AALBORG UNIVERSITY

Department of Biotechnology, Chemistry and Environmental Engineering, Aalborg University,
9000 Aalborg, Denmark

Separation of secondary dispersed diesel-water emulsions by electrospun membranes identified by inverse-quantitative structure-activity relationship

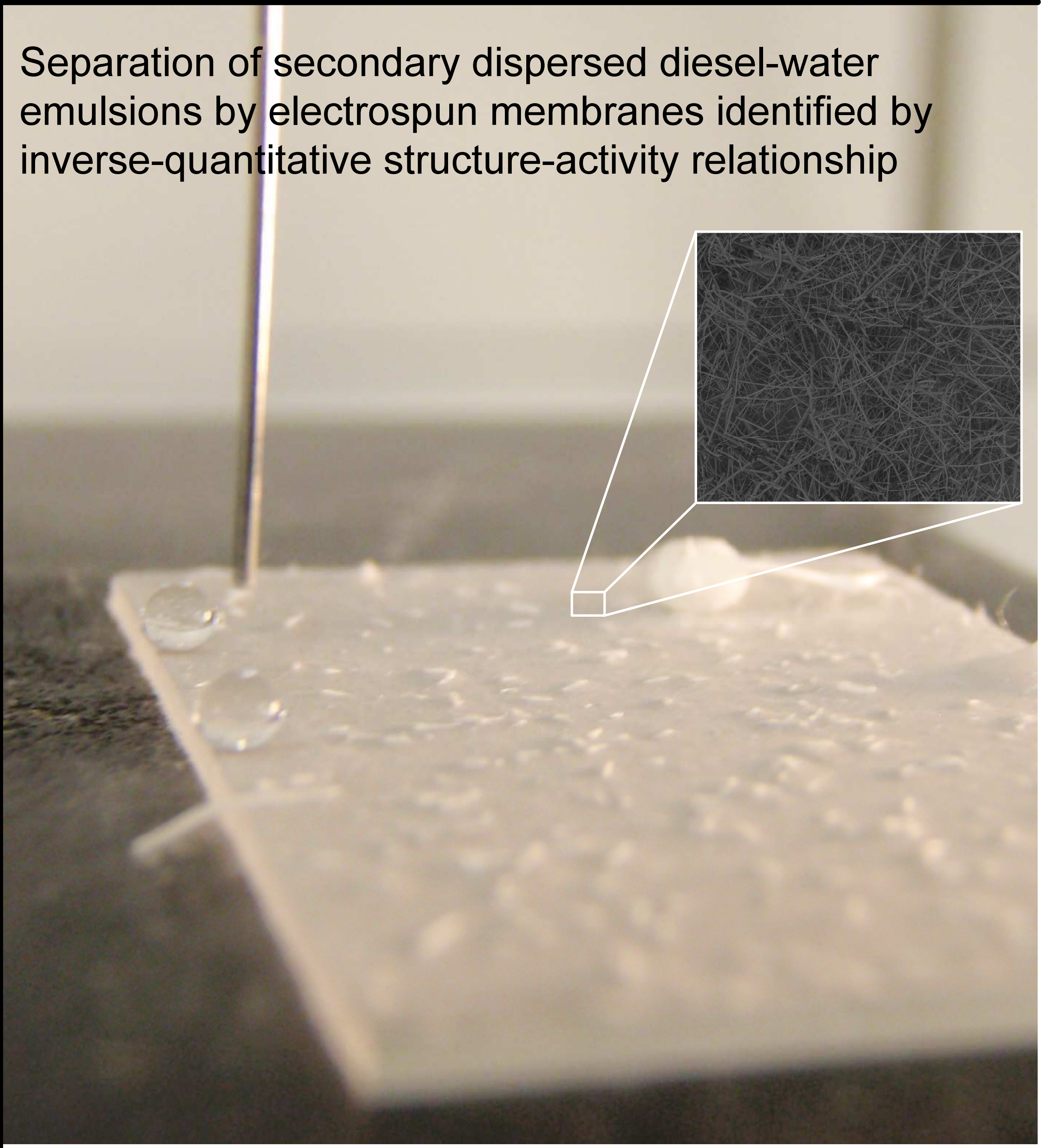

Kristian Bastholm Knudsen
Master Thesis
May 2012

Title: Separation of secondary dispersed diesel-water emulsions by electrospun membranes identified by inverse-quantitative structure-activity relationship

Danish Title (Dansk titel): Separation af sekundære diesel-vand emulsioner med electrospundet membraner identificeret ved brug af inverse-quantitative structure-activity relationship

Project: Master Thesis

Project Period: September 1st 2011 - May 31th 2012

Author:

Kristian Bastholm Knudsen

Supervisors:
Associate Professor Kristian Keiding[1]
Professor George G. Chase[2]
Professor Donald P. Visco Jr.[2]

Issues: 5
Number of Pages: 75
- Report: 74
- Appendix: 1
Additional Material: CD-ROM

---

[1] *Department of Biotechnology, Chemistry and Environmental Engineering, Aalborg University, 9000 Aalborg, Denmark*

[2] *Department of Chemical and Biomolecular Engineering, The University of Akron, OH 44325-3906, United States*

Preface

This report covers the 9th and 10th semester in chemical engineering at the School of Engineering and Science at Aalborg University. The project was conducted from September 1st 2011 to May 31st 2012.
Most of the work was carried out at The University of Akron (Ohio, USA) in the period from November 20th 2011 to April 4th 2012. In this connection, I wish to thank Professor George Chase for accepting me into his group and for his guidance and useful discussions. I would also like to thank research assistant Goutham Viswanadam and Sarfaraz Patel for guidance and technical assistance during the experimental work and research assistant Jon Rajala for dragging me to Starbucks® when needed. I also wish to thank Professor Donald P. Visco and research assistant Hamed Kayello for their help and supervision in developing the inverse-quantitative structure-activity relationship.
Likewise, I wish to thank my supervisor Associate Professor Kristian Keiding at Aalborg University for help and guidance when needed.

Last but not least, I would like to thank my sponsors for their support to realize my thesis.

- Oticon Fonden
- Knud Højgaards Fond
- Ingeniørforeningens Låne- og Hjælpefond
- Augustinus Fonden
- Reinholdt W. Jorck og Hustrus Fond
- Roblon Fonden

Aalborg, May 2012
Kristian Bastholm Knudsen

Abstract

This present project has focused on the fabrication of novel membranes for the separation of secondary dispersions of water-in-diesel. The quest of improving the efficiency and reduce the pressure drop of such filtrations has, due to the introduction of biodiesel, increased caused by the content of surfactants in biodiesel. The surfactants decrease the drop size distribution and increase the concentration of total water, which decreases the combustion efficiency and lifetime of engines.

The separation of secondary dispersions of water-in-diesel has previously been demonstrated to be dependent on the hydrophobicity of the membrane surface. The hydrophobicity of a surface is both dependent on the surface energy and surface morphology. In the search of a novel membrane material an inverse-quantitative structure-activity relationship was developed on the basis of polymers' critical surface tensions.

The model predicted new potential polymers with low critical surface tensions, i.e. hydrophobic materials. The solutions were then subjective evaluated, which resulted in the purchase of poly(styrene-co-α-methylstyrene), PSMS.

The surface of PSMS was experimentally characterized by measuring the water contact angle, which resulted a contact angle of 94.10$\pm$3.73^o, thus PSMS could be characterized as being hydrophobic.

To further increase the hydrophobicity, PSMS was electrospun. This is a process that utilize electrostatic forces to form polymeric fibers with induced pores and hollows, thus increasing the hydrophobicity of the surface. The electrospinning of PSMS resulted in surfaces with a water contact angle of 165.85$\pm$0.51^o hereby producing superhydrophobic surfaces.

Membranes were, on the basis of the previous results, fabricated by electrospinning PSMS on a support material. Membranes, that were electrospun using a 60 w/w % PSMS/DMF solution and a deposited mass of 30 g PSMS/m^2, achieved the highest separations efficiencies of 93.85$\pm$2.65 % with a pressure drop of 0.64$\pm$0.17 kPa.

Resumé af projektet (Danish abstract)

Dette projekt har fokuseret på fremstillingen af nye membraner til separationen af sekundære dispersioner af vand-i-diesel. Interessen for at øge effektivitet og mindske tryktabet er i takt med anvendelsen af biodiesel steget, hvilket skyldes, at biodiesel indeholder en række surfaktanter, som mindsker vand dråbe distributionen i diesel samt øger indholdet af bundet vand. Dette mindsker brændstof økonomien samt levetiden på motorer og ønskes derfor fjernet.

Separationen af sekundære dispersioner af vand-i-diesel har tidligere vist, at være afhængig af membranen overfaldens hydrophobicitet. Hydrofobiciteten er en funktion af både overflade energi samt struktur og i søgen efter nye membran materialer blev en inverse-quantitative structure-activity relationship model, baseret på den kritiske overflade energi af polymere, udviklet.
Modellen forudsagde nye potentielle polymer strukturer med lav kritisk overflade energi, dvs. hydrofobe polymere. Løsningerne blev subjektivt evalueret og resulterede i købet af poly(styrene-co-α-methylstyrene), PSMS.
Overfladen af PSMS blev eksperimentelt undersøgt og resulterede i en vand kontakt vinkel på 94.10 ± 3.73^o, som derved kunne karakterers, som værende hydrofobt.
For at øge hydrofobiciteten ydereligere blev PSMS electrospundet, hvilket er en proces, som vha. elektrostatiske kræfter danner fibre. Dannelsen af fibre inducere ujævnheder og huller i overflade strukturen og kan derved øge hydrofobiciteten. Dette var tydeligt, da electrospindingen af PSMS producerede overflader med vand kontakt vinkler på 165.85 ± 0.51^o, hvilket kan karakteriseres som værende en superhydrofob overflade.
Membraner blev på baggrund af ovenstående forsøg fremstillet ved at electrospinde PSMS på et support materiale. Membraner, som blev electrospundet udfra 60 w/w % PSMS/DMF og med en aflejringsmasse på 30 g PSMS/m^2, opnåede den maksimale fjernelsesprocent på 93.85 ± 2.65 % med et tryktab over membranen på 0.64 ± 0.17 kPa

Abbreviations

θ	Contact angle [degree]
θ_{norm}	Normalized contact angle [-]
CST	Critical surface tension [mJ/m^2]
CST_{norm}	Normalized critical surface tension [-]
γ_{SV}	Solid/vapor interfacial tension [mJ/m^2]
γ_{SL}	Solid/liquid interfacial tension[mJ/m^2]
γ_{LV}	Liquid/vapor interfacial tension[mJ/m^2]
CAMD	Computer-aided molecular design
QSAR	Quantitative structure-activity relationship
I-QSAR	Inverse-quantitative structure-activity relationship
$^h\sigma_G(x)$	The atomic Signature rooted on atom x in molecule G
$^h\sigma(G)$	The molecular graph of molecule G
MLR	Multiple linear regression
LOOCV	Leave-one-out cross-validation
PSMS	Poly(styrene-co-α-methylstyrene)
R_D	The apparent Darcy flow resistance [m^{-1}]

Contents

Appendix

1. Introduction

The quest to obtain improved water repelling surfaces is of interest to both the academic world and the industrial fields. It involves controlling both the chemical composition and the surface morphology [1] [2]. One of these fields is in the separation of diesel-water emulsions, which might seem like a problem solved but in 2007 the United States Environment Protection Agency enforced new standards for the emission gases from diesel engines by reducing the content of sulfur with 97 % to a concentration of 15 ppm. In order to meet such demands the diesel manufactures started implanting the refining step hydrodesulphurization hereby producing the product ultra low sulphur diesel, ULSD. Hydrodesulphurization is a catalytic process that removes sulfur, some non-wax type species and natural lubricants from the diesel. The loss of diesels natural lubricants both caused unstable pressures in the combustion champers and tears in the injection systems and the addition of other lubricants were therefore clearly needed to ensure a proper combustion and lifespan of diesel engines. At the same time oil prices escalated and political and social pressure forced biodiesel into the market by mixing it with ULSD in order to lower prices and minimize the use of fossil fuels. The mixture improved the lubricity of ULSD but introduced yet another problem - surfactants [3].

When water is introduced to the surfactant-containing fuel, the surfactants depress the interfacial tension resulting in stable drop size distributions with diameters $< 100\ \mu$m, known as secondary dispersions. The secondary dispersions of water allows the water drops to pass through the excisting fuel filters, traditionally composed of silicone treated with cellulose, and into the injection system. The injection systems in most modern diesel engines is high pressure injection systems implemented to increase fuel efficiency and minimize emissions gasses such as NO_x and it is this system that is vunerable to contaminants such as water. Injection manufactures have therefore set treshold values for emulsified water in diesel to 200 ppm and the concentration of free water to zero. To ensure this, a filter should be incorporated in the fuel system that economically, safely and efficiently removes the secondary dispersions of water-in-diesel [3].
Coalescence filtrations have displayed such properties and generally two different kinds of approaches are used in the separation of droplets from a liquid. Both methods depend on the kinetic energy being greater than the surface tension of the droplets hereby coalescing the droplets. The first type of coalescence filtration utilize a hydrophilic depth coalescing filter and as the fuel is pumped through the filter, water associates itself with the filter hereby slowing it down and as more water enters the filter water coalesce and the drops increase in size. When the larger water drops exits the filter downstream, they are separated on the basis of density [4] [5]. The second type of coalescence filtration is by the use of superhydrophobic filters, here water is repelled by the membrane surface and as more water is repelled it coalesce and is seperated on the basis of density on the upstream side of the membrane. The separation efficiencies of both filtrations are dependent on the flow rate, bed depth, drop size, hydrophobicity, fiber size, fiber area and fiber orientation [1] [6] [7]. The two different kinds of coalescence filtrations are illustrated in Figure 1.1.

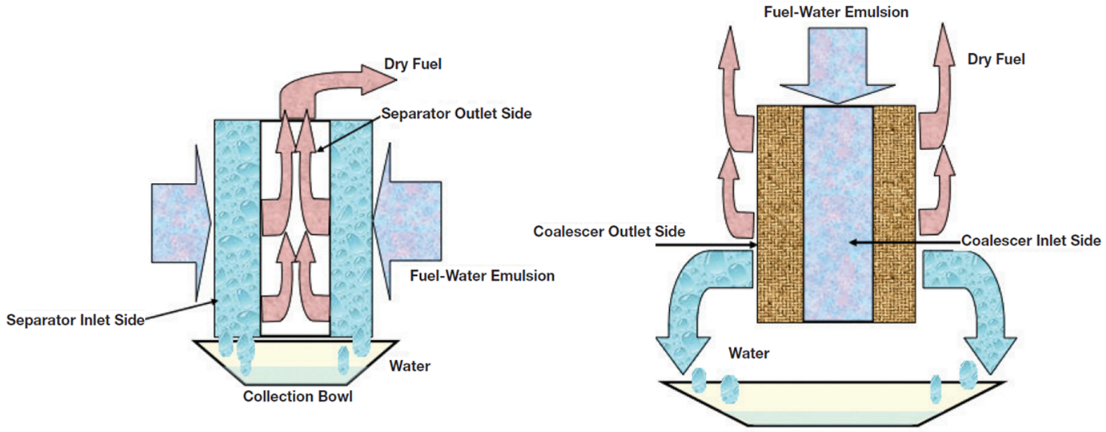

Figure 1.1: The first pictures illustrates the coalescence filtration of a water-in-fuel by the use of a hydrophilic filter, while the second picture illustrates the coalescence of water by the use of a superhydrophobic filter [3].

To improve the separation of secondary dispersions of water in ULSD, this project focuses on three topics. The first topic is the search of new super hydrophobic polymers, using inverse-quantitative structure-activity relationship, for the use in coalescence membranes. Second is the production of fiber mats by electrospinning and third is the investigation of the coalescence performance of the produced membranes.
The following chapters presents the wettability, a method used to characterize the hydrophobicity, inverse-quantitative structure-activity relationship, a computer aided technique to identify novel compounds, and electrospinning, a method used to develop fibers with high surface areas.

2. Theory

2.1 Wettability and surface energies

Surface chemistry is a major part of science in the aspects of a chemical process, engineering and technology, biology and medicine. The free energy of a surface plays a major role in controlling the behaviour of any system and thus needs careful consideration when designing a system [8]. The free energy of a surface is a function of the cohesive forces of the solid; the strongest materials being formed of purely covalent bonding while weaker solids contain weaker bonds, such as hydrogen bonds. The wettability of a surface on the other hand is mainly governed by adhesive Van der Waals forces between water and a surface. In general the wettability is poor when the cohesive forces within a liquid is greater than the adhesive forces between the liquid and solid, which is illustrated in Figure 2.1.

The wettability of a surface can be characterized in terms of the contact angle between a liquid droplet and the connecting surface. The droplet will either remain as a drop or spread out onto the surface forming a thin liquid film. A surface can hereby be characterized by measuring the contact angle of either water or oil droplets on a surface, resulting in the following definitions. Hydrophilic or oleophilic when the contact angle is below 90^o, hydrophobic or oleophobic when above 90^o, superhydrophobic or superoleophobic when greater than 150^o [9].

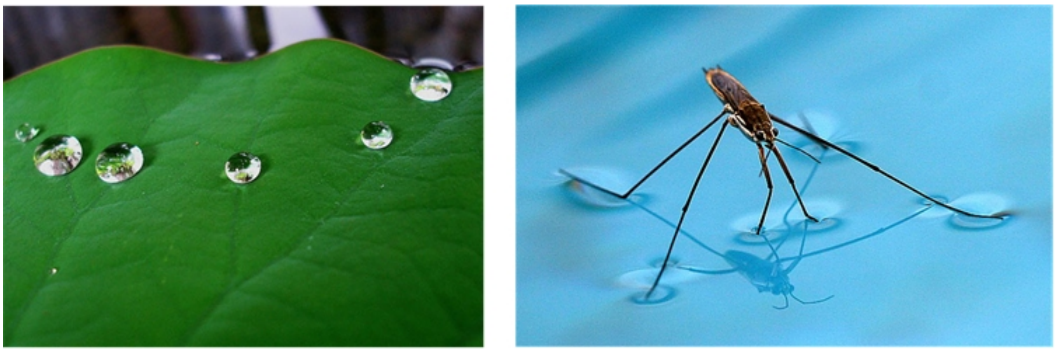

Figure 2.1: Illustrates the superhydrophobic properties of a lotus flower and the legs of a water strider [10] [11].

In the construction of superhydrophobic or superoleophobic surfaces the structure of the surface also plays an important role, which is best explain by simplifying the structures of a surface as either beeing smooth or rough. The hydrophobicity of the smooth surface will primarly be governed by the surface free energy while the hydrophobicity of the rough surface will increase since this induces trapped air beneath the droplet [9]. The control of both the surface energy and surface structure are of great importance since this can lead to remarkable properties, as decribed by the three types of surfaces below.

For a surface with a free surface energy above that of water and oil, as depicted in Figure 2.2, hydrophilicity and oleophilicity can coexist. This is thermodynamically favorable since the surface will lower its free energy by being covered with a lower energy liquid and by inducing pores and hollows to the surface the hydrophilicity and oleophilicity can be increased even further. This is due to the increase in surface area, which will result in the liquids entering the pores and hollows thus lowering the contact angle [9].

A surface with a free surface energy below that of oil and water, as depicted in Figure 2.2, will be hydrophobic and oleophobic since the liquids have higher surface tensions than the energy of the surface. The liquids will therefore not lower the free surface energy by wetting the surface and the liquids are therefore be repelled by the surface causing an increase in the contact angle. In order to increase hydrophobicity and oleophobicity of such a surface, roughness can be induced, which produces pores and hollows into the surface. The liquids will however not penetrate the pores and hollows since the adhesion already is weak and air is instead captured below the liquid droplets. The adhesion between the captured air pockets and the liquid droplets is basically non-existent hereby further increasing the contact angles [9].

A surface with a free surface energy in between the surface tensions of water and oil, as depicted in Figure 2.2, will be oleophilic and hydrophobic since water will increase the free surface energy and oil will lower it. Roughness can again be applied to the surface but due to the energy of the surface, oil will penetrate the pores and hollows hereby increasing the oleophilicity of the surface. Water on the other hand will be repelled from the surface due to the captured air hereby increasing the hydrophobicity [9].

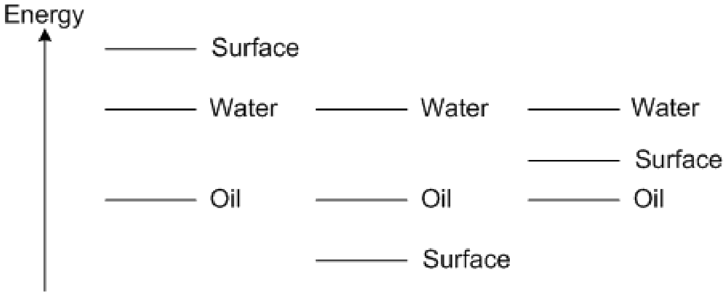

Figure 2.2: The three types of surface energies.

2.1.1 Young's equation

Thomas Young described how the coehsive and adhesive interactions between a solid and a liquid occurs by measuring the contact angle. This lead to what now is known as Young's equation, equation 2.1, which is a force balance equation described by interfacial tensions.

$$cos(\theta) = \frac{\gamma_{sv} - \gamma_{sl}}{\gamma_{lv}} \tag{2.1}$$

Here θ is the contact angle in Youngs model, as depicted on Figure 2.3, γ_{sv}, γ_{sl} and γ_{lv} are the solid/vapor-, solid/liquid- and liquid/vapor interfacial tension [mJ/m^2], respectively.

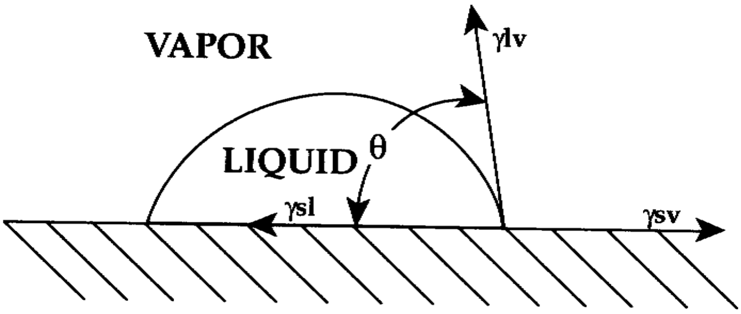

Figure 2.3: Illustrates the different interfacial tensions and the contact angle, θ [12].

2.1.2 Critical surface tension

The critical surface tension, CST, is another method used to determine the surface energy or solid/vapor interfacial tension by using equation 2.2 and 2.3.

$$\gamma_{sl} = \gamma_{sv} - \gamma_{lv} \cdot cos(\theta) \tag{2.2}$$

$$\gamma_{sl} = f(\gamma_{sv}, \gamma_{lv}) \tag{2.3}$$

Originally developed by Zisman, the method suggests that when a liquid just wets a surface then γ_{sv} is equal to γ_{lv}. Experimentally this is done by measuring the contact angles between a solid and a range of liquids. Hereby one obtains cos(θ) values as a function of different γ_{lv} values, which should be a smooth linear relationship. When examining low energy surfaces, the surface tension of the liquids are often too great hereby making the relationship insufficient. Zisman solved this by extrapolating the relationship to cos(θ) = 1 and hereby obtaining the surface tension of the solid. The surface tension obtained at cos(θ) = 1 is however not equal to γ_{sv} due to some factor inflicting with the measurements of the contact angle, such as absorption of the solvent to the surface and solvent evaporation. The surface tension at cos(θ) is therefore referred to as the critical surface tension, γ_c, hereby making γ_c = γ_{lv} at θ = 0^o [13]. The choice of solvents is of great importance in the measurements of the CST since these will determine which type of forces exist at the interface of the solid and liquid, thus if an appropriate range of liquids is not chosen, a false CST can be obtained [14].

2.2 Inverse-quantitative structure-activity relationship

Potential new polymers can be identified using computer-aided molecular design, CAMD. The purpose of CAMD is to obtain molecular structures that possess an improved property. Quantitative structure-activity relationship, QSAR, is a empirical type of CAMD that relates the numerical value of an activity or property to structural components of a given compound [15] [16]. QSAR can be used to predict the property of compounds by translating molecular structures into molecular descriptors [15], which is a mathematical procedure that transforms chemical information into a useful number [17]. In the construction of a QSAR equation molecular descriptors acts as independent variables while the property of interest act as the dependent variable [16]. The predictability of a QSAR model depends on the size and diversity of the molecules used in the model. This set of data is normally referred to as the training set, thus the larger and more diverse training set the better predictive capacity [16]. QSAR models are however restricted only to determine the property of the compounds closely related to a training set and a model was therefore derived from QSAR which purpose is to design new compounds with improved properties, on the basis of a QSAR analysis. This method is known as the inverse-quantitative structure-activity relationship, i-QSAR, and is more complex than QSAR for a number of reasons, which will be outlined in the following [18]. In short the i-QSAR reassembles the molecular descriptors to construct compounds, which properties have been determined from the QSAR analysis [16].

I-QSAR can be divided into six steps, as shown on Figure 2.4. The first step is the translation of the 2D molecular structures into molecular descriptors. The second part is the QSAR analysis and the third part is the generation of constraint equations, which restricts the chemical space. The fourth step consists of solving these equations, which yields in the generation of new molecular Signatures. The fifth step is the translation from molecular descriptors to actual 2D molecular structures. The last step is a subjective evaluation of the solved structure [16].

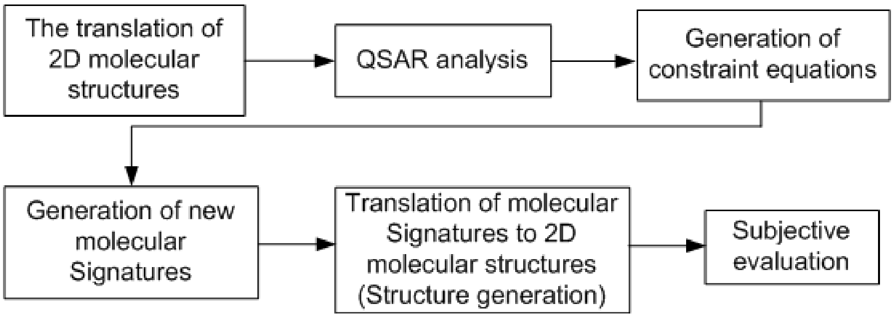

Figure 2.4: Illustrates the six steps of an i-QSAR analysis.

In the following the i-QSAR analysis is described step by step, starting with the choice of molecular descriptor. The translation is best described by using an example and is therefore first presented in section 2.2.6.

2.2.1 Molecular descriptor

A molecular descriptor is a procedure that computes structures into a vector space in which the molecular structure can be encoded into a useful number. For a molecular descriptor to be useful in regards to i-QSAR, the value of the descriptor should give an insight into the property of the molecules and be able to be a part of a model that can predict properties of new molecules. Molecular descriptors are often a result algebra, graph theory, information theory, computational chemistry etc. [17] [18]. The molecular descriptor used in this project was the molecular descriptor called Signature due to its success to address the i-QSAR problem. The success of Signature is threefold. First, Signature performs the QSAR analysis as well as conventional molecular descriptors [16] [19]. Second, Signature has a lower degeneracy than other molecular descriptors and can be controlled by the user by a variable termed height. The degeneracy of a molecular descriptor is how well it is able to map one property to one descriptor. Ideally a molecular descriptor should only describe one structural area of a compound instead of several. In the construction of the i-QSAR model it is crucial that the molecular descriptor has a low degeneracy since this will limit the number of solutions and hereby the computational time [16]. Third, Signature provides a way to go directly from a numerical solution to a 2D molecular structure, due to already exciting algorithms from graph theory, which connects the Signatures [16] [19].

Signature

Signature is a systematic codification system over an alphabet of atom types which describes the extended valence, i.e. neighborhood, of atoms in a molecule [20]. The Signature is a transformation of the 2D molecular structure of a molecule into a set of canonized substructures. Signature was developed by Faulon et al. (2003) [20] and they developed two kind of Signatures: the atomic and molecular Signature. The former representing a single canonized substructure of the molecule and the latter being a set of canonized substructures hereby representing the 2D molecular structure of a molecule in terms of the codification system [19].

Prior to introducing the atomic and molecular Signature some terminology and notation has to be defined. The Signatures are based on graph theory and a molecule can therefore be defined as a molecular graph, as illustrated in equation 2.4.

$$G = (V, E, C, c_G) \tag{2.4}$$

Where G is the molecular graph, V are the vertices, atoms, represented in the molecule G. E are the corresponding edges, bonds, between the atoms and atoms in the graph are colored, C, by the elements of the period table and labeled with a number in order to prevent duplication. c_G associates the valance of each atom type hereby limiting the number of covalent bonds formed by an atom [20]. A molecular graph is a method used to describe the structure of a molecule which is not necessarily saturated, as described by equation 2.5.

$$\forall x \in V_G, deg(x) \leq valence(C_G(x)) \tag{2.5}$$

Thus for all atoms, x, in the molecular graph G the vertex degree, number of bonds, to the atom must be equal or less than the valence of those atoms [20].

The atomic signature

Atomic Signatures are, as previously described, canonized substructures of a molecule which describes a limited neighborhood of the molecule. In terms of graph theory the atomic Signature is defined as a subgraph of the molecular graph G. The atomic Signature can be defined as ${}^h\sigma_G(x)$ where x is an atom of G, h is the height of the atomic Signature which is defined as the distance from atom x to the height h, thus limiting the number of atoms and bonds in the subgraph [15].

The canonical representation takes the form of a tree that is rooted on an atom and covers atoms and bonds in the form of vertices and edges respectively up the height h. The atomic Signature is therefore a directed graph, which is constructed in three steps, detailed in the following and illustrated in Figure 2.5.

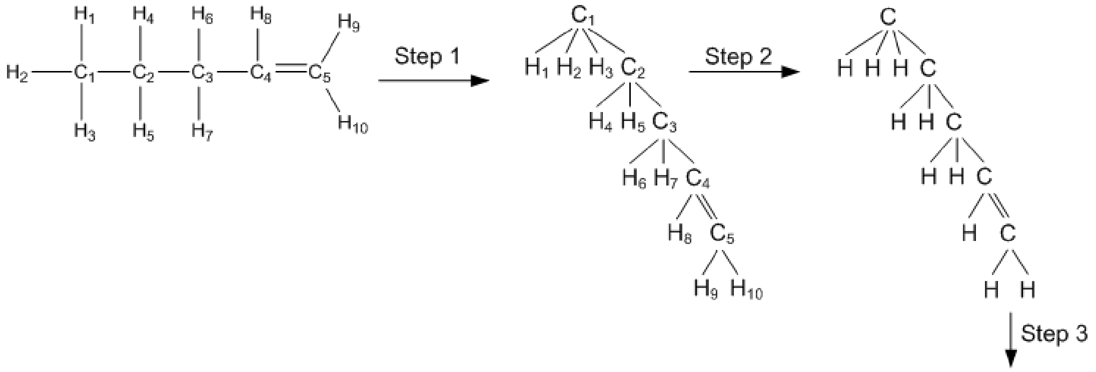

${}^0\sigma(G)$ = 10 [H]( ) + 5 [C]( )

${}^1\sigma(G)$ = 10 [H]([C]) + 1 [C]([C][H][H][H]) + 2 [C]([C][C][H][H]) + 1 [C]([C]=[C][H]) + 1 [C](=[C][H][H])

${}^2\sigma(G)$ = 3 [H]([C]([C][H][H])) + 4 [H]([C]([C][C][H])) + 1 [H]([C]([C]=[C])) + 2 [H]([C](=[C][H])) +
1 [C]([C]([H][H][H])[C]([C][H][H])[H][H]) + 1 [C]([C]([C][H][H])[H][H][H]) +
1 [C]([C](=[C][H])[C]([C][H][H])[H][H]) + 1 [C](=[C]([H][H])[C]([C][H][H])[H]) + 1 [C](=[C]([C][H])[H][H]

Figure 2.5: Illustrates the procedure in the translation of the 2D molecular structure of pentene into atomic and molecular Signatures. ${}^0\sigma(G)$, ${}^1\sigma(G)$ and ${}^2\sigma(G)$ are the height 0, 1 and 2 molecular Signature, respectively. Note that each term in the three molecular Signatures corresponds to atomic Signatures of equal height. The number before each atomic Signature is the occurrence number of the respective atomic Signature.

In the first step a subgraph ${}^hG(x)$ is extracted from G which contains all atoms and bonds from the root atom x to the distance h. The atoms are then labeled in a canonical order, atom x having label 1, atom 2 labeled 2 etc. A tree spanning all bonds of ${}^hG(x)$ is constructed where the root of the tree is atom 1. The first layer of the tree consists of neighbors to atom 1, the second layer consists of neighbors to atoms of the first layer; this construction continues up to layer h. The construction is then terminated when reaching layer h or if an atom in layer k, k < h, already is present in another layer which is true for cyclic compounds. Two, the canonical labeled atoms that only appears once are removed and the remainder is renumbered as in the order they appear [20]. Three, the atomic Signatures are written by reading the tree in a depth first order and printing "[ ]" and "( )" around each atom and layer, respectively [15] [20]. In addition bonds are labeled depending on the bond type: single bonds being unlabeled, double bonds are labeled with "=", triple bonds with "t" and aromatic bonds with "p" [15].

The molecular Signature

In other words an atomic signature is a string of characters describing the atomic orbitals from atom x to the height h. In order to construct the structure of a molecule in terms of the canonized substructures, the molecular Signature, ${}^{h}\sigma$(G), is a summation of the atomic Signatures [15], as expressed by equation 2.6.

$$ {}^{h}\sigma(G) = \sum_{x \in V_G}^{h} \sigma_G(x) \tag{2.6} $$

2.2.2 Quantitative structure-activity relationship analysis

The second step in the i-QSAR analysis is the QSAR analysis. In this step the unique atomic Signatures acts as independent variables while the property of interest function as the dependent variable. A list of unique Signatures is compiled from the compounds in the training set and a descriptor matrix is created where the rows are the compounds, columns are the unique atomic Signatures and the entries is the occurrence numbers of each atomic Signature [15] [16] [19]. In order to ensure the development of a good correlated and predictive QSAR model procedures are applied to sort and remove atomic Signatures. To ensure a good correlated model perfectly correlated rows, atomic Signatures with same predictive values are removed hereby avoiding redundancies which can interfere with the QSAR equation [15]. In order for the QSAR equation to predict the property of interest for compounds beyond the scope of the training set, the cross-validating method named leave-one-out cross-validation, LOOCV, is often performed. This method is described further in the following but as consequence of applying this method the occurrence number of a atomic Signature must be equal to or greater than 3, thus atomic Signatures with occurrence numbers below this value are removed [15] [16] [19].

Next, the descriptor matrix and the corresponding property values are used to determine the QSAR equation and depending on the correlation between the two, different regression methods are used [15] [16] [19]. An efficient method for a linear correlation is the forward stepping multiple linear regression. The main advantage is that it is less computationally intensive and can therefore be used on datasets with a large number of atomic Signatures [21]. If multiple linear regression, MLR, is applied, the QSAR equation takes the form of equation 2.7.

$$ P = \beta_0 + \beta_1 \cdot x_1 + \ldots + \beta_i \cdot x_i \tag{2.7} $$

Where β_0 is the regression coefficient for all the included atomic Signatures, β_i represents the regression coefficients for the atomic Signature i, x_i represents the occurrence number of the atomic Signature i and P is the property of interest. The MLR procedure determines which atomic Signatures are the most significant based on F-statistics [15] [16] [19] thus the atomic Signature with smallest F value is selected first, provided that it is below the critical F value and following atomic Signatures are then added depending on their F value [21]. The Coefficient of determination, R^2, which measures the correlation between the models predicted property and the experimental property will increase as atomic Signatures are added but a high R^2 value will however not ensure the predictability of the model outside of the original training set due to a phenomena called overfitting [15]. It is therefore crucial to validate if the fitted data can predict the properties on a new set of compounds and to ensure this predictability, LOOCV is often used [22]. LOOCV is calculated by removing each compound in the training set, one at a time and refitting the regression coefficients. Each model obtains a new R^2 value, commonly referred to as q^2, and while R^2 increases as the number of independent variables are added, q^2 normally reaches a maximum and then decreases due to noisy data. A model with a q^2 greater than 0.5 is usually considered being predictable thus to ensure that a model is predictable the number of atomic Signatures included in the QSAR equation is decided on the basis of the q^2, providing q^2 is greater than 0.5 [15] [22].

2.2.3 The constraint equations

The next step in the i-QSAR analysis is the construction of constraint equations, which serve as constraints in the construction of new compounds by reconnecting atomic Signatures into molecular Signatures with desired properties determined by the QSAR equation [18]. The constraint equations restrict the occurrence numbers of the atomic Signatures in a molecular Signature. The solutions must however represent quantities meaningful to the Signature hence the occurrence numbers should take the form of non-negative integer values [15] [18]. As an example the constraint equations would reject the molecular Signature: 1 [C]([H][H][H][H]), since the molecular Signature containing the mentioned atomic Signature must also contain at least 4 occurrences of the atomic Signature: [H]([C]). Since the molecular Signature does not contain the additional atomic Signature, the molecular Signature cannot correspond to a real 2D molecular structure. To enforce the occurrence numbers, three constraint equations are normally used in the analysis of polymers: The graphicality equation, the consistency equation and the polymer-repeating unit, PRU, equation [18].

The graphicality equation is a valence constraint equation that ensures that the valence of each atom in the reconstruction is meet - hereby only constructing molecules with a net charge of zero. It is based on graph connectivity due to the nature of the atomic Signature, i.e. being a canonized subgraph of a molecular graph [16]. In order to construct a connected graph, that is a molecular Signature in which all atomic Signatures are bonded to each other, two demands are necessary. First, the sum of all bonds must be even. This is true since each bond must be present in two atomic Signatures, as for the case of the molecular Signature of methane: 1 [C]([H][H][H][H]) and 4 [H]([C]), each of the C-H bonds occur twice, once in [C]([H][H][H][H]) and once in [H]([C]) and in terms of graph theory this is known as the handshaking lemma. The second demand is that the total number of atomic Signatures with an odd number of bonds also must be

even, as for the value of the atomic Signature [H]([C]) in methane.
If one of the two requirements are not satisfied an unconnected graph is constructed that is a molecule in which a bond only is present in one atomic Signature meaning an atom is missing in the molecular Signature. To efficiency calculate if a molecular Signature is connected an equation taken from graph theory is applied. Equation 2.8 illustrates the graphicality equation.

$$[(i-2)\cdot x_i]+2 \equiv 0 mod 2 \tag{2.8}$$

Where i is the vertex degree, valence, of the parent atom in the atomic Signature i and x_i is the occurrence number of the atomic Signature i. The "-2" and "+2" terms ensures, as described in the above, that the sum of all bonds must be even and that the total number of atomic Signatures with odd bonds is even, respectively. Note that "$\equiv$ 0 mod 2" indicate that the equation is a modulus equation, thus for a molecular Signature to be connected the total number of bonds must be even [15].

While the graphicality equation ensures the valence of each atom is met, it does not ensure that atoms are bonded to the right atoms. The consistency equation ensures this alignment of atoms between two atomic Signatures. The consistency equations arises from the way the molecular Signature is created; a bond in one atomic Signature will have a corresponding bond in another atomic Signature, but in the reverse order. In the construction of new molecular Signatures it is therefore guaranteed that a bond in one atomic Signature will match with a bond in another atomic Signature. Blind reconstruction is however not the way to go and the consistency equations enforces this correlation by subtracting the bonds between the parent and child atomic Signatures, which must be equal to zero if atoms align [15], as showed in equation 2.9.

$$\#(^{h-1}\sigma_x \rightarrow^{h-1} \sigma_y) - \#(^{h-1}\sigma_y \rightarrow^{h-1} \sigma_x) = 0 \tag{2.9}$$

Where "$\#(^{h-1}\sigma_x \rightarrow^{h-1} \sigma_y)$" is the occurrence number of the parent atomic Signature and "$\#(^{h-1}$-$\sigma_y \rightarrow^{h-1} \sigma_x)$" is the occurrence number of child atomic Signatures. The term "$^{h-1}$" indicate that only root atoms are used in the equation [15].

A consistency equation is constructed for each bond type included in the training set and each equation only contains atomic Signatures, which include that specific bond type. Equation 2.9 is however not adequate for bond types as the carbon-carbon bond since one cannot distinguish between the parent or child atomic Signature. Instead a modulus equation is utilized so that the sum of such bonds in the two atomic Signatures must be even [15] [18]. This form of consistency equation is illustrated in equation 2.10.

$$\#(^{h-1}\sigma_i \rightarrow^{h-1} \sigma_i) \equiv 0 mod 2 \tag{2.10}$$

The final constraint equation is the PRU equation, which is specific for the case of linear homo polymers and it ensures that the occurrence number of atomic Signatures containing root atoms that are repeating atoms is equal to 2, which must be the case for a linear homopolymer [18].

2.2.4 Generation of new molecular Signatures

A solution to the i-QSAR analysis must satisfy all of the consistency equations, the graphicality equation and the PRU equation. Solving all of these equations result in new molecular Signatures but is a challenging task since there are more unknown variables than there are equations. This creates an infinite number of solutions and additionally time and storage space is also an issue. Multiple algorithms have been developed to solve similar problems, but as Weis and Visco (2010) [15] discussed most algorithms have issues with both computational time and storage space. Weis and Visco (2010) [15] therefore developed a brute-force method which is an iterative approach to solve the constraint equations based on the min/max occurrence values of the atomic Signatures in the training set. The technique is however not truly brute-force since not all min/max occurrence values are used and in practice a truly brute-force method is unreasonable not only because it is too costly to compute, but also due to the reason that the domain under which the QSAR analysis can be expected to be accurate is limited [18]. To ensure that extrapolations are not performed when solving the constraint equations two forms of limitations are added. First, only atomic Signatures, which are present in the training set, is used, hereby validating the QSAR equation. This is done by only adding atomic Signatures from the training set to the constraint equations. Second, the molecular size of potential solutions is limited by the maximum occurrence values of the specific atomic Signature [18].

The brute-force method developed by Weis and Visco (2010) [15] solves the constraint in a step-wise manner so that equations, which contain variables with the lowest occurrence values, are solved first. This means that atomic Signatures that have been solved in the first constraint equation then have a fixed value(s) and when this atomic Signature then appear in another equation only the value(s) that satisfied the first equation is used. This continues until all constraint equation have been solved resulting in a range of new molecular Signatures [15].

2.2.5 Structure generation

At this point molecular Signatures with desired properties, which have satisfied the constraint equations, have been generated. These solutions are however still vectors and in order to transform a molecular Signature into a 2D molecular structure one must recognize that a molecular Signature can result in multiple 2D structures. As an example all compounds with the chemical structure of $C_{10}H_{22}$ would obtain a height 1 molecular Signature of 22 [H]([C]), 8 [C]([C][C][H][H]) and 2 [C]([C][H][H][H]). It is obvious that changing the sequence of atomic Signatures will result in different 2D molecular structures and in fact there exists 75 isomers of decane.

An algorithm developed by Faulon et al. (2003) [20] was utilized to transform molecular Signatures into 2D molecular structures which is best described by using an example, as presented in the following.

2.2.6 Example of an inverse-quantitative structure-activity relationship

This section serves as an illustration of how the i-QSAR method is performed by applying it to a training set consisting of two compounds poly(propylene), PP, and poly(vinylchloride), PVC. As described in the above, the first step is the translation of the 2D molecular structures into molecular Signatures, here height 1 atomic Signatures are used, and both translations are depicted in Figure 2.6.

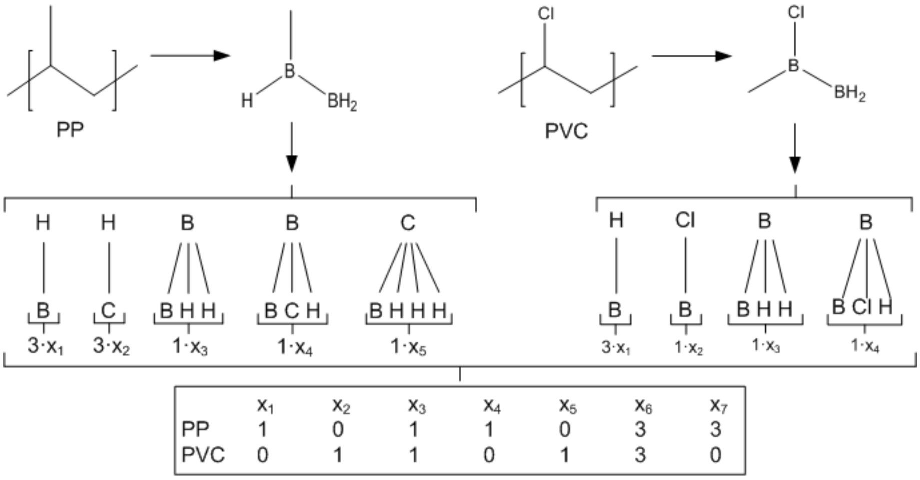

	x_1	x_2	x_3	x_4	x_5	x_6	x_7
PP	1	0	1	1	0	3	3
PVC	0	1	1	0	1	3	0

Figure 2.6: The translation of PP and PVC into height 1 atomic Signatures.

Note that in the first step of the translation, the repeating atoms are replaced with boron. This is done to ensure the identification of the repeating atoms in the reconstruction, since one otherwise cannot tell the difference between repeating atoms and non-repeating atoms. These dummy atoms may not be present in any compound in the training set and in order to validate the octet rule and the consistency equations, they must have a valence less than the original atoms [18]. In this example only the i-QSAR part is described since only two of the atomic Signatures had occurrence numbers equal to or greater than 3 making it impossible to perform LOOCV. The rest of this section therefore deals with the generation of the constraint equations, solving these and transforming the two generated solutions into 2D molecular structures by using the structure generator developed by Faulon et al. (2003) [20].

In the following the constraint equations are constructed by using the *unique* height 1 atomic Signatures from PP and PVC, which are summarized in Table 2.1.

Table 2.1: Illustrates the unique atomic Signatures of PP and PVC.

Variable	Height 1 atomic Signature
x_1	[B]([B][C][H])
x_2	[B]([B][Cl][H])
x_3	[B]([B][H][H])
x_4	[C]([B][H][H][H])
x_5	[Cl]([B])
x_6	[H]([B])
x_7	[H]([C])

On the basis of equation 2.8, the graphicality equation can determined, which results in equation 2.11.

$$x_1 + x_2 + x_3 + 2x_4 - x_5 - x_6 - x_7 + 2 \equiv 0 mod 2 \tag{2.11}$$

As a check, consider the molecular Signature of PVC [x_1,x_2,x_3,x_4,x_5,x_6,x_7] = [0,1,1,0,1,3,0], where the values of x_i is the occurrence number of atomic Signature i.

$$0 + 1 + 1 + 2 \cdot 0 - 1 - 3 - 0 + 2 = 0 \tag{2.12}$$

Hereby each atom in the reconstructed PVC has the correct valence. Instead consider the graphicality equation of the molecular Signature [x_1,x_2,x_3,x_4,x_5,x_6,x_7] = [0,0,0,1,0,0,5], this is not one of the two molecules presented in the training set, but originates from an ethane molecule with an additional x_1 atomic Signature.

$$-0 - 0 + 0 + 2 \cdot 1 - 0 - 0 - 5 + 2 = -1 \tag{2.13}$$

This molecular Signature does not satisfy the graphicality equation and as a result it is a disconnected graph and therefore discarded.

The next step is the construction of the consistency equations, one for each bond type, by using equations 2.9-2.18.

$$\text{C-B bonding:} \quad -x_1 + x_4 = 0 \tag{2.14}$$

$$\text{B-B bonding:} \quad x_1 + x_2 + x_3 \equiv 0 mod 2 \tag{2.15}$$

$$\text{B-H bonding:} \quad -x_1 - x_2 - 2 \cdot x_3 + x_6 = 0 \tag{2.16}$$

$$\text{B-Cl bonding:} \quad -x_2 + x_5 = 0 \tag{2.17}$$

$$\text{C-H bonding:} \quad -3 \cdot x_4 + x_7 = 0 \tag{2.18}$$

The operational signs dictate the parent/child relationship in each atomic Signature and the prefix is the time each child atom appears in an atomic Signature. As a check, again consider the molecular Signature of PVC [x_1,x_2,x_3,x_4,x_5,x_6,x_7] = [0,1,1,0,1,3,0] and the above equations can be satisfied resulting in equation 2.19-2.23.

$$\text{C-B bonding: } -0+0=0 \tag{2.19}$$
$$\text{B-B bonding: } 0+1+1=2 \tag{2.20}$$
$$\text{B-H bonding: } -0-1-2\cdot 1+3=0 \tag{2.21}$$
$$\text{B-Cl bonding: } -1+1=0 \tag{2.22}$$
$$\text{C-H bonding: } -3\cdot 0+0=0 \tag{2.23}$$

Thus the 4 atomic Signatures representing PVC are bonded in such a way that all bonds in each atomic Signatures align forming a connected graph.

The last constraint equation is the PRU equation, which dictates that the sum of atomic Signatures containing repeating parent atoms must be equal to 2. In the case of this example, the PRU equation takes the form of equation 2.24.

$$x_1+x_2+x_3=2 \tag{2.24}$$

In case of PVC, the equation equals 2 confirming the representation of PVC in terms of atomic Signatures.

Generation of new molecular Signatures

In this section the brute-force method developed by Weis and Visco (2010) [15] will be demonstrated in order to generate new molecular Signatures by solving the 5 constraint equations, the PRU equation and the graphicality equation. As described in section 2.2.4 the equation that contains atomic Signatures with the least amount of values are enumerated first. For this case, the min/max occurrence values for each atomic Signature is illustrated in Table 2.2.

Table 2.2: The min/max occurrence numbers for the unique atomic Signatures for the training set obtained with PP and PVC.

	x_1	x_2	x_3	x_4	x_5	x_6	x_7
Min	0	0	1	0	0	3	0
Max	1	1	1	1	1	3	3

The first equation to be solved is the C-B consistency equation, since the sum of occurrence values, as well as in the equations of B-B, B-Cl and C-H bonding, is 4. This is the lowest amount of iterations, 2·2 = 4, observed for the set of equations. The C-B consistency equation is solved by exhausting the atomic Signatures, as illustrated in equation 2.25-2.29.

$$-x_1 + x_4 = 0 \tag{2.25}$$
$$-0+0=0 \tag{2.26}$$
$$-0+1=1 \tag{2.27}$$
$$-1+0=-1 \tag{2.28}$$
$$-1+1=0 \tag{2.29}$$

Two solutions satisfies the B-C consistency equation and the corresponding values of x_1 and x_4 therefore ensures that C-B bonds in a molecular Signature will align. It is important to note that only the two combinations of x_1 and x_4 can coexist otherwise the B-C bonds will not align. The two solutions are the start of two new molecular Signatures, which is illustrated in Table 2.3.

Table 2.3: Illustrates the not yet finished molecular Signature of the two solutions.

Solution #	x_1	x_4
1	1	1
2	0	0

Next the B-B bonding consistency equation is evaluated. This equation contains the atomic Signatures x_1, x_2 and x_3 and since both values of x_1 were valid in the B-C equation, both are used here. The equation therefore results in 2·2·1 = 4 iterations, as illustrated in equation 2.30-2.34.

$$x_1 + x_2 + x_3 \equiv 0 mod 2 \tag{2.30}$$
$$0+0+1=1 \tag{2.31}$$
$$1+0+1=2 \tag{2.32}$$
$$0+1+1=2 \tag{2.33}$$
$$1+1+1=3 \tag{2.34}$$

The B-B bonding constraint equations resulted in 2 valid equations. The corresponding values from these equations are then added to the two molecular Signatures, as shown in Table 2.4.

Table 2.4: Illustrates the not yet finished molecular Signature of the two solutions.

Solution #	x_1	x_2	x_3	x_4
1	1	0	1	1
2	0	1	1	0

Next the B-H bonding consistency equation is solved, but since the first three of the atomic Signatures have been represented in the previous consistency equations and only the two combinations presented in Table 2.4 validate the B-C and B-B consistency equation the B-H bonding consistency equation is therefore only solved for the two molecular Signatures by adding the value of x_6 to the two equations. This is presented in equation 2.35-2.37.

$$-x_1 - x_2 - 2 \cdot x_3 + x_6 = 0 \tag{2.35}$$
$$-1 - 0 - 2 \cdot 1 + 3 = 0 \tag{2.36}$$
$$-0 - 1 - 2 \cdot 1 + 3 = 0 \tag{2.37}$$

The value of x_6 satisfied both of the two molecular Signatures resulting in Table 2.5.

Table 2.5: Illustrates the not yet finished molecular Signature of the two solutions.

Solution #	x_1	x_2	x_3	x_4	x_6
1	1	0	1	1	3
2	0	1	1	0	3

Next is the B-Cl consistency equation is solved. The equation contains the atomic Signatures x_2 and x_5 which each have two values resulting in 2 · 2 = 4 iteration, as demonstrated by equation 2.38-2.42.

$$-x_2 + x_5 = 0 \tag{2.38}$$
$$-0 + 0 = 0 \tag{2.39}$$
$$-1 + 0 = -1 \tag{2.40}$$
$$-0 + 1 = 1 \tag{2.41}$$
$$-1 + 1 = 0 \tag{2.42}$$

The B-Cl consistency equation resulted in 2 valid equation and the corresponding values of which are added to the molecular Signatures, as depicted in Table 2.6.

Table 2.6: Illustrates the not yet finished molecular Signature of the two solutions.

Solution #	x_1	x_2	x_3	x_4	x_5	x_6
1	1	0	1	1	0	3
2	0	1	1	0	1	3

The last consistency equation is the one ensuring the alignment of C-H bonding. This equation contains the atomic Signatures x_4 and x_7 and since both x_4 values have been validated by the previous consistency equation both are applied in the C-H bonding equation. The atomic Signature x_7 contains 4 values: 0, 1, 2 and 3, as illustrated in Table 2.2, resulting in 2·4 = 8 iterations, as illustrated in equation 2.43-2.51.

$$-3 \cdot x_4 + x_7 = 0 \tag{2.43}$$
$$-3 \cdot 0 + 0 = 0 \tag{2.44}$$
$$-3 \cdot 0 + 1 = 1 \tag{2.45}$$
$$-3 \cdot 0 + 2 = 2 \tag{2.46}$$
$$-3 \cdot 0 + 3 = 3 \tag{2.47}$$
$$-3 \cdot 1 + 0 = -3 \tag{2.48}$$
$$-3 \cdot 1 + 1 = -2 \tag{2.49}$$
$$-3 \cdot 1 + 2 = -1 \tag{2.50}$$
$$-3 \cdot 1 + 3 = 0 \tag{2.51}$$

As the equations show only 2 of the occurrence values combined satisfies the consistency equation and the corresponding two values of x_7 are added to the molecular Signatures, as shown in Table 2.7.

Table 2.7: The two solved molecular Signatures.

Solution #	x_1	x_2	x_3	x_4	x_5	x_6	x_7
1	1	0	1	1	0	3	3
2	0	1	1	0	1	3	0

By appling the brute-force method developed by Weis and Visco (2010) [15] to the training set based on PP and PVC resulted in two molecular Signatures, as illustrated in Table 2.7. The next step is to guarantee that these two molecular Signatures are linear homopolymers and that the valence of each atom is meet. First, the PRU equation is implemented as illustrated in equation 2.52-2.54.

$$x_1 + x_2 + x_3 = 2 \tag{2.52}$$
$$1 + 0 + 1 = 2 \tag{2.53}$$
$$0 + 1 + 1 = 2 \tag{2.54}$$

Both equations are satisfied hereby confirming that both molecular Signatures are linear homopolymers. Next, the graphicality equation is implemented and again both molecular Signatures satisfy the equation, as illustrated below.

$$x_1 + x_2 + x_3 + 2 \cdot x_4 - x_5 - x_6 - x_7 + 2 \equiv 0 mod 2 \tag{2.55}$$
$$1 + 0 + 1 + 2 \cdot 1 - 0 - 3 - 3 + 2 = 0 \tag{2.56}$$
$$0 + 1 + 1 + 2 \cdot 0 - 1 - 3 - 0 + 2 = 0 \tag{2.57}$$

As explained in the above, solving the seven constraint equations by the brute-force method developed by Weis and Visco (2010) [15] resulted in two molecular Signatures, which satisfied the equations by 26 iterations. Comparing this number of iterations to a truly brute-force method, which then would be the product of range for each of the seven atomic Signatures, resulting in 2·2·1·2·2·1·4 = 64 iterations. The implementation thus reduced the number of iterations by more than half hereby ensuring an efficient computational time when applying the method to larger training sets.

Structure generation

At this point a descriptor matrix of solutions, Table 2.7, have been generated and the next step is to transform the two molecular Signatures into 2D molecular structures. If one however compares the two solved molecular Signatures, Table 2.7, with the atomic Signatures of PP and PVC from Figure 2.6, it is obvious that these are the same molecular Signatures. For simplicity only the translation of the molecular Signature of PP $[x_1,x_2,x_3,x_4,x_5,x_6,x_7]=[1,0,1,1,0,3,3]$ will be demonstrated. As described in section 2.2.5 a molecular Signature can result in multiple 2D molecular structures and in order to identify the 2D structures a method developed by Faulon et al. (2003) [20] was utilized. It is this method that is presented here.

The reconstruction of a molecular Signature starts with atomic Signatures only containing the parent atoms, that is with no bonds. Bonds are then added in all possible means to saturate the valence of all atoms in the molecular Signature, which is performed in the order of the atom with the lowest valence to the atom of highest valence. This is depicted on Figure 2.7, where the parent atoms in each atomic Signature of PP is 3·H, 3·H, B, B and C.

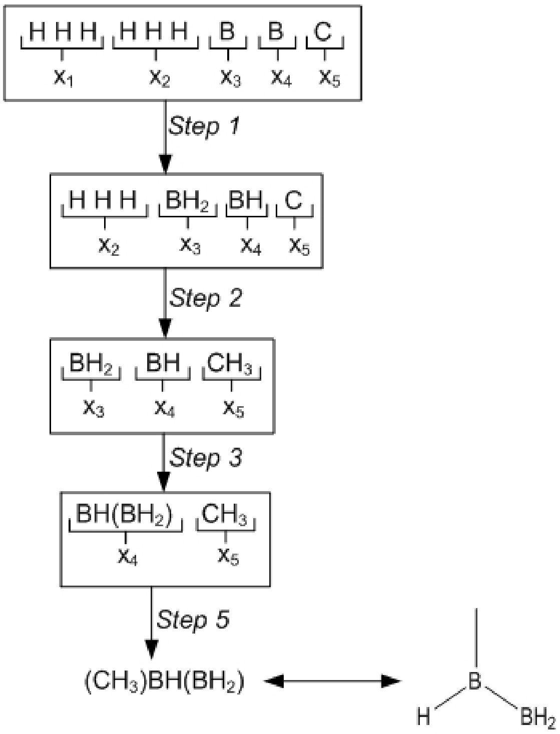

Figure 2.7: Illustrates the translation of PP using the method developed by Faulon et al. (2003) [20].

The hydrogen atoms of x_1 are saturated first, step 1, by matching the child of x_1 with parents of the remainder atomic Signatures. The child of x_1 is boron which is the parent of both x_3 and x_4. Next, the occurrence of hydrogen atoms in x_3 and x_4 is checked, thus occurring two times in x_3 and once in x_4 hereby in total occurring three times. This matches the occurrence number of x_1 and the respective atomic Signatures are connected.
Next, hydrogen atoms in the atomic Signature x_2 are saturated, step 2, and the child of x_2 is carbon which occurs as the parent of x_5. In x_5 hydrogen occurs three times as a child which matches the occurrence number of x_2 and the two Signatures are therefore combined.
Next, the carbon atom of signature x_3 is saturated, step 3 in Figure 2.7 and the children of x_3, see Figure 2.6, is 2 hydrogen atoms and a carbon atom and since the two hydrogen atoms have been attached makes the boron atom the missing atom. x_3 is therefore connected with x_4, as it is the only atomic Signature containing boron and due to the alignment of atomic Signatures.
The last step, step 5, is to saturate the parent boron atom of the atomic signature x_4. x_4 is already bonded with a hydrogen atom and a BH_2 group, hereby making the remaining atom carbon. x_5 contains a parent carbon and has a boron as a child, the two atomic Signatures are therefore connected, resulting in a connected graph, i.e. the molecule poly(propylene).

2.3 Electrospinning

Electrospinning is an application, which is capable at producing polymer fibers in the nanometer diameter range whereas other fiber spinning techniques such as wet-, dry-, melt- and gel spinning only is capable at producing polymer fibers with diameters in the micrometer scale. Nanofibers are notable due to their large surface area to volume which has shown to be effective in applications such as filtrations, sensors, protective clothing, nanofiber reinforced composites, conductive fibers, tissue engineering, catalysts, drug delivery etc. [23] [24].
Electrospinning can be considered as a variant of the electrospraying process, known from its application in mass spectroscopy, since both techniques involve the use of a high voltage to induce the formation of a liquid jet. In electrospray the liquid jet is broken up, which often is a result of the solutions low viscosity yielding in the formation of small drops. In electrospinning on the other hand the liquid jet is continuously stretched due to a higher viscosity liquid hereby resulting in electrostatic repulsions between the surface charges and in the evaporation of solvent, which yields in the production of solid fibers [25].

Figure 2.8 illustrates a basic electrospinning setup. Its main components consists of a high voltage power supply connected to a capillary tube with a small diameter needle and a grounded metal collector, which for example can be covered with a fabric. A direct current power supply is most often used due to its simplicity although experiments have been conducted with alternating current. The capillary tube is charged with a polymer solution and with the use of a syringe pump, the solution can be fed through the capillary tube with a constant and controllable rate. When a high voltage, typically 1-30 kV, is applied, the pendent polymer drop at the nozzle of the needle will become highly electrified hereby inducing evenly distributed charges at the surface of the drop [25].

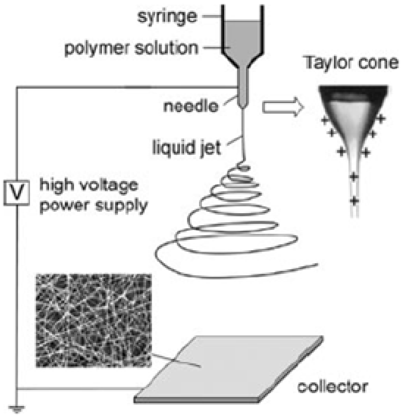

Figure 2.8: A schematic representation of the electrospinning process. Note that the distance from the tip of the needle to the collector is termed the gap distance [25].

The liquid drop hereby experience two major kinds of electrostatic forces: the electrostatic repulsion between the surface charges and columbic forces produced by the external field. As the intensity of the electric field is increased a critical value is attained when the electrostatic forces overcome the surface tension of the polymer solution. This will cause the polymer droplet to suspend from the hemispherical shape to eject from the nozzle into a conical shape, knwon as the Taylor cone. The electrified polymer solution jet then undergoes a stretching and whipping process resulting in the evaporation of solvent and in charged polymer fibers. These fibers then undergo a region of stretching where the diameter can be reduced from as much as hundreds of micrometers to as small as tens of nanometers before being deposited as randomly orientated fibers on the grounded collector. During the stretching of the polymer jet another phenomenon known as splaying can occur. Here the electrostatic forces overcome the cohesive forces of the jet resulting in the jet splitting into multiple polymer jets [25] [23]. Figure 2.9 illustrates electrospun poly(styrene-co-dimethylsiloxane) nanofibers.

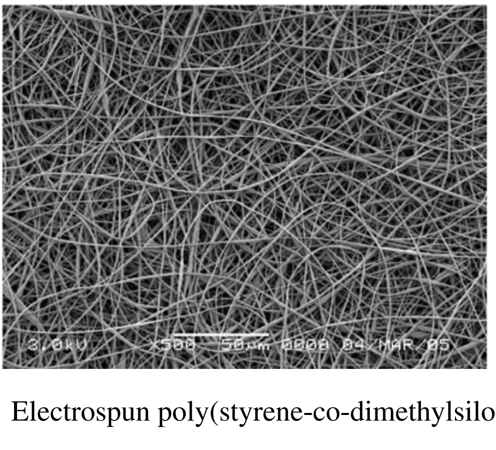

Figure 2.9: Electrospun poly(styrene-co-dimethylsiloxane) [26].

Various investigations have been conducted on controlling the morphology of the electrospun polymer fibers. In general each polymer behaves differently, as a result of its molecular weight, polydispersity index, branching, functional groups. Properties such as conductivity, viscosity and surface tension also influence the process as well as the electric potential, flow rate, polymer concentration, gap distance, temperature, humidity, air velocity and type of collector have influence on the formation of fibers. In total this sums up to some 14 different parameters affecting the morphology of the electrospun fibers, which through theory and experience have shown some general trends. In order electrospin fibers from a polymer solution, the solution must have a surface tension low enough, a charge density and viscosity high enough in order to prevent the jet from collapsing into droplets before the solvent has evaporated. Other parameters such as the gap distance have shown to mainly affect the morphology while decreasing the electric field has shown to yield in beaded fibers independent of the polymer concentration. The polymer concentration has shown to strongly affect the fiber size distribution, as the fibers diameter increases as function of the polymer concentration. While some general guidelines are known, there is always exceptions to the rule and investigations of novel electrospun materials should therefore always be conducted [23].

3. Project aim

The objective of this project was to produce a novel filter material with improved separation performance for the separation of secondary dispersed water droplets in diesel fuel.
This project therefore includes considerations on identifying and producing a novel filter material with super hydrophobic properties and investigating the separation efficiencies as function of the hydrophobicity:

- The first aim of this project is to identify structural components of polymers that govern the hydrophobicity and generate new polymeric structures with super hydrophobic properties by developing an inverse-quantitative structure-activity relationship.
  - First, two models will be developed one based on water contact angles of flat polymer surfaces and a second on the basis of critical surface tensions.
  - Second, a selected polymer will be purchased based on the results from the best performing model.
- The second aim of this project is to verify the inverse-QSAR models.
  - This should be done by either investigating the water contact angle or the critical surface tension on flat polymer surfaces of the selected polymer.
- The projects third aim is to investigate the electrospinning ability of the selected polymer, hereby possibly increasing the hydrophobicity of the material.
  - First, this should be done by varying the following electrospinning parameters: the polymer concentration, choice of solvent, flow rate, gap distance and voltage. The morphology of samples should be investigated by SEM to identify if fibers or drops were formed.
  - Second, the relationship between fiber size distributions and selected electrospinning conditions should be investigated.
- The projects fourth aim is to investigate the relationship between the fiber size distribution, deposited fiber and the hydrophobicity.
  - This should be done by varying the polymer concentration, flow rate, gap distance and the weight of deposited fiber. The fiber size distribution and hydrophobicity of the produced fibers should be characterized by SEM and the contact angles, respectively.
- The fifth aim of this project is to obtain superhydrophobic membranes with improved seperation performances.
  - This should be done by electrospinning various amounts of the selected polymer by various electrospinning conditions onto a support material. The separation efficiencies and pressure drops across the membranes should be investigated during the liquid/liquid coalescence filtrations.

4. Materials and methods

In this chapter the preparations, equipment and experimental conditions used in the experimental work will be presented.

4.1 Inverse-quantitative structure-activity relationship

In order to construct new polymeric structures with improved hydrophobicity, two i-QSAR models were developed based on two different training sets. The first model contained the water contact angles of 44 polymer films, which are depicted in Table 4.1 and Table 4.2. The second model was based on the critical surface tensions of polymers and consisted of 39 polymers, which is depicted in Table 4.3.

Table 4.1: The first part of the training set for the i-QSAR model containing water contact angles. Abb. is short for abbrivation and θ is the contact angle [degree].

Polymer	Abb.	θ	Reference
Cellulose acetat	CA	45.9	[27]
Poly(vinyl alcohol)	PVOH	51.0	[28]
Poly(tetrafluoroethylene)	PTFE	58.0	[29]
Poly(vinyl acetate)	PVA	60.6	[28]
Nylon 11	PA-11	61.0	[30]
Poly(ethylene oxide)	PEO	63.0	[28]
Poly(caprolactam)	Nylon 6	63.0	[30]
Poly(ethylene-co-vinyl alcohol)	EVOH	65.0	[31]
Poly(caprolactone)	PCL	69.0	[32]
Poly(sulfone)	PSU	70.5	[28]
Poly(metacrylate)	PMMA	70.9	[28]
Nylon 6,6	PA-6,6	72.0	[27]
Poly(ethylene terephthalate)	PET	72.5	[28]
Poly(d,l-lactide-co-glycolide)	PLGA	74.5	[33]
Poly(ether imide)	PEI	75.0	[34]
Poly(oxymethylene)	POM	76.8	[28]
Poly(vinylidene chloride)	PVDC	80.0	[28]
Poly(p-phenylene sulfide)	PPS	80.3	[28]
Poly(carbonate)	PC	82.0	[28]
Poly(ether ether ketone)	PEEK	83.3	[35]
Poly(vinyl fluoride)	PVF	84.5	[28]
Poly(lactic acid)	PLA	85.0	[33]
Poly(vinyl chloride)	PVC	85.6	[28]
Poly(styrene)	PS	87.0	[28]

Table 4.2: The second part of the training set for the i-QSAR model containing water contact angles. Abb. is short for abbrivation and θ is the contact angle [degree].

Polymer	Abb.	θ	Reference
Poly(urethane)	PU	87.0	[36]
Poly(epichlorohydrin)	PECH	87.0	[37]
Poly(benzimidazole)	PBI	88.0	[38]
Poly(vinylidene flouride)	PVDF	89.0	[28]
Poly(vinylidenefluoride-co-hexafluoropropylene)	PVDF/HFP	90.0	[28]
Poly(n-butyl methacrylate)	PnBMA	91.0	[28]
Poly(trifluoroethylene)	-	92.0	[28]
Poly(butadiene)	-	96.0	[28]
Poly(ethylene)	PE	96.0	[28]
Butadiene-acrylonitrile	NBR	97.0	[37]
Poly(chlorotrifluoroethylene)	PCTFE	99.9	[28]
Poly(acrylonitrile)	PAN	100.8	[39]
Ethylene propylene rubber	EPR	105.0	[37]
Poly(dimethylsiloxane)	PDMS	107.2	[28]
Poly(4-methyl-1-pentene)	-	108.0	[28]
Poly(t-butyl methacrylate)	PtBMA	108.1	[28]
Fluorinated ethylene propylene	FEP	108.5	[28]
Poly(tetrafluoroethylene-co-hexafluoropropylene)	TFE/HFP	111.0	[40]
Poly(propylene)	PP	112.0	[27]
Poly(isobutylene)	-	112.1	[28]

Table 4.3: The training set for the i-QSAR model containg critical surface tensions. All of the CST are from [41]. Abb. is short for abbrivation and CST is the critical surface tension [mJ/m^2].

Polymer	Abb.	CST	Polymer	Abb.	CST
Poly(hexafluoropropylene)	HFP	16.9	Poly(phenyl methacrylate)	PPhMA	35.0
Fluorinated ethylene polypropylene	FEP	19.1	Poly(epichlorohydrin)	PECH	35.0
Poly(tetrafluoroethylene)	PTFE	19.4	Poly(vinyl acetate)	PVA	35.3
Poly(stearyl methacrylate)	PSMA	20.8	Nylon 11	PA-11	35.6
Poly(lauryl methacrylate)	PLMA	21.3	Poly(benzyl methacrylate)	PBMA	36.0
Polyoctyl methacrylate	POMA	23.5	Poly(vinyl alcohol)	PVOH	37.0
Poly(trifluoroethylene)	-	26.5	Poly(oxymethylene)	POM	37.0
Poly(isobutylene)	PIB	27.0	Cellulose acetate	CA	37.5
Poly(hexyl methacrylate)	PHMA	27.5	Poly(methyl methacrylate)	PMMA	37.5
Poly(butadiene)	-	29.3	Poly(vinyl chloride)	PVC	37.9
Poly(n-butyl methacrylate)	-	29.8	Poly(p-phenylene sulfide)	PPS	38.0
Poly(propylene)	PP	30.5	Poly(ethylene terephthalate)	PET	39.0
Poly(chlorotrifluoroethylene)	PCTFE	30.8	Poly(vinylidene chloride)	PVDC	40.2
Poly(2-ethylhexyl acrylate)	P2EA	31.0	Poly(sulfone)	PSU	42.1
Poly(vinylidene fluoride)	PVDF	31.6	Nylon 6,6	-	42.2
Poly(ethylene)	PE	31.6	Poly(caprolactam)	Nylon 6	43.9
Poly(vinyl fluoride)	PVF	32.7	Poly(carbonate)	PC	44.0
Poly(ethyl methacrylate)	PEMA	32.8	Poly(phenylene oxide)	PPO	47.0
Poly(styrene)	PS	34.0	Cellulose triacetate	CtA	48.8
Poly(acrylamide)	-	34.3			

The i-QSAR analysis of the two training sets were conducted, as described in section 2.2 and will therefore not be detailed futher in this section.

4.2 Materials

The i-QSAR analysis resulted in the purchase of poly(styrene-co-α-methylstyrene), PSMS, from Sigma Aldrich. The weighted average, M_w and number average, M_n, molecular weight were 2800 and 800 g/mol, respectively (M_w/M_n = 3.5). Cyclohexane (99.0 %) was purchased from Acros, N,N-dimethylformamide, DMF, (99.8 %) from EMD Chemicals, ethanol (Anhydrous) from Pharmaco-AAPER, tetrahydrofurane, THF, (99 %), hexane (95 %), formaide (99.5 %) and 2-ethoxyethanol (99 %) were purchased from Sigma Aldrich.

4.3 Vertification of inverse-quantitative structure-activity relationship

The i-QSAR analysis only resulted in generated structures for the CST model and in the purchase of PSMS. This model could therefore be validated by experimentally determining the CST of PSMS and comparing this value with the CST generated by the model. The CST of PSMS was determined by measuring the contact angle of 7 different ratios of formamide and 2-ethoxyethanol, as illustrated in Table 4.4.

Table 4.4: Lists the volumetric ratios of formamide and 2-ethoxyethanol and their corresponding liquid/vapor interfacial tensions, which was aquired from Dann (1969) [14].

Formamide/2-ethoxyethanol [V/V %]	γ_{lv} [mJ/m^2]
1.00/0.00	58.3
0.99/0.01	56.3
0.75/0.25	43.0
0.49/0.51	36.5
0.34/0.66	34.2
0.19/0.81	31.3
0.03/0.97	28.8

A PSMS surface was prepared by evenly spreading a 60 w/w % PSMS/DMF solution onto a 7.5x2.5 cm glass slide (Fisher Scientific) and letting it dry in a hood. The contact angle of each solvent was measured with a contact angle goniometer (DSA 100, Krüss GmbH, Germany) in triplets by applying 3 drops with a volume of 5 μL onto the PSMS surface. Each drop was analyzed by the "sessile-drop" method by the software: Drop Shape Analysis version 1.91.0.2, where the contact angle was measured on the left and right of the drop resulting in an average contact angle. This was done for each of the 3 drops yielding in an average contact angle for each solvent.

4.4 Electrospinning setup

This section describes the electrospinning setup used for all electrospun samples and is depicted in Figure 4.1

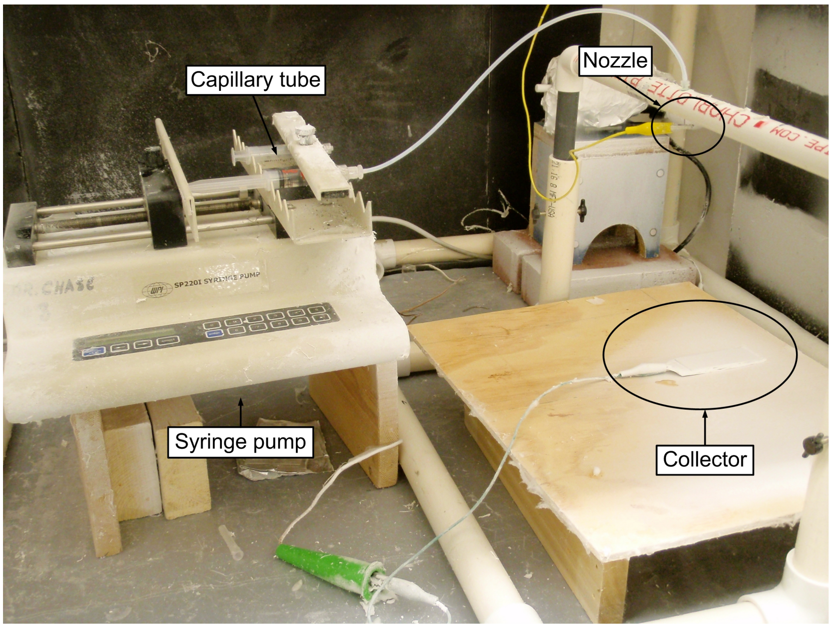

Figure 4.1: The electrospinning setup used at The University of Akron.

The setup consists of a syringe pump (WPI, SP220i syringe pump) with a flow range of 10^{-6}-4260 mL/hr. A 5 mL syringe was placed in the syringe pump, which was charged with polymer solutions. In order to orientate the flow of the fibers vertically, the needle of the syringe was connected by teflon tubing as depicted in the figure. A DC high voltage supply (ES30P, Gamma high voltage research) was used to generate the potential difference between the needle and collector, which unless otherwise stated was aluminum foil. The voltage supply is not in included in the picture.

4.5 Electrospinning of poly(styrene-co-α-methylstyrene)

This section is divided into two subsections; the investigation of the electrospinning ability of PSMS and the investigation of the hydrophobicity of electrospun PSMS c.f. the project aim.

4.5.1 The investigation of the electrospinning ability of poly(styrene-co-α-methylstyrene)

The electrospinning ability of PSMS was investigated by preparing 3 stock solutions of 25, 35 and 50 w/w % PSMS in cyclohexane, 90/10 w/w % cyclohexane/THF and DMF, respectively. This resulted in 9 solutions and each was electrospun at 3 different flow rates: 1, 5 and 10 mL/hr, 2 different gap distances: 15 and 20 cm and 2 different voltages: 20 and 30 kV. This yielded in

a total of 108 samples.
The purpose of these samples was to investigate the electrospinning ability of PSMS. In order to rather rapidly investigate the 108 samples, only the polymer jet and the deposited material was investigated by the naked eye for fiber formation and if doubt the samples was investigated by microscope (Olympus SZ 6045 TRPT).

The relationship between selected electrospinning conditions and fiber size distributions was then investigated. This was done by electrospinning stock solutions of 15, 25, 35, 50, 52, 54, 56, 58 and 60 w/w % PSMS/DMF using selected electrospinning conditions, which was based on the above and is depicted in Table 4.5. The fiber size distributions were determined by examining the samples on a scanning electron microscope, SEM (TM-3000, Hitachi, Japan) and measuring the fiber diameter and fiber length using the software ImageJ (www.rsbweb.nih.gov/ij). The fiber size distributions were determined using the *length weighted fiber diameter* method as described by Varabhas et al. (2008) [42] and Dosunmu et al. (2006) [43], thus for each sample the fiber size distribution was determined on not fewer than a 100 fibers taken from at least 8 different SEM pictures. For beaded fibers the fiber diameter referes to the diameter of the treads between the beads.

Table 4.5: The selected electrospinning conditions were divided into three groups with varying flow rate and gap distance.

Group	1	2	3
Flow rate [mL/hr]	1	0.5	0.5
Gap distance [cm]	20	20	10
Voltage [kV]	30	30	30

4.5.2 The hydrophobicity of electrospun poly(styrene-co-α-methylstyrene)

In order to investigate the hydrophobicity of the electrospun fibers, PSMS was electrospun on the basis of the results of section 4.5.1. This resulted in the electrospinning of 54, 56, 58 and 60 w/w % PSMS/DMF using the 3 different electrospinning conditions from Table 4.5. The hydrophobicity was also investigated as a function of fiber deposition. This was done by electrospinning the solution onto 2.5x3.75 cm glass slides (Fisher Scientific) and fabricating a glass slide for each of the following fiber depositions: 10, 20, 30 and 40 g PSMS/m^2. This resulted in 48 samples of which the hydrophobicity was determined by measuring the water contact angle with a contact angle goniometer (DSA 100, Krüss GmbH, Germany) in triplets, as described in section 4.3.

4.6 Membrane manufacturing and characterization

The membranes fabricated was manufactured using the electrospinning setup previously described in section 4.4. Polymer solutions of 54 and 60 w/w % PSMS/DMF were electrospun into fibers using the group 2 and 1 electrospinning conditions from Table 4.5, respectively. Fibers were collected onto 11.4x11.4 cm glass fiber mats (Grade 8000166 Glass, Hollingsworth & Vose, mean fiber diameter of 6.50 μm) with 10, 20, 30 and 40 g PSMS/m^2 of collected fibers for the 54 w/w % PSMS/DMF solution and 30 and 40 g PSMS/m^2 for the 60 w/w % PSMS/DMF solution. The six different type of membranes are summarized in Table 4.6 and were chosen based on the results from the hydrophobicity investigations.

Table 4.6: Lists the data of the 6 different type of membranes. [PSMS] is the concentration of PSMS given in w/w %.

Membrane	[PSMS]	Electrospinning conditions	Fiber deposition [g/m^2]
A_{10}	54	Group 2	10
A_{20}	54	Group 2	20
A_{30}	54	Group 2	30
A_{40}	54	Group 2	40
B_{30}	60	Group 1	30
B_{40}	60	Group 1	40

The membranes were abbreviated as a series A and B and each series was electrospun at 54 and 60 w/w % PSMS/DMF using group 2 and 1 electrospinning conditions, respectively. The subscripts, 10-40, of each membrane describes the intended weight of deposited fibers and each type of membrane was fabricated in triplets yielding in a total of 18 membranes. The air permeability and porosity of each membrane was examined using a Fraizer test (FAP-HP, Fraizer) and an in house gas Pycnometer with pressureized air, respectively. The mean fiber diameter and hydrophobicity of each membrane was, due to the previous experiments, not investigated.

4.7 Liquid/liquid coalescence

The 6 different types of membranes, i.e. Table 4.6, was investigated for the separation of secondary dispersions of water-in-diesel. A schematic diagram of the experimental setup is shown on Figure 4.2. A mixture of water-in-diesel was used in the experiments, in which deionized water was dispersed in diesel in a concentration of 0.2/99.8 V/V % water/diesel. This solution was stored in the oil tank and before each run the fuel was vigorously stirred and was then pumped from the oil tank by a centrifugal fuel pump (Airtex ATX-E3309 GIC07D02 electric fuel pump) at a constant flow of 200 mL/min through the filter sample holder and into a storage tank. A loop was installed to control the flux through the membrane and at a flow rate of 200 mL/min the resulting flux was 0.92 $\frac{m^3}{m^2 \cdot hr}$. The flow through the loop into the oil tank was sufficient to maintain a table water-in-diesel emulsion through the conducted experiments and stirring was therefore not needed.

The fuel pump was switched on at least 10 min prior to opening valve 1 hereby obtaining a fine stable water-in-diesel emulsion with drop size distributions in the range of 0-60 μm.

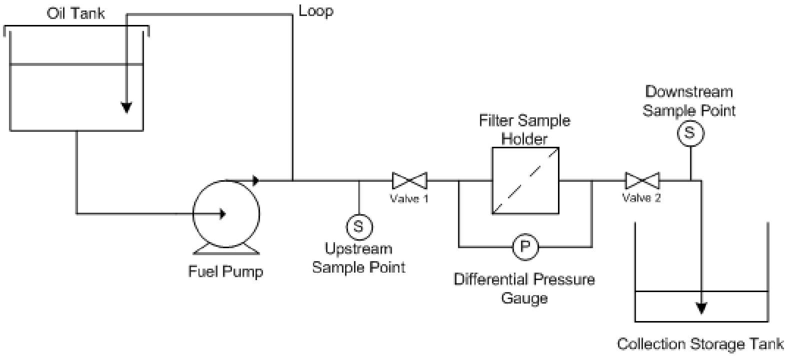

Figure 4.2: The filtration experimental apparatus.

The filter holder was machined out of Plexiglas^{TM} with an 11.4x11.4 cm opening for placement of the membrane samples, which was held in place by a stainless steel wire mesh screen. The filter holder is depicted in Figure 4.3 and each of the 18 membranes were only used once.
The filtrations was started by opening valve 1 when a stable drop size distribution was observed in the upstream. Downstream samples of 100 mL and pressure drops were then collected and noted every 10 min. until steady state was achieved. Drop size distributions of the collected samples were analyzed immediately after collection by dynamic light scatter using an Accusizer^{TM} 780 optical particle sizer. The Accusizer was cleaned between each scan using ethanol or hexane to achieve a threshold value of 250 counts/mL.

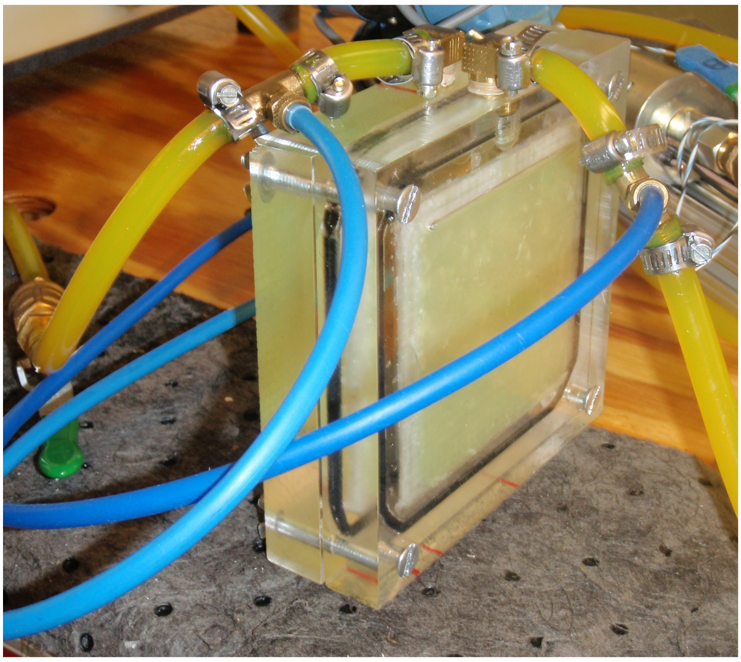

Figure 4.3: The filterholder used in the filtrations.

5. Results

This chapter contains the results from the i-QSAR models and the experimental work done in this project. To ease the reading the results will be presented in the same order as in the materials and method.

5.1 Inverse-quantitative structure-activity relantionship

In this section, the results of i-QSAR models based on a contact angle training set and a critical surface tension training set will be presented. To understand these results to full, the reader is referred to section 2.2 where theoretical aspects and a detailed example using only two polymers is presented.
In total 4 QSAR models were constructed by using height 1 and 2 atomic Signatures for each of the two training sets. On the basis of R^2 and q^2, as described in section 2.2.2, the best performing QSAR model was selected resulting in the construction of a single i-QSAR model.

5.1.1 Translation

The first step in the i-QSAR analysis was the translation of the 2D molecular structures into atomic Signatures, as illustrated in section 2.2.6. In order to do so, the repeating atoms of a repeating polymer unit needed to be replaced with a dummy atom. The repeating- and dummy atoms used in each of the two training sets are depicted in Table 5.1.

Table 5.1: Illustrates repeating- and dummy atoms used in the two training sets. "+" indicates that the combination is present in the training set while "-" indicates it as being absent.

θ	CST	Repeating atom	Dummy atom
+	+	C	B
+	+	N	Se
+	+	O	I
+	-	Si	Al
+	+	S	P
+	+	Aromatic Carbon	-Br

The translation of the contact angle training set, which consisted of 44 linear homopolymers was translated into height 1 atomic Signatures resulting in 96 unique atomic Signatures that are illustrated in Table 5.2.

Table 5.2: Illustrates the unique height 1 atomic Signatures translated for the contact angle training set. Significant atomic Signatures used in the QSAR analysis are marked with bold.

Variable	atomic Signature	Variable	atomic Signature	Variable	atomic Signature
x_{1}	[Al]([C][C][I])	x_{33}	[C]([B]t[N])	x_{65}	[C](p[C]p[C][S])
x_{2}	[B]([B][C][C])	x_{34}	[C]([Br]p[C]p[C])	x_{66}	[C](p[C]p[C]p[N])
x_{3}	[B]([B][C][H])	x_{35}	[C]([C]=[C][H])	x_{67}	[Cl]([B])
x_{4}	[B]([B][Cl][Cl])	x_{36}	[C]([C]=[O][Se])	x_{68}	[Cl]([C])
x_{5}	[B]([B][Cl][F])	x_{37}	[C]([C][C]=[O])	x_{69}	[F]([B])
x_{6}	[B]([B][Cl][H])	x_{38}	[C]([C][C][C][C])	x_{70}	[F]([C])
x_{7}	[B]([B][F][F])	x_{39}	[C]([C][C][C][H])	x_{71}	[H]([B])
x_{8}	[B]([B][F][H])	x_{40}	[C]([C][C][C][O])	x_{72}	[H]([C])
x_{9}	[B]([B][H][H])	x_{41}	[C]([C][C][H][H])	x_{73}	[H]([N])
x_{10}	**[B]([B][H][O])**	x_{42}	[C]([C][C][H][I])	**x_{74}**	**[H]([O])**
x_{11}	**[B]([C]=[O])**	x_{43}	[C]([C][C][H][O])	x_{75}	[H]([P])
x_{12}	[B]([C][C][F])	x_{44}	[C]([C][Cl][H][H])	x_{76}	[H]([Se])
x_{13}	[B]([C][C][H])	x_{45}	[C]([C][F][F][F])	x_{77}	[I]([Al])
x_{14}	[B]([C][F][F])	x_{46}	[C]([C][H][H][H])	x_{78}	[I]([B])
x_{15}	[B]([C][H][H])	x_{47}	[C]([C][H][H][I])	x_{79}	[I]([C])
x_{16}	[B]([C][H][O])	x_{48}	[C]([C][H][H][N])	x_{80}	[N]([B][C][H])
x_{17}	[B]([H][H][I])	x_{49}	[C]([C][H][H][O])	x_{81}	[N]([C][C][C])
x_{18}	[B]([N]=[O])	x_{50}	[C]([C][H][H][Se])	x_{82}	[N]([C][C][H])
x_{19}	[Br]([C])	x_{51}	[C]([C][I]=[O])	x_{83}	[N](p[C]p[C])
x_{20}	[C]([Al][H][H][H])	x_{52}	[C]([C][N]=[O])	x_{84}	[N](p[C]p[C][H])
x_{21}	[C]([B]=[C][H])	x_{53}	[C]([C][O]=[O])	x_{85}	[N](t[C])
x_{22}	[C]([B][C]=[O])	x_{54}	[C]([C]p[C]p[C])	x_{86}	[O](=[B])
x_{23}	[C]([B][C][C][F])	x_{55}	[C]([C]p[N]p[N])	x_{87}	[O](=[C])
x_{24}	[C]([B][C][F][F])	x_{56}	[C]([H][H][H][O])	x_{88}	[O](=[S])
x_{25}	[C]([B][C][H][H])	x_{57}	[C]([I][O]=[O])	x_{89}	[O]([B][C])
x_{26}	[C]([B][C][H][I])	x_{58}	[C]([N][O]=[O])	x_{90}	[O]([B][H])
x_{27}	[C]([B][C][H][O])	x_{59}	[C]([O][O]=[O])	x_{91}	[O]([C][C])
x_{28}	[C]([B][F][F][F])	**x_{60}**	**[C](p[C]p[C][H])**	x_{92}	[O]([C][H])
x_{29}	[C]([B][H][H][H])	x_{61}	[C](p[C]p[C][I])	x_{93}	[P]([C][H][H])
x_{30}	**[C]([B][H][H][I])**	x_{62}	[C](p[C]p[C][N])	x_{94}	[S]([C][C]=[O]=[O])
x_{31}	[C]([B][O]=[O])	x_{63}	[C](p[C]p[C][O])	x_{95}	[Se]([C][C])
x_{32}	[C]([B]p[C]p[C])	x_{64}	[C](p[C]p[C][P])	x_{96}	[Se]([C][H])

A QSAR model based on the same training set was created by translating the 2D molecular structures into height 2 atomic Signatures. The translation of the same 44 polymers hereby resulted in 248 unique height 2 atomic Signatures, which due to its sheer size only is presented on the enclosed CD saved as "Atomic Signatures.xlsx".

Next, the CST training set was translated into height 1 atomic Signatures. The translation of the 39 linear homopolymers resulted in 73 unique height 1 atomic Signatures, which are depicted in Table 5.3.

Table 5.3: Illustrates the unique height 1 atomic Signatures translated for the CST training set. Significant atomic Signatures used in the QSAR analysis are marked with bold.

Variable	atomic Signature	Variable	atomic Signature	Variable	atomic Signature
x_{1}	[B]([B][C][C])	x_{26}	[C]([B]p[C]p[C])	**x_{50}**	**[Cl]([B])**
x_{2}	[B]([B][C][F])	x_{27}	[C]([Br]p[C]p[C])	x_{51}	[Cl]([C])
x_{3}	[B]([B][C][H])	x_{28}	[C]([C][C][C][C])	**x_{52}**	**[F]([B])**
x_{4}	[B]([B][Cl][Cl])	x_{29}	[C]([C][C][C][H])	**x_{53}**	**[F]([C])**
x_{5}	[B]([B][Cl][F])	**x_{30}**	**[C]([C][C][H][H])**	**x_{54}**	**[H]([B])**
x_{6}	[B]([B][Cl][H])	x_{31}	[C]([C][C][H][I])	x_{55}	[H]([C])
x_{7}	**[B]([B][F][F])**	x_{32}	[C]([C][C][H][O])	x_{56}	[H]([N])
x_{8}	[B]([B][F][H])	x_{33}	[C]([C][Cl][H][H])	x_{57}	[H]([O])
x_{9}	[B]([B][H][H])	**x_{34}**	**[C]([C][H][H][H])**	x_{58}	[H]([P])
x_{10}	[B]([B][H][O])	x_{35}	[C]([C][H][H][I])	x_{59}	[H]([Se])
x_{11}	[B]([C]=[O])	x_{36}	[C]([C][H][H][N])	x_{60}	[I]([B])
x_{12}	[B]([C][C][F])	**x_{37}**	**[C]([C][H][H][O])**	x_{61}	[I]([C])
x_{13}	[B]([C][F][F])	x_{38}	[C]([C][H][H][Se])	x_{62}	[N]([C][C][H])
x_{14}	**[B]([C][H][H])**	x_{39}	[C]([C][H][I][O])	x_{63}	[N]([C][H][H])
x_{15}	[B]([H][H][I])	x_{40}	[C]([C][N]=[O])	x_{64}	[O](=[B])
x_{16}	[Br]([C])	x_{41}	[C]([C][O]=[O])	x_{65}	[O](=[C])
x_{17}	[C]([B]=[C][H])	**x_{42}**	**[C]([C]p[C]p[C])**	x_{66}	[O](=[S])
x_{18}	[C]([B][C]=[O])	x_{43}	[C]([H][H][H][O])	x_{67}	[O]([B][C])
x_{19}	[C]([B][C][F][F])	x_{44}	[C]([I][O]=[O])	x_{68}	[O]([B][H])
x_{20}	**[C]([B][C][H][H])**	x_{45}	[C](p[C]p[C][H])	**x_{69}**	**[O]([C][C])**
x_{21}	[C]([B][C][H][I])	x_{46}	[C](p[C]p[C][I])	x_{70}	[O]([C][H])
x_{22}	[C]([B][F][F][F])	**x_{47}**	**[C](p[C]p[C][O])**	x_{71}	[P]([C][H][H])
x_{23}	**[C]([B][H][H][H])**	x_{48}	[C](p[C]p[C][P])	x_{72}	[S]([C][C]=[O]=[O])
x_{24}	[C]([B][N]=[O])	x_{49}	[C](p[C]p[C][S])	x_{73}	[Se]([C][H])
x_{25}	[C]([B][O]=[O])				

An additional QSAR model based on CST was also developed on the basis of the height 2 atomic Signatures. The translation of the 39 linear homopolymers hereby resulted in 183 unique atomic Signatures, which also only are presented on the enclosed CD saved as "Atomic Signatures.xlsx".

5.1.2 Quantitative structure-activity relantionship analysis

The next step was to create a QSAR model with a sufficient level of correlative and predictive capability. This was done by first creating four descriptor matrices, one for each model. This is a matrix where the rows are the polymers, the columns are the unique atomic Signatures and the entries are the occurrence number of a particular atomic Signature of a particular polymer. Again due to the sheer number of atomic Signatures, the descriptor matrices are only presented on the enclosed CD saved as "Descriptor matrices.xlsx".

The QSAR analysis took the form of a MLR equation, as described in section 2.2.2, and the analysis of the different descriptor matrices was conducted in the following order:

- Contact angle height 1 atomic Signatures
- Contact angle height 2 atomic Signatures
- CST height 1 atomic Signatures
- CST height 2 atomic Signatures

Contact angle

The QSAR analysis was, as described in the above, calculated on the basis of a descriptor matrix. The descriptor matrix for the height 1 atomic Signature contained 45 rows and 97 columns, one column for the contact angles and 96 columns for the unique atomic Signatures. The QSAR equation was however only calculated on the basis of 44 atomic signatures hereby removing 55 atomic Signatures in order to perform LOOCV. The most significant atomic Signatures were then added one at a time, on the basis of the F-statistics. The R^2 and q^2 values were calculated for each step resulting in Figure 5.1, which depicts the R^2 and q^2 values as function of the number of independent variables, i.e. atomic Signatures.

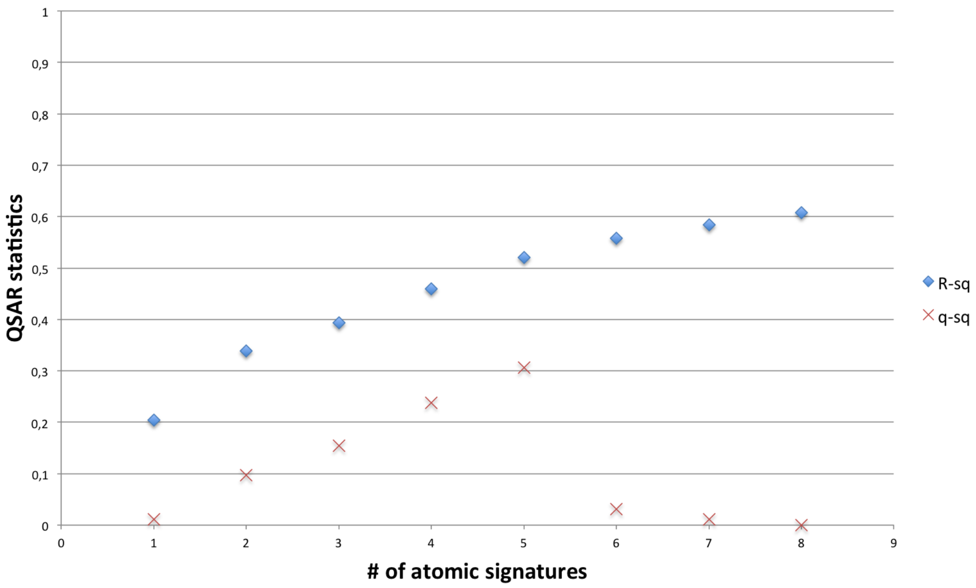

Figure 5.1: The impact of contact angle height 1 atomic Signatures on the QSAR statistics, which is plotted as function of the number of independent variables.

Notice that the R^2 increases as additional independent variables are added, while q^2 begins to drop after 5 atomic Signatures. For this project the QSAR equation should contain as many atomic Signatures as possible to cover the variety of the training set. The number of atomic Signatures in the final model was therefore chosen on the basis of the model with the highest q^2 value and as depicted in Figure 5.1, the best performing model included 5 atomic Signatures. This model hereby obtained a R^2 value of 0.52 and a q^2 value of 0.31. The structure of the 5 atomic signatures and hereby the 2D molecular structures included in the QSAR model to predict contact angle are marked with bold in Table 5.2. As a result of performing MLR on the 5 unique height 1 atomic Signatures, equation 5.1 took form, presenting the atomic Signatures from most to least significant.

$$\theta = 93.609 - 16.183 \cdot x_{74} - 22.508 \cdot x_{11} - 29.403 \cdot x_{10} - 1.102 \cdot x_{60} - 30.609 \cdot x_{30} \tag{5.1}$$

Using the QSAR equation to predict the contact angle of the polymers in the same training set and plotting these values against the experimental data, resulted in Figure 5.2.

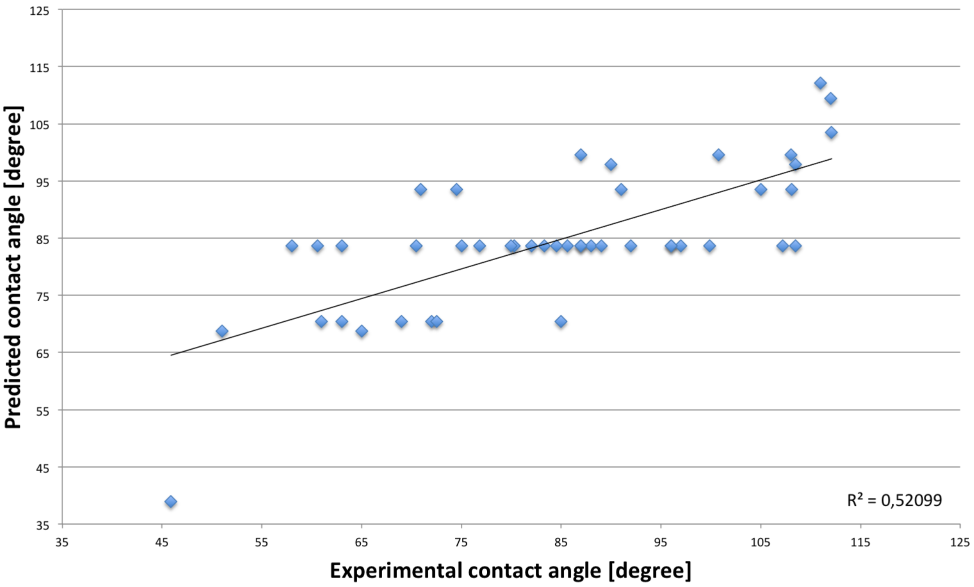

Figure 5.2: The experimental- versus predicted values for QSAR model based on the contact angle training set using height 1 atomic Signatures.

Next, a QSAR equation using the contact angle height 2 atomic Signatures was developed. The construction of the descriptor matrix resulted in a matrix with 45 rows and 249 columns, one column for the corresponding contact angles and 248 for the unique height 2 atomic Signatures. In order to perform LOOCV, 193 atomic Signatures were removed leaving 55 atomic Signatures with occurence numbers equal to or greater than 3 for the QSAR analysis. The forward stepping MLR resulted in Figure 5.3, which illustrates the R^2 and q^2 as function of the number of atomic Signatures.

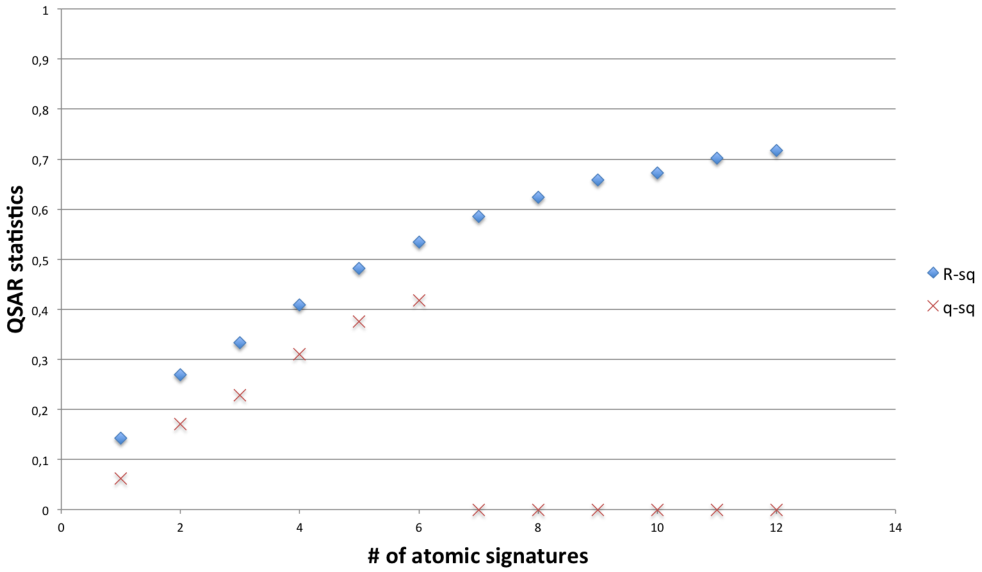

Figure 5.3: The impact of contact angle height 2 atomic Signatures on the QSAR statistics, which is plotted as function of the number of atomic Signatures.

Here the same tendencies are present as for the contact angle height 1 atomic Signatures. This analysis resulted in a QSAR equation with 6 atomic Signatures, which are depicted in Table 5.4.

Table 5.4: The 6 unique height 2 atomic Signatures used in the QSAR analysis of the contact angle. The Signatures are depicted in the order from most significiant to least.

Variable	atomic Signature
x_{198}	[H]([O]([C]))
x_{32}	[B]([C]([C][H][H])=[O])
x_3	[B]([B]([C][H])[H][H])
x_{160}	[F]([B]([C][F]))
x_{179}	[H]([C]([B][H][H]))
x_{183}	[H]([C]([C][C][H]))

Using the 6 atomic Signatures resulted in the QSAR equation, equation 5.3, and by predicting the contact angles of the polymers in the training set and plotting these values against the experimental values, resulted in Figure 5.4. Notice that the use of equation 5.3 will result in normalized contact angles in the range of -1 to 1, these values have been obtained by normalizing the contact angles before performing the QSAR analysis using equation 5.2. This was done due to reasons, which will be detailed in section 6.1.1. The equation used to normalize the contact angles is depicted in Figure A.1 in appendix A.

$$\theta_{norm} = 2 \cdot \frac{\theta - \theta_{min}}{\theta_{max} - \theta_{min}} - 1 \tag{5.2}$$

$$\theta_{norm} = 0.074 - 0.370 \cdot x_{198} - 0.580 \cdot x_{32} + 0.530 \cdot x_3 + 0.239 \cdot x_{160} + 0.115 \cdot x_{179} + 0.012 \cdot x_{183} \tag{5.3}$$

As seen on the two figures, this resulted model obtained a R^2 and q^2 value of 0.53 and 0.42, respectively.

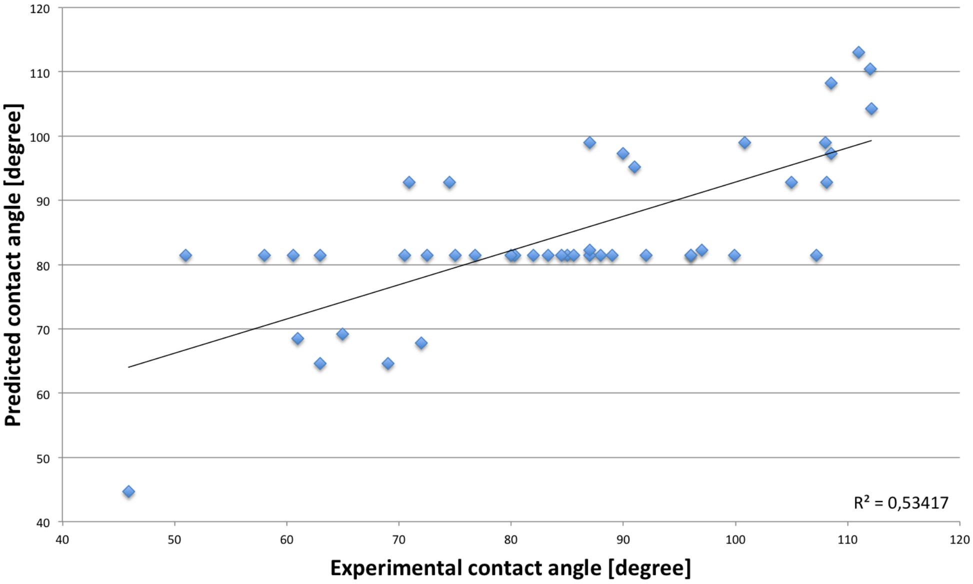

Figure 5.4: The experimental- versus predicted values for the QSAR equation based on the contact angle training set using height 2 atomic Signatures.

Critcal surface tension

The two QSAR models based on the training set with CST were normalized using the trend linw in Figure A.2 of appendix A.

The first QSAR model was based on the height 1 atomic Signatures, which are presented in Table 5.3. The model was calculated on a descriptor matrix with 39 rows and 74 columns, one column for the CST and 73 columns for the unique height 1 atomic Signatures. Prior to performing the forward stepping MLR 40 unique atomic Signatures were removed leaving 33 with occurrence numbers greater than or equal to 3 for the LOOCV analysis. Figure 5.5 illustrates the R^2 and q^2 values as function of the number of atomic Signatures.

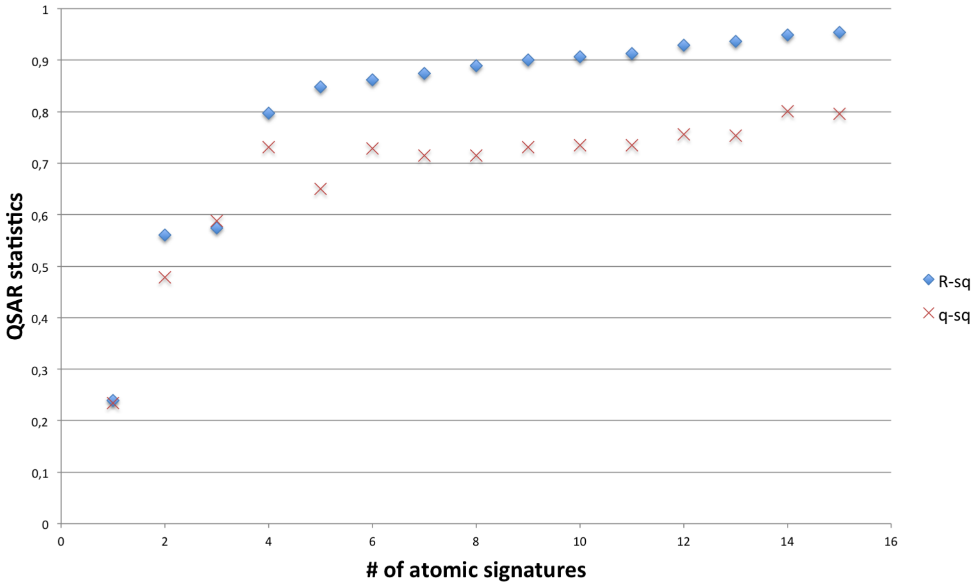

Figure 5.5: The impact of CST height 1 atomic Signatures on the QSAR statistics, which is plotted as function of the number of atomic Signatures.

As the figure illustrates the R^2 and q^2 increased as a function of the independent variables. The calculations were terminated at 15 atomic signatures due to the F-statistics, thus the 16^{th} atomic Signature was insignificant. The QSAR equation was chosen on the basis of the best predicting model, i.e. highest q^2 value. A QSAR equation, equation 5.4, with 14 atomic Signatures was hereby obtained with a R^2 and q^2 value of 0.95 and 0.80, respectively. The 14 atomic Signatures included in the QSAR equation are marked with bold in Table 5.3.

$$\begin{aligned} \mathrm{CST}_{norm} = 0.311 &- 0.069 \cdot x_{52} - 0.234 \cdot x_{23} - 0.057 \cdot x_{54} - 0.046 \cdot x_{30} - 0.152 \cdot x_{53} \\ &- 0.421 \cdot x_{7} + 0.448 \cdot x_{20} + 0.021 \cdot x_{34} + 0.148 \cdot x_{50} - 0.135 \cdot x_{14} \\ &- 0.404 \cdot x_{37} + 0.253 \cdot x_{69} + 0.210 \cdot x_{42} - 0.216 \cdot x_{47} \end{aligned} \tag{5.4}$$

Using this QSAR equation to predict the CST of polymers in the training set and plotting these values against the experimental values resulted in Figure 5.6, which confirms the R^2 value of 0.95.

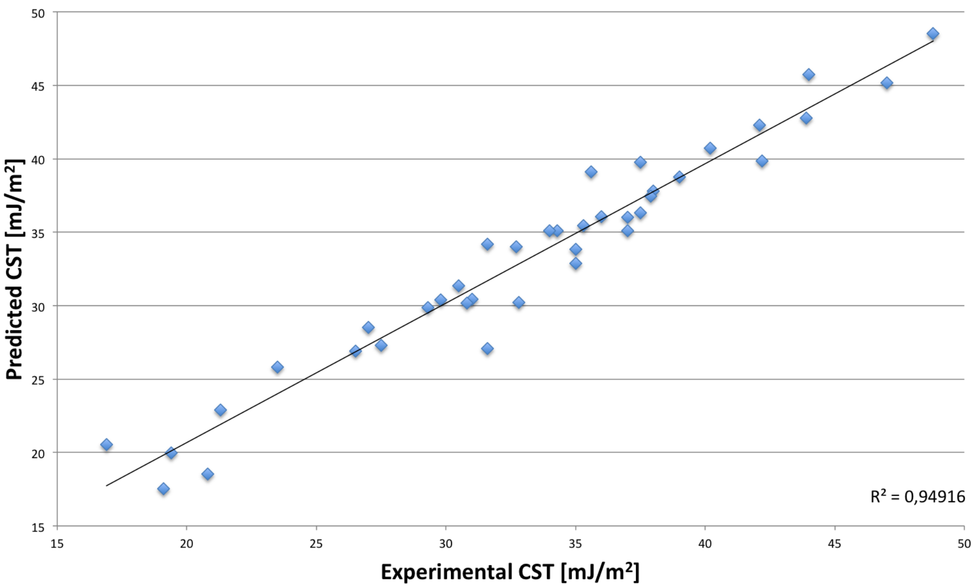

Figure 5.6: The experimental- versus predicted values for the QSAR equation based on the CST training set with 14 height 1 atomic Signatures.

The last QSAR equation was constructed by translating the CST training set into height 2 atomic Signatures. The resulting descriptor matrix contained 39 rows and 184 columns, one column for the CST and 183 columns for the unique height 2 atomic Signatures. The removal of atomic Signatures, which had occurrence numbers below 3 resulted in a descriptor matrix with 50 unique atomic Signatures. The forward stepping MLR and LOOCV resulted in Figure 5.7.

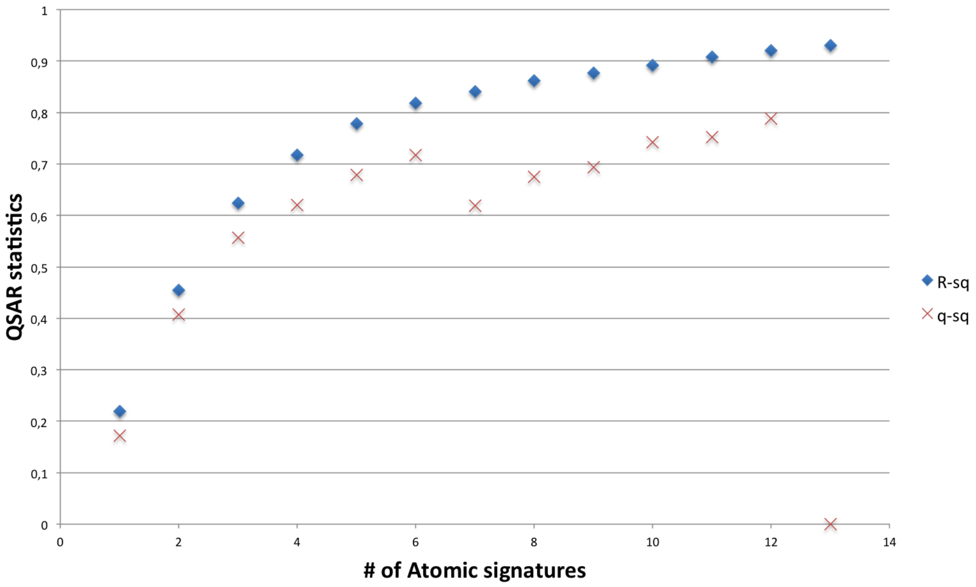

Figure 5.7: The impact of CST height 2 atomic Signatures on the QSAR statistics, which is plotted as function of the number of independent variables.

As the figure illustrates the most predictive and correlative model occurs with 12 atomic Signatures. This model obtained R^2 and q^2 values of 0.92 and 0.79, respectively. The 12 atomic Signatures included in the QSAR equation, equation 5.5, are illustrated in Table 5.5.

Table 5.5: The 12 unique height 2 atomic Signatures used in the QSAR analysis of the CST. The Signatures are depicted in the order from most significiant to least.

Variable	atomic Signature
x_{122}	[F]([C]([B][F][F]))
x_{62}	[C]([C]([C][H][H])[H][H][O]([C]))
x_{117}	[F]([B]([B][F]))
x_{126}	[H]([B]([B][H]))
x_{128}	[H]([B]([C][H]))
x_{133}	[H]([C]([B][H][H]))
x_{71}	[C]([C]([H][H][H])=[O][O]([C]))
x_{36}	[Br]([C](p[C]p[C]))
x_{18}	[B]([B]([H][H])[C]([O]=[O])[C]([H][H][H]))
x_{162}	[O](=[B]([C]))
x_{59}	[C]([C]([C][H][H])[C]([C][H][H])[H][H])
x_{142}	[H]([C]([C][H][O]))

$$\begin{aligned}\mathrm{CST}_{norm} = 0.237 &- 0.312\cdot x_{122} - 0.340\cdot x_{62} - 0.232\cdot x_{117} - 0.030\cdot x_{126} - 0.102\cdot x_{128} \\ &- 0.097\cdot x_{133} + 0.305\cdot x_{71} + 0.390\cdot x_{36} + 0.310\cdot x_{18} + 0.370\cdot x_{162} \\ &- 0.040\cdot x_{59} - 0.088\cdot x_{142}\end{aligned} \tag{5.5}$$

Using this QSAR equation to predict the CST of polymers in the training set and plotting these values against the experimental values resulted in Figure 5.8.

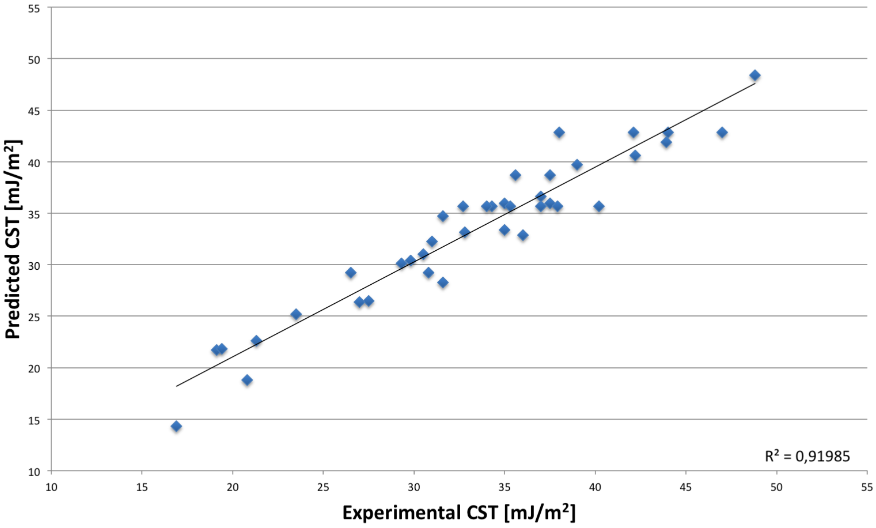

Figure 5.8: The experimental- versus predicted values for the QSAR equation based on the CST with 12 height 2 atomic Signatures.

5.1.3 The constraint equations

As described in section 5.1, 4 QSAR models would be developed and the best performing model would be selected for further development. The model with the highest correlative and predictive abilities was the QSAR model based on CST height 1 atomic Signature. This section will describe the construction of the constraint equations for this model.

The following constraint equations are written in the order of least iterations to most, thus in the order they were solved. Equation 5.6-5.32 are the consistency equations, which ensures the alignment of atoms in the construction of molecular Signatures and has taken the form of either equation 2.9 or 2.10 depending on the bond type. Equation 5.33 is the graphicality equation which ensures that the valence of each atom is meet and has taken the form of equation 2.8. Equation 5.34 is the PRU equation, which ensures that only two repeating atoms are present in solved molecular Signatures.

The last constraint equation is the QSAR equation, equation 5.35, which is used to rank the solved molecular Signatures. The purpose of the i-QSAR model was to predict polymers with improved hydrophobicity, i.e. superhydrophobic materials, and therefore only solutions with CST values lower than the polymers in the training set, 16.9 mJ/m^2, was solved. The interval was set to -1.001 to -1.000 due to the computational time, which corresponded to an un-normalized interval of 16.884-16.900 mJ/m^2.

$$\text{C=C: } x_{17} \equiv 0 mod 2 \tag{5.6}$$

$$\text{B=O: } -x_{11} + x_{64} = 0 \tag{5.7}$$

$$\text{B-I: } -x_{15} + x_{60} = 0 \tag{5.8}$$

$$\text{C-Br: } -x_{16} + x_{27} = 0 \tag{5.9}$$

$$\text{C-Cl: } -x_{33} + x_{51} = 0 \tag{5.10}$$

$$\text{C-Se: } -x_{38} + x_{73} = 0 \tag{5.11}$$

$$\text{H-Se: } -x_{59} + x_{73} = 0 \tag{5.12}$$

$$\text{C-P: } -x_{48} + x_{71} = 0 \tag{5.13}$$

$$\text{H-P: } -x_{58} + 2 \cdot x_{71} = 0 \tag{5.14}$$

$$\text{C-S: } -x_{49} + 2 \cdot x_{72} = 0 \tag{5.15}$$

$$\text{O=S: } -x_{66} + 2 \cdot x_{72} = 0 \tag{5.16}$$

$$\text{B-O-: } -x_{10} + x_{67} + x_{68} = 0 \tag{5.17}$$

$$\text{H-O: } -x_{57} + x_{68} + x_{70} = 0 \tag{5.18}$$

$$\text{H-N: } -x_{56} + x_{62} + 2 \cdot x_{63} = 0 \tag{5.19}$$

$$\text{C-N: } -x_{24} - x_{36} - x_{40} + 2 \cdot x_{62} + x_{63} = 0 \tag{5.20}$$

$$\text{B-Cl: } -2 \cdot x_{4} - x_{5} - x_{6} + x_{50} = 0 \tag{5.21}$$

$$\text{C-F: } -2 \cdot x_{19} - 3 \cdot x_{22} + x_{53} = 0 \tag{5.22}$$

$$\text{C=O: } -x_{18} - x_{24} - x_{25} - x_{40} - x_{41} - x_{44} + x_{65} = 0 \tag{5.23}$$

$$\text{C-I: } -x_{21} - x_{31} - x_{35} - x_{39} - x_{44} - x_{46} + x_{61} = 0 \tag{5.24}$$

$$\text{B-B: } x_1 + x_2 + x_3 + x_4 + x_5 + x_6 + x_7 + x_8 + x_9 + x_{10} \equiv 0 mod 2 \tag{5.25}$$

$$\text{B-H: } -x_3 - x_6 - x_8 - 2 \cdot x_9 - x_{10} - 2 \cdot x_{14} - 2 \cdot x_{15} + x_{54} = 0 \tag{5.26}$$

$$\text{B-F: } -x_2-x_5-2\cdot x_7-x_8-x_{12}-2\cdot x_{13}+x_{52}=0 \tag{5.27}$$

$$\begin{aligned}\text{B-C: } & -2\cdot x_1-x_2-x_3-x_{11}-2\cdot x_{12}-x_{13}-x_{14}+x_{17}+x_{18}+x_{19}+x_{20}\\ & +x_{21}+x_{22}+x_{23}+x_{24}+x_{25}+x_{26}=0\end{aligned} \tag{5.28}$$

$$\text{C-pC: } 2\cdot x_{26}+2\cdot x_{27}+2\cdot x_{42}+2\cdot x_{45}+2\cdot x_{46}+2\cdot x_{47}+2\cdot x_{48}+2\cdot x_{49}\equiv 0 mod 2 \tag{5.29}$$

$$\text{C-O-: } -x_{25}-x_{32}-x_{37}-x_{39}-x_{41}-x_{43}-x_{44}-x_{47}+x_{67}+2\cdot x_{69}+x_{70}=0 \tag{5.30}$$

$$\begin{aligned}\text{C-C: } & x_{18}+x_{19}+x_{20}+x_{21}+4\cdot x_{28}+3\cdot x_{29}+2\cdot x_{30}+2\cdot x_{31}+2\cdot x_{32}+x_{33}\\ & +x_{34}+x_{35}+x_{36}+x_{37}+x_{38}+x_{39}+x_{40}+x_{41}+x_{42}\equiv 0 mod 2\end{aligned} \tag{5.31}$$

$$\begin{aligned}\text{C-H: } & -x_{17}-2\cdot x_{20}-x_{21}-3\cdot x_{23}-x_{29}-2\cdot x_{30}-x_{31}-x_{32}-2\cdot x_{33}\\ & -3\cdot x_{34}-2\cdot x_{35}-2\cdot x_{36}-2\cdot x_{37}-2\cdot x_{38}-x_{39}-x_{43}-x_{45}+x_{55}=0\end{aligned} \tag{5.32}$$

$$\begin{aligned}\text{Graph eq.: } & x_1+x_2+x_3+x_4+x_5+x_6+x_7+x_8+x_9+x_{10}+x_{12}+x_{13}+x_{14}+x_{15}\\ & -x_{16}+x_{17}+x_{18}+2\cdot x_{19}+2\cdot x_{20}+2\cdot x_{21}+2\cdot x_{22}+2\cdot x_{23}+x_{24}+x_{25}\\ & +x_{26}+x_{27}+2\cdot x_{28}+2\cdot x_{29}+2\cdot x_{30}+2\cdot x_{31}+2\cdot x_{32}+2\cdot x_{33}+2\cdot x_{34}\\ & +2\cdot x_{35}+2\cdot x_{36}+2\cdot x_{37}+2\cdot x_{38}+2\cdot x_{39}+x_{40}+x_{41}+x_{42}+2\cdot x_{43}\\ & +x_{44}+x_{45}+x_{46}+x_{47}+x_{48}+x_{49}-x_{50}-x_{51}-x_{52}-x_{53}-x_{54}-x_{55}\\ & -x_{56}-x_{57}-x_{58}-x_{59}-x_{60}-x_{61}+x_{62}+x_{63}-x_{64}-x_{65}-x_{66}+x_{71}\\ & +2\cdot x_{72}\equiv 0 mod 2\end{aligned} \tag{5.33}$$

$$\begin{aligned}\text{PRU eq.: } & x_1+x_2+x_3+x_4+x_5+x_6+x_7+x_8+x_9+x_{10}+x_{11}+x_{12}+x_{13}+x_{14}+x_{15}\\ & +x_{16}+x_{60}+x_{61}+x_{71}+x_{73}=2\end{aligned} \tag{5.34}$$

$$\begin{aligned}\text{CST}_{norm} = & \, 0.311-0.069\cdot x_{52}-0.234\cdot x_{23}-0.057\cdot x_{54}-0.046\cdot x_{30}-0.152\cdot x_{53}\\ & -0.421\cdot x_7+0.448\cdot x_{20}+0.021\cdot x_{34}+0.148\cdot x_{50}-0.135\cdot x_{14}\\ & -0.404\cdot x_{37}+0.253\cdot x_{69}+0.210\cdot x_{42}-0.216\cdot x_{47}\end{aligned} \tag{5.35}$$

The equations were solved using the brute force method developed by Weis and Visco (2010) [15], which has been exemplified in section 2.2.6. The equations have therefore been solved using the min/max occurrence numbers of the atomic Signatures, which are illustrated in the tab "CST h1" of the document "Descriptor matrices.xlsx" on the enclosed CD.
Solving the 28 constraint equations and only accepting molecular Signatures with CST values in the range of 16.844-16.900 mJ/m^2 resulted in 2035 new molecular Signatures. An example of one of these is depicted in Table 5.6, note that only atomic Signatures with values greater than 0 are depicted in the table. The 2035 molecular Signatures are illustrated in the file "CST-solved-molecular-sig.xlsx" on the enclosed CD.

Table 5.6: Example of a solved molecular Signature, note that only atomic Signatures with occurence numbers greater than 0 are depicted.

Molecular Signature	x_{12}	x_{13}	x_{23}	x_{26}	x_{30}	x_{34}	x_{42}	x_{47}	x_{55}	x_{69}
no. 1	1	1	2	1	15	1	1	2	39	1

5.1.4 Structure generation

The last step in the i-QSAR analysis was the translation from molecular Signatures into 2D molecular Structures. This was done by using an algorithm developed by Faulon et al. (2003) [20] and and has been exemplified in section 2.2.6. The translation resulted in 456 2D molecular structures and most of which had similar tendencies. Due to the sheer size of the solutions only a selection of these describing general trends are illustrated in Figure 5.9, Figure 5.10 and Figure 5.11.

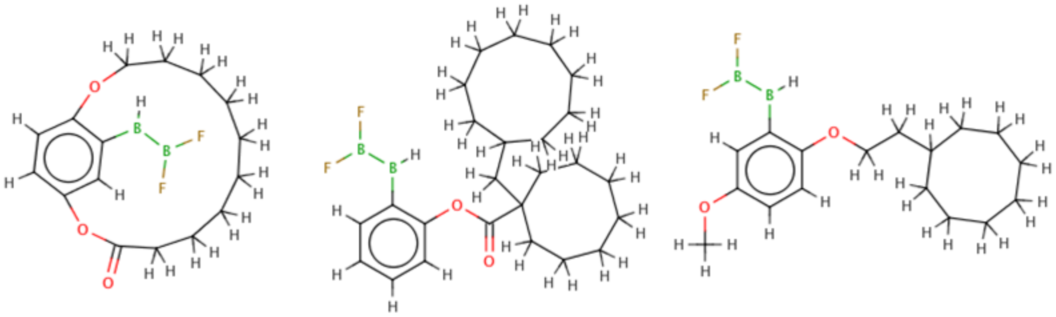

Figure 5.9: The first selection of solutions to the i-QSAR model. Note that these structures are repeating units of polymers and that the *boron* atoms represents repeating *carbon* atoms of the backbone, cf. Table 5.1.

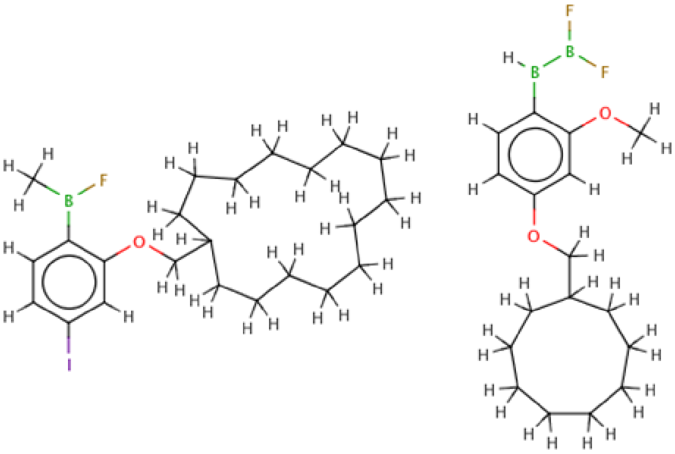

Figure 5.10: The second selection of solutions to the i-QSAR model. Note that these structures are repeating units of polymers and that the *boron* and *iodide* atoms represents repeating *carbon* and *oxygen* atoms of the backbone respectively, cf. Table 5.1.

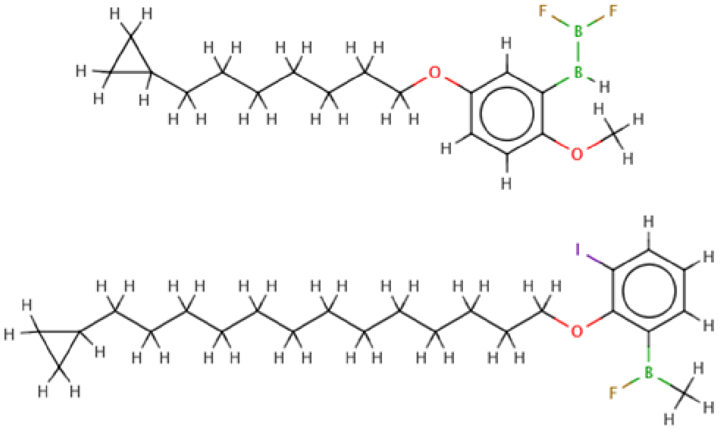

Figure 5.11: The third selection of solutions to the i-QSAR model. Note that these structures are repeating units of polymers and that the *boron* and *iodide* atoms represents repeating *carbon* and *oxygen* atoms of the backbone respectively, cf. Table 5.1.

5.1.5 Subjective evaluation

The solutions to the i-QSAR models were then subjective evaluated on internal strain, solubility, adhesion with water, availability and cost. This resulted in the purchase of poly(styrene-co-α-methylstyrene).

5.2 Vertification of inverse-quantitative structure-activity relationship

The translation of PSMS into height 1 atomic Signatures resulted in 10 atomic Signatures. Two of these were not included in the CST model and are therefore denoted as "-" in Table 5.7.

Table 5.7: Illustrates the molecular siganture of PSMS. The atomic Signature of height 1 and occ# is short for the occurrence number of the respective atomic Signatures.

Variable	atomic Signature	Occ#
$\mathbf{x_{14}}$	**[B]([C][H][H])**	**1**
$\mathbf{x_{20}}$	**[C]([B][C][H][H])**	**1**
$\mathbf{x_{23}}$	**[C]([B][H][H][H])**	**1**
x_{26}	[C]([B]p[C]p[C])	1
$\mathbf{x_{42}}$	**[C]([C]p[C]p[C])**	**1**
x_{45}	[C](p[C]p[C][H])	10
$\mathbf{x_{54}}$	**[H]([B])**	**2**
x_{55}	[H]([C])	16
-	[C]([B][C][C][H])	1
-	[B]([C][C][C])	1

Five of the atomic Signatures were incorporated in the QSAR equation, which are marked with bold in the table. The occurrence numbers of the five atomic Signatures are also depicted in the table and were used to calculate the CST of PSMS, as illustrated in equation 5.36 and 5.37. The unnormalized CST value was obtained using the trend line of Figure A.2 in appendix A resulting in a CST of 40.60 mJ/m^2, as depicted in equation 5.38.

$$\mathrm{CST}_{norm} = 0.311 - 0.234 \cdot x_{23} - 0.057 \cdot x_{54} + 0.448 \cdot x_{20} - 0.135 \cdot x_{14} + 0.210 \cdot x_{42} \tag{5.36}$$

$$\mathrm{CST}_{norm} = 0.311 - 0.234 \cdot 1 - 0.057 \cdot 2 + 0.448 \cdot 1 - 0.135 \cdot 1 + 0.210 \cdot 1 = 0.486 \tag{5.37}$$

$$\mathrm{CST}_{i-QSAR} = 15.95 \cdot 0.486 + 32.85 = 40.60 \text{ mJ/m}^2 \tag{5.38}$$

Next, the CST of PSMS was experimentally determined, as described in section 4.3. The measured contact angles using the different volumetric ratios of formamide and 2-ethoxyethanol on a flat PSMS surface are illustrated in Table 5.8.The water contact angle was also measured.

Table 5.8: Illustrates the contact angle, θ, for each of the listed solvents on a flat PSMS surface. Note that ^{1} is the water *contact angle* of the PSMS, which also was measured.

Formamide/2-ethoxyethanol [V/V %]	γ_{lv} [mJ/m^2]
1.00/0.00	71.36±1.21
0.99/0.01	68.38±0.86
0.75/0.25	55.07±0.15
0.49/0.51	46.52±2.58
0.34/0.66	41.25±2.54
0.19/0.81	33.12±3.20
0.03/0.97	Spreads
Water	94.10±3.73^1

Figure 5.12 illustrates the Zisman plo, which resulted in a experimental CST of 22.78 mJ/m^2 as illustrated in equation 5.39.

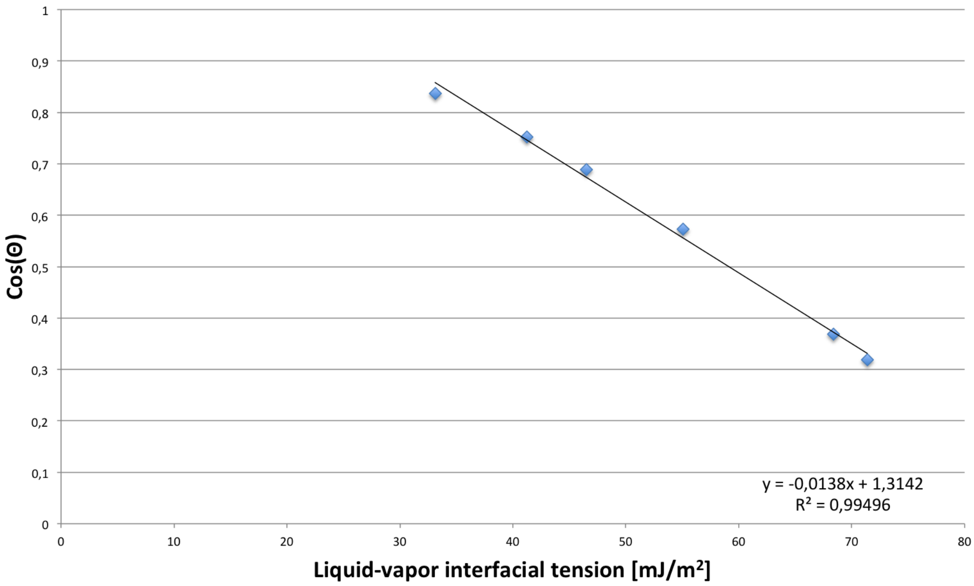

Figure 5.12: Illustrates the Zisman plot of PSMS using different ratios of Formamide and 2-ethoxyethanol.

$$\text{CST}_{exp} = \frac{1-1.3142}{-0.0138} = 22.78\ \text{mJ/m}^2 \tag{5.39}$$

5.3 Electrospinning of poly(styrene-co-α-methylstyrene)

The electrospinning conditions of PSMS was investigated followed by the analysis of the hydrophobicity.

5.3.1 The investigation of the electrospinning ability of poly(styrene-co-α-methylstyrene)

The electrospinning ability of PSMS was investigated by dissolving the polymer in cyclohexane, 90/10 w/w % cyclohexane/THF and DMF with concentrations of 25, 35 and 50 w/w % . These samples were only investigated by observing the polymer jet and the deposited material in microscope, as described in section 4.5.1. These results were therefore only characterized as either producing beads, i.e. electrospraying, fibers, i.e. electrospinning, or as an intermediate between the two processes. The results from these experiments are depicted in Table 5.9, where the deposited material has been characterized as either beads "B" or an intermediate between beads and fibers "I". Note that in total 108 experiments were conducted but only 63 abbriviations are depcited in the table. This is because each of the flow rates were investigated for each of the 2 gap distances and the 2 different voltages. To illustrate this, all combinations of the 35 w/w % PSMS/DMF resulted in beads while samples of 50 w/w % PSMS/DMF for a flow rate of 1 mL/hr resulted in intermediates. Samples with flow rates of 5 and 10 mL/hr on the other hand resulted in beads.

Table 5.9: The 108 samples electrospun by varying the polymer concentration, solvent, flow rate, gap distance and voltage. "B" indicates the formation of beads, "I" indicates an intermediate between beads and fibers.

		Flow rate mL/hr]			Gap distance [cm]		Voltage [kV]	
[PSMS]	Solvent	1	5	10	15	20	20	30
25	Cyclohexane	B	B	B	B	B	B	B
35	Cyclohexane	B	B	B	B	B	B	B
50	Cyclohexane	B	B	B	B	B	B	B
25	90/10 w/w % Cyclohexane/THF	B	B	B	B	B	B	B
35	90/10 w/w % Cyclohexane/THF	B	B	B	B	B	B	B
50	90/10 w/w % Cyclohexane/THF	B	B	B	B	B	B	B
25	DMF	B	B	B	B	B	B	B
35	DMF	B	B	B	B	B	B	B
50	DMF	I	B	B	I	I	I	I

Based on the results from Table 5.9, a new set of experiments was conducted in order to more thoroughly investigate the formation and dimension of the electrospun PSMS fibers. This was done by electrospinning 15, 25, 35, 50, 52, 54, 56, 58 and 60 w/w % PSMS/DMF using the 3 groups of conditions depicted in Table 4.5. In Figure 5.13, SEM pictures are depicted for each of the 9 concentration electrospun for the group 2 conditions. As seen on the figure, beads were formed until the concentration reached 52 w/w % PSMS/DMF, where an intermediate between beads and fibers was present and when the concentration was increased to 54 w/w %

PSMS/DMF, fibers were formed. This tendency was also true for the group 1 and 2 conditions with the exception that fiber formation started at 52 w/w % PSMS/DMF.

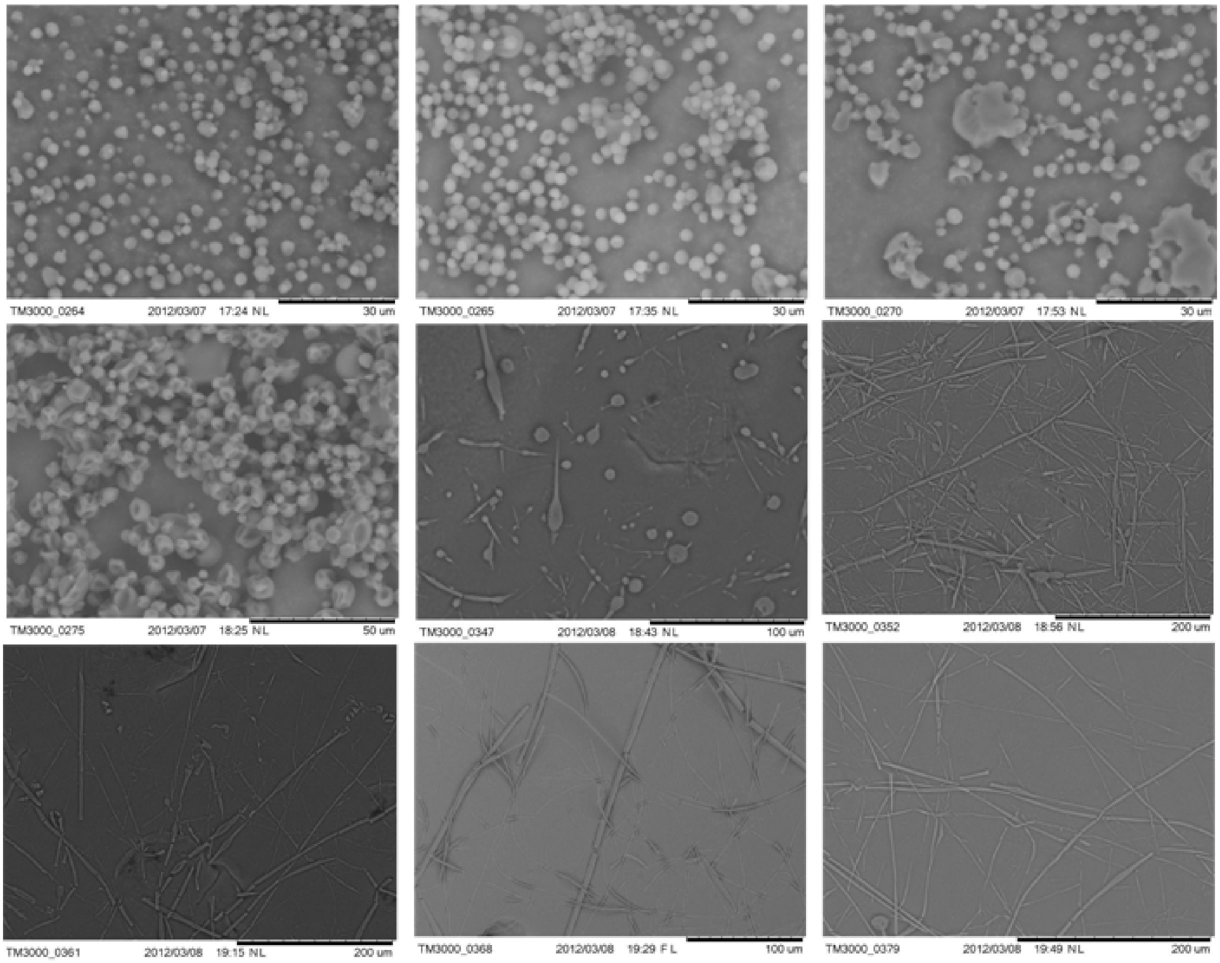

Figure 5.13: The 9 different PSMS concentrations electrospun by the group 2 conditions. Top row from the left: 15, 25 and 35 w/w % PSMS/DMF. Middle row from the left: 50, 52 and 54 w/w % PSMS/DMF. Bottom row from the left: 56, 58 and 60 w/w % PSMS/DMF.

Fiber size distributions were then determined by analyzing the SEM pictures using the length weighted fiber diameter method, which utilize the Length weighted log-normal distribution, which is illustrated as equation 5.40-5.42.

$$\ln(\mathrm{x}_{mean}) = \frac{1}{L_{tot}} \sum L_i \cdot x_i \tag{5.40}$$

$$\ln(\sigma_g) = \sqrt{\frac{\sum(L_i(x_i - x_{mean}^2)}{L_{tot}}} \tag{5.41}$$

$$\mathrm{f(x)} = \frac{1}{x_i \cdot ln(\sigma_g) \cdot \sqrt{2\pi}} \cdot exp\left(-\frac{ln(x_i - x_{mean})^2}{2\sigma_g^2}\right) \tag{5.42}$$

This resulted in the determination of the fiber size distributions for the following samples:

- Group 1: 52-60 w/w % PSMS/DMF
- Group 2: 52-60 w/w % PSMS/DMF
- Group 3: 54-60 w/w % PSMS/DMF

This yielded in a total of 14 samples and their fiber size distributions are depicted in Figure 5.14, Figure 5.15 and Figure 5.16.

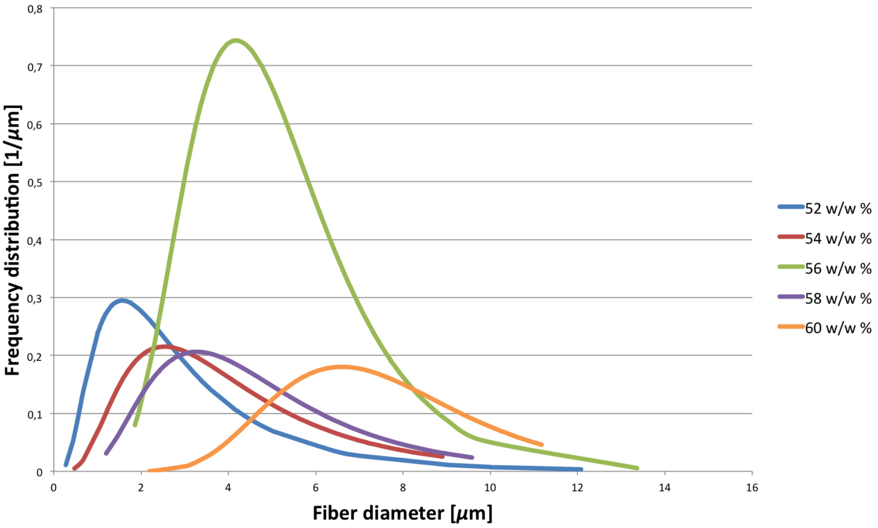

Figure 5.14: Length weighted log-normal frequency distributions of the fibers electrospun by group 1 conditions.

Fibers electrospun from group 1 conditions hereby obtained a mean fiber size of 1.57, 2.55, 4.16, 3.31 and 6.57 μm for 52, 54, 56, 58 and 60 w/w % PSMS/DMF, respectively.

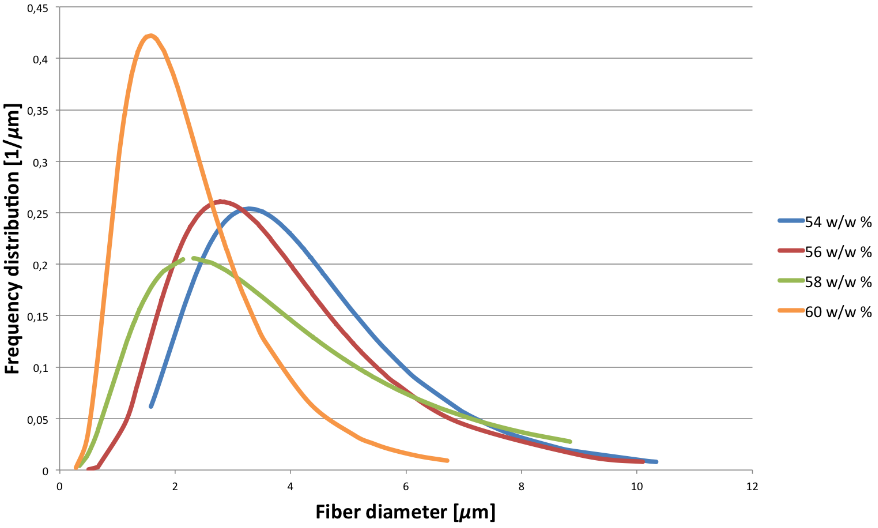

Figure 5.15: Length weighted log-normal frequency distributions of the fibers electrospun by group 2 conditions.

Fibers electrospun from group 2 conditions hereby obtained a mean fiber size of 3.30, 2.78, 2.32 and 1.58 μm for 54, 56, 58 and 60 w/w % PSMS/DMF, respectively.

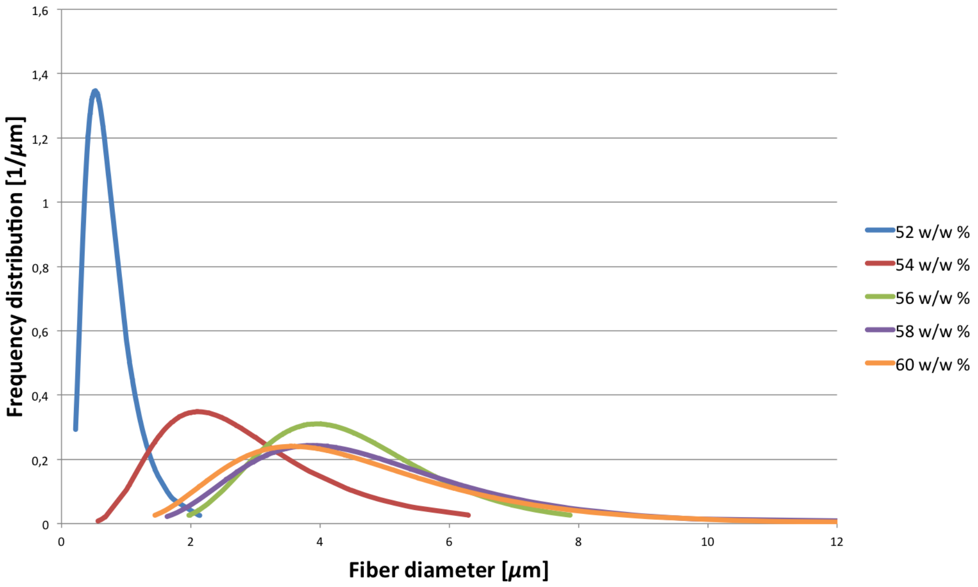

Figure 5.16: Length weighted log-normal frequency distributions of the fibers electrospun by group 3 conditions.

Fibers electrospun from group 3 conditions hereby obtained a mean fiber size of 0.52, 2.11, 3.94, 3.88 and 3.56 μm for 52, 54, 56, 58 and 60 w/w % PSMS/DMF. As seen on the 3 graphs, the mean fiber size increases as a function of the concentration for samples electrospun by the group 1 and 3 conditions while it decreases for the group 3 conditions. The mean fiber size is depicted as a function of the PSMS concentration in Figure 5.17.

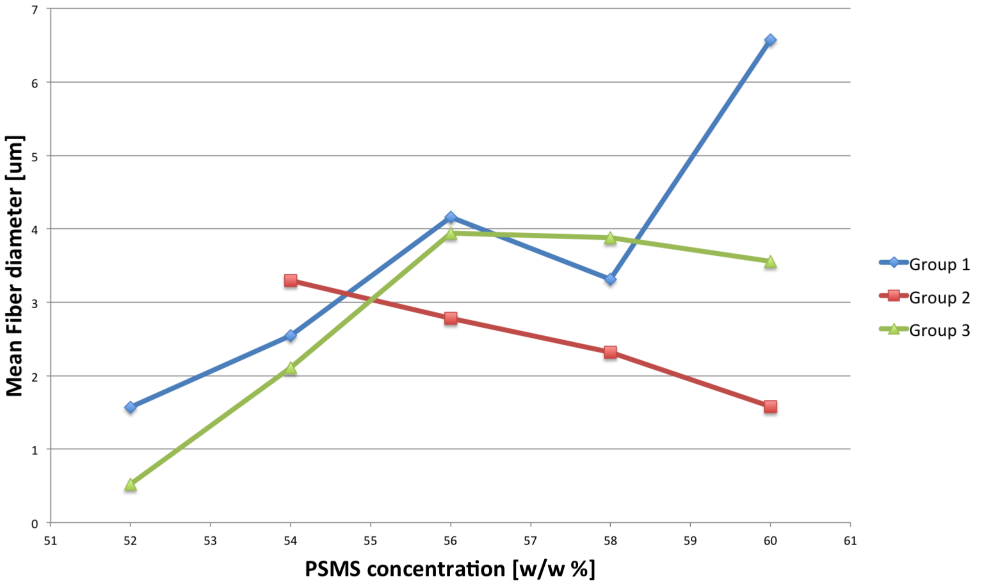

Figure 5.17: The mean fiber diameter as function of the electrospun PSMS concentration.

5.3.2 The hydrophobicity of electrospun poly(styrene-co-α-methylstyrene)

The production of electrospun membranes onto glass slides resulted in 48 fiber mats, which were investigated by measuring water contact angle. Samples electrospun using the group 1 conditions are depicted in Figure 5.18, the group 2 conditions in Figure 5.19 and the group 3 conditions in Figure 5.20. Notice that pictures used to measure the contact angles are illustrated in Figure 5.19 for the 10 g/m^2 series.

The general tendency for the 3 groups of electrospun fiber mats was that the hydrophobicity decreased as a function of mean fiber size until increasing for the highest fiber size and that the hydrophobicity generally decreased as function of deposited fibers, i.e. fiber mat thickness. The hydrophobicity of the produced fiber mats can all be characterized as being hydrophobic, since they all possed a contact angle greater than 90^o. The fiber mats produced, in Figure 5.18, with 10 and 20 g PSMS/m^2 are superhydrophobic while only the samples with a mean fiber diameter of 6.57 μm for the 30 and 40 g PSMS/m^2 samples can be classified as being superhydrophobic.

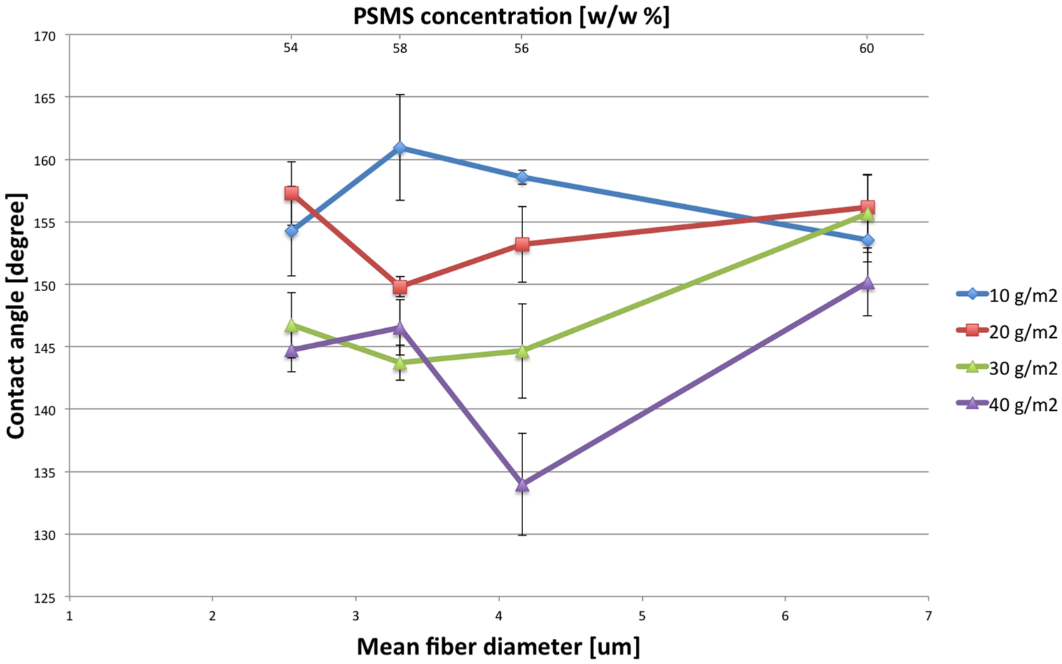

Figure 5.18: The contact angle of samples electrospun using the group 1 conditions as a function of both the mean fiber diameter and the PSMS concentration.

The hydrophobicity of the electrospun fiber mats in Figure 5.19 with 10 and 20 g PSMS/m^2 all exhibited superhydrophobic properties while the sample containing a mean fiber diameter of 2.32 μm for the 20 g PSMS/m^2 together will all samples of the 40 g PSMS/m^2 fiber mats could be classified as being hydrophobic.

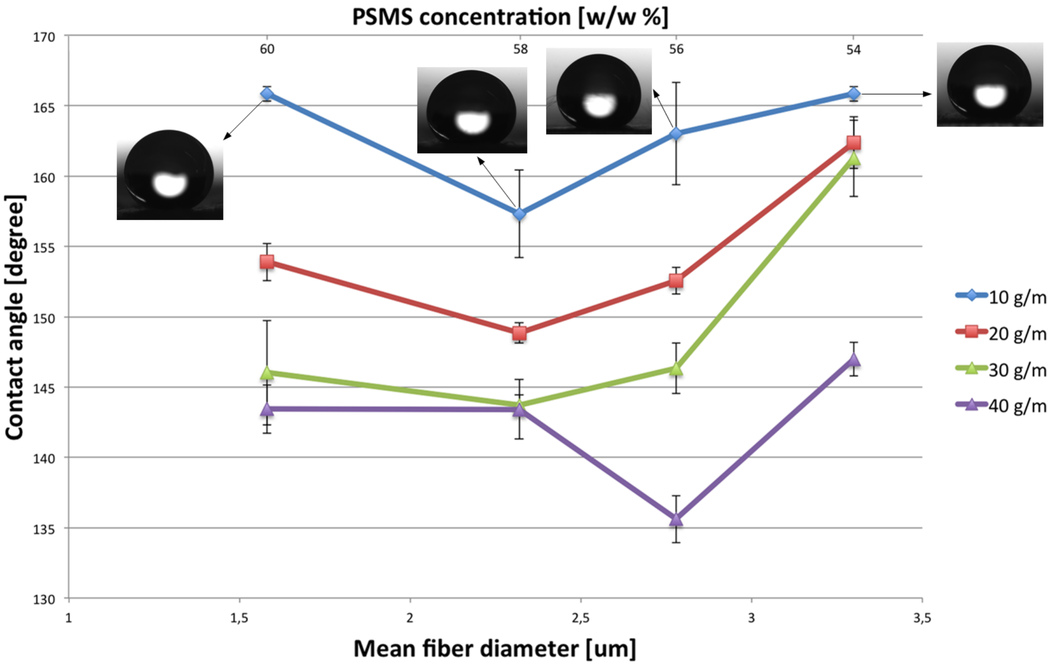

Figure 5.19: The contact angle of samples electrospun using the group 2 conditions as a function of both the mean fiber diameter and the PSMS concentration. Notice that the concentration is depicted from 60 to 50 w/w % PSMS/DMF.

The fiber mats electrospun using the group 3 electrospinning conditions are illustrated in Figure 5.20. These samples exhibited the same tendencies as described in the above, thus the fiber mats of 10 and 20 g PSMS/m^2 exhibits superhydrophobicity while only selected fiber mats of the 30 g PSMS/m^2 series exhibits the same characteristics. Samples of the 40 g PSMS/m^2 series can be classified as being hydrophobic.

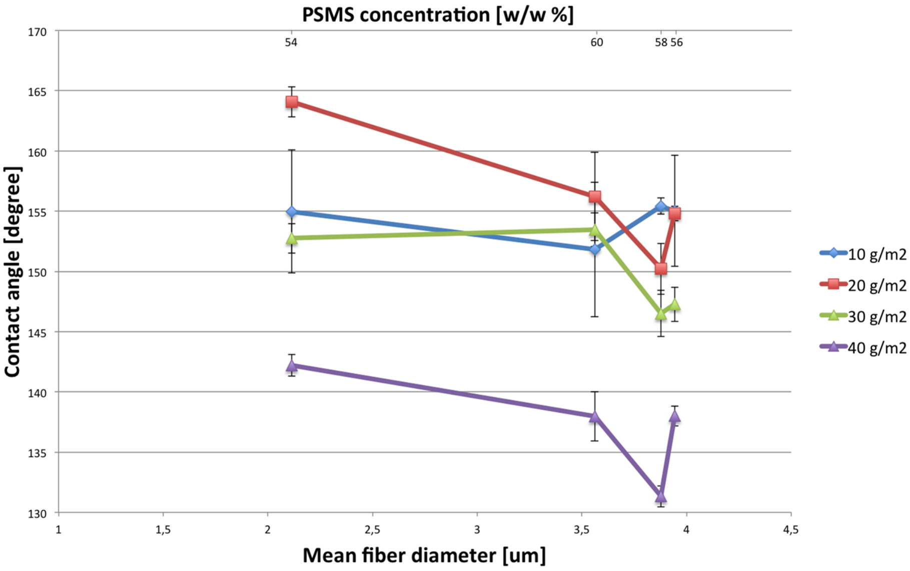

Figure 5.20: The contact angle of samples electrospun using the group 3 conditions as a function of both the mean fiber diameter and the PSMS concentration. Notice that the concentration is depicted in the order of 54, 60, 58 and 56 w/w % PSMS.

5.4 Membrane manufacturing and characterization

Table 5.10 illustrates the actual amount of deposited fiber, the concentration used to electrospin the membrane, the mean fiber size from Figure 5.17, the contact angle from Figure 5.18 and Figure 5.19, the apparent Darcy flow resistance and the porosity for each of the types of membranes manufactured.

Table 5.10: The membrane datasheet describing the template glass fiber and the 6 different types of membranes fabricated. [PSMS] is the PSMS concentration given in w/w % PSMS/DMF, θ is the contact angle and d_f is the mean fiber diameter given from Figure 5.17.

Membrane	Weight [g]	[PSMS]	d_f [μm]	θ [degree]	R_D [m^{-1}]	Porosity [-]
Glass fiber	-	-	6.50	-	$2.15 \cdot 10^6 \pm 1.10 \cdot 10^5$	0.99
A_{10}	9.86±0.58	54	1.58	165.85±0.51	$2.38 \cdot 10^6 \pm 2.25 \cdot 10^5$	0.99
A_{20}	21.90±2.71	54	1.58	162.39±1.84	$3.13 \cdot 10^6 \pm 3.40 \cdot 10^5$	0.99
A_{30}	29.14±1.19	54	1.58	161.28±1.78	$3.47 \cdot 10^6 \pm 1.80 \cdot 10^5$	0.99
A_{40}	42.72±13.23	54	1.58	147.00±1.20	$3.56 \cdot 10^6 \pm 4.66 \cdot 10^5$	0.99
B_{30}	30.29±1.09	60	6.57	155.64±3.11	$3.85 \cdot 10^6 \pm 1.09 \cdot 10^6$	0.99
B_{40}	44.72±5.90	60	6.57	150.19±2.73	$5.10 \cdot 10^6 \pm 4.64 \cdot 10^6$	0.99

Figure 5.21 illustrates two of the fabricated membranes.

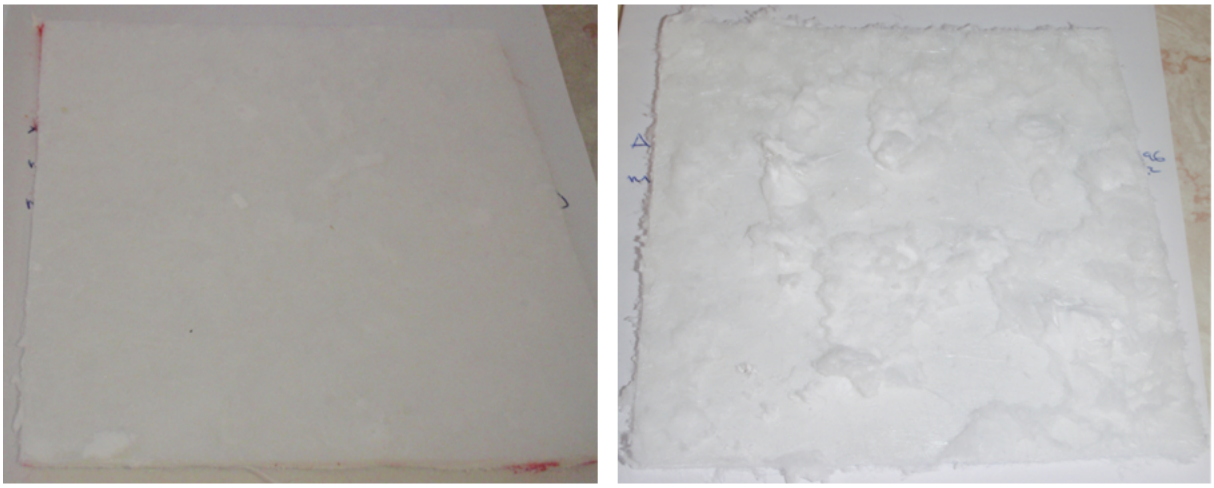

Figure 5.21: The left picture is a membrane fabricated by depositing 30 g PSMS /m^2 of a 54 w/w % PSMS/DMF onto a glass fiber mat while the right pictures is a membrane with 40 g PSMS/m^2 of a 60 w/w % PSMS/DMF.

The air permeability of each membrane was investigated by measuring the flow rate, Q, and pressure drop, Δp, across the membrane. The permeability could hereby be determined by Darcy's Law as the ratio between Q and Δp [44]. Darcy's Law is illustrated as equation 5.43.

$$k_D = \left(\frac{\mu \cdot Q}{A}\right) \cdot \left(\frac{\Delta x}{\Delta p}\right) \tag{5.43}$$

Where k_D is the permeability constant [m^2], μ is the air viscosity ($0.0181 \cdot 10^{-3}$ Pa·s), A is the test sample area [m^2] and Δx is the sample thickness [m].
Measuring the thickness of a textile is however problematic and is therefore often the largest source of error [44]. It was therefore preferred to present the air permeability in terms of the apparent flow resistance, as defined in equation 5.44.

$$R_D = \left(\frac{A \cdot \Delta p}{\mu \cdot Q}\right) \tag{5.44}$$

Where R_D is the apparent Darcy flow resistance [m^{-1}] [44]. The resulting R_D values are depicted in Figure 5.22, as a function of deposited PSMS fibers. The marked black line in the figure illustrated the R_D of the template glass fiber mats.

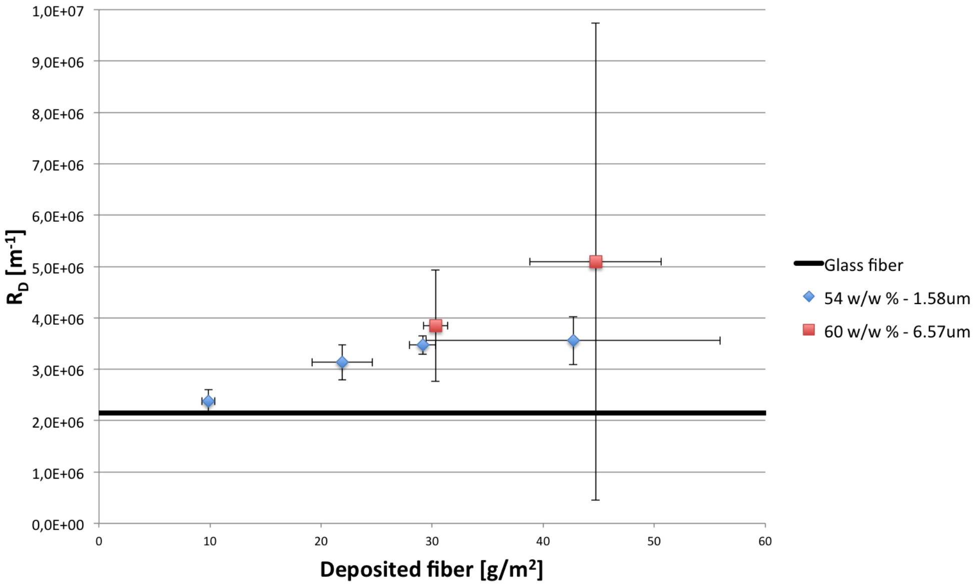

Figure 5.22: The apparent Darcy flow resistance related to the deposition of electrospun fibers.

The measured porosities of the fabricated membranes resulted in porosities of approximately 1, as illustrated in Table 5.10, which could indicate that no membrane was present.

5.5 Liquid/liquid coalescence

The last aim of this thesis was to investigate the separation performance of superhydrophobic membranes. This resulted in the fabrication of 6 different types of membranes, termed A_{10}-A_{40} and B_{30}-B_{40}, which were made by electrospinning PSMS onto glass fiber mats. The separations performance was investigated, as described in section 4.7, by measuring the size drop distributions on which the separations efficiencies were calculated using equation 5.45.

$$\begin{aligned} \text{Efficiency} &= 1 - \frac{C_d}{C_u} \\ \text{Efficiency} &= 1 - \frac{\sum_d \cdot \rho \cdot N_d \cdot (\pi/6) \cdot d_d^3}{\sum_u \cdot \rho \cdot N_u \cdot (\pi/6) \cdot d_u^3} \end{aligned} \tag{5.45}$$

Where N_d [-] is the number of water droplets downstream of size d_d [m] and N_u [-] is the number of water droplets upstream of size d_u [m] and ρ is the density of water [g/m^3].
The resulting efficiencies for each membrane type is depicted in Figure 5.23.

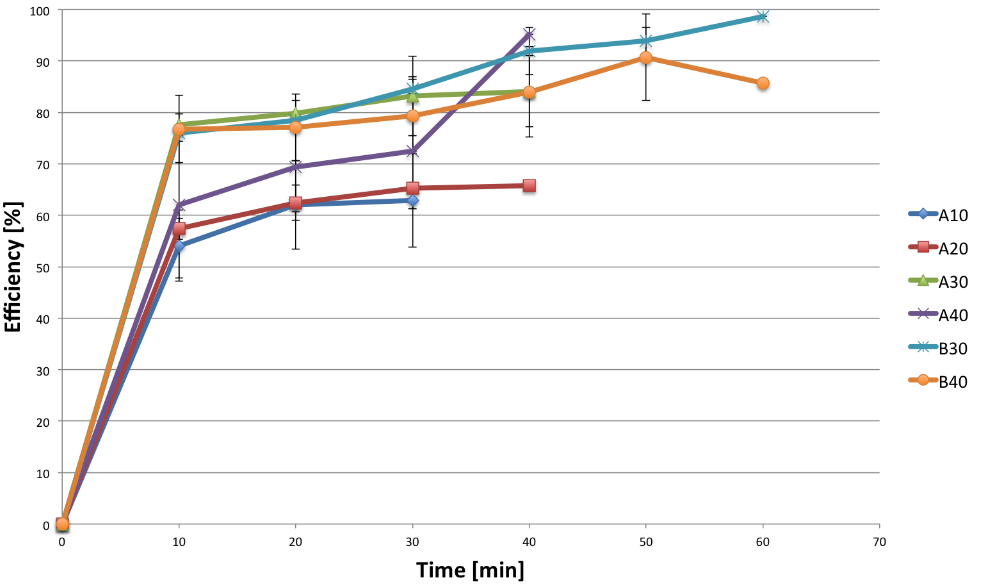

Figure 5.23: The separation efficiency versus time of the 6 different type of membranes.

Each separation was terminated when the increase in separation efficiency did not noteworthy increase indicating that steady state was achieved. The steady state, as seen on the figure, of the different membranes was achieved at different time intervals, thus the experiments were terminated at various times. As seen on the figure, the separation efficiencies increased as a function of deposited fibers and fluctulations in the efficiencies of the A_{40}, B_{30} and B_{40} membranes could be observed at the last measurement due to only one of the triplicates was meausred at the last point, since it had not reached steady state. This therefore resulted in a single determination in the 3 respective points, which therefore did not contain as much information as the previous measurements.

Figure 5.24 illustrates the pressure drop as a function of time for the 6 different type of membranes. Again note that the A_{40}, B_{30} and B_{40} membranes at 40, 60 and 60 min. was determined by a single determination, resulting in the increase or decrease of the pressure drops.

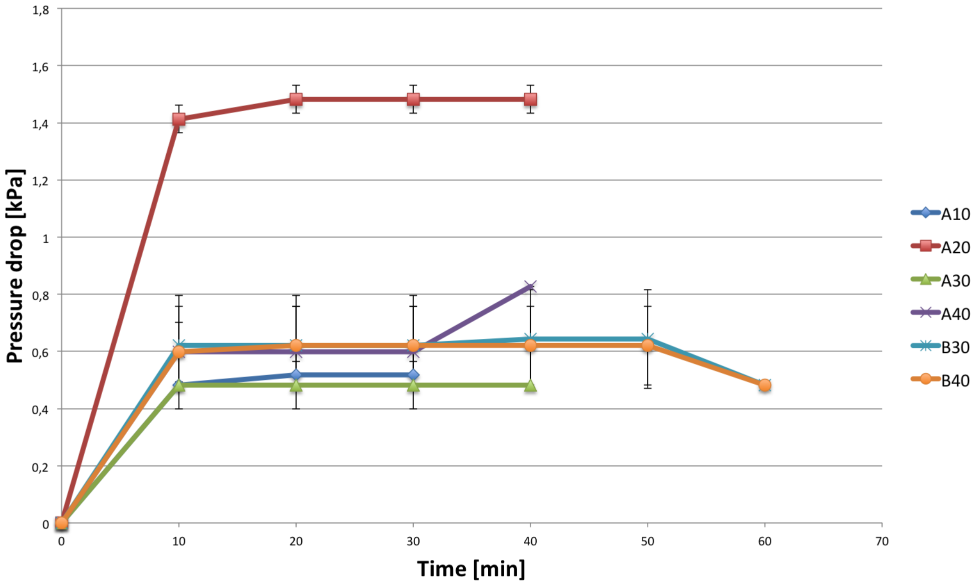

Figure 5.24: The pressure drop as a function of time for the 6 different type of membranes.

An example of the size drop distribution is illustrated in Figure 5.25, which clearly depicts that the size drop distribution decreases as a function of time. The size drop distribution marked as "Upstream" was collected at the upstream sample point whereas all other samples were collected at the downstream sample point. The sudden drop in count at 30 μm was a constant result of the analysis using the Azzusizer.

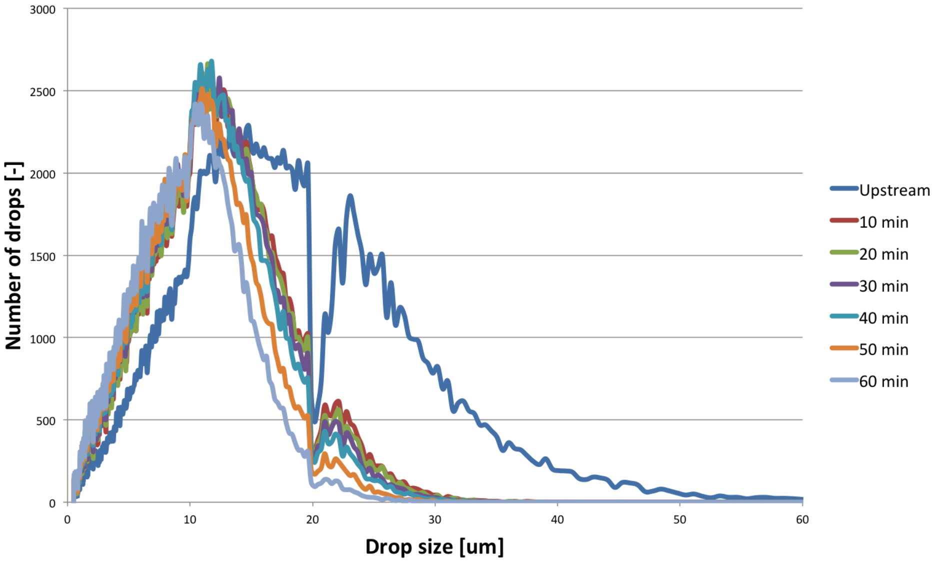

Figure 5.25: The size drop distributions measured during the liquid/liquid coalescence using one of the B_{40} membrane.

6. Discussion

This chapter discusses the results produced during this thesis and will be presented in the same order as the two previous chapters.

6.1 Inverse-quantitative structure-activity relantionship

In this section the results of the i-QSAR model will be discussed. However steps such as the translation of the molecular structures, construction of constraint equations, solving these and the structure generation will not be discussed since these are valid systematic methods.

6.1.1 Quantitative structure-activity relantionship analysis

The first model developed was the QSAR model based on the contact angle height 1 atomic Signatures, which contained 5 atomic Signatures. As Figure 5.1 and Figure 5.2 illustrates, this model obtained a R^2 value of 0.52, which clearly indicate poor correlative abilities. In addition the model also obtained poor predictive abilities, which is illustrated by the poor q^2 values of 0.31. The poor linear correlation could be caused by a number of reasons. One, due to the wide range of contact angles in the training set, 45.9-112.1^o, computational errors might have occurred. Two, the training set contains a number of outliners inflicting with the regression and predictability. Three, the atomic Signatures could not sufficiently describe the contact angle of a polymer surface. Four, the relationship is not linear.

The first reason was investigated by normalizing the contact angles between -1 and 1 and recalculating the QSAR model. The same model was however obtained with maximum R^2 and q^2 values of 0.52 and 0.31, respectively. To eliminate the possibility of future computational errors the following models were all normalized.

The second reason was investigated using a 2-sided Grubbs test with a significance level of 0.1 and by using the predicted values the following G values were obtained.

$$G_{min} = 3.63$$
$$G_{max} = 2.18$$

These values were then compared with the critical value of the t-distribution of 3.11 and since G_{min} was greater, it was insignificant and therefore removed from the dataset. This was the data point [x;y] = 45.9;38.9 in Figure 5.2 and corresponds to the removal of cellulose acetate. The Grubbs test was then performed again but no further outliners were present. A new QSAR model was therefore developed with 9 atomic Signatures, a maximum q^2 value of 0.36 and a R^2 value of 0.62. The correlation was hereby increased by 10 % but both values were still poor.

The possibility that the atomic Signature insufficiently described the relationship could be due to two reasons. First, the 5 atomic Signatures used in the model is an insufficient number of atomic Signatures to properly describe the relationship and additional atomic Signatures were therefore needed to obtain a better performing model. Second, the atomic Signature itself cannot describe the relationship between the canonized substructures and the water contact angles of polymer films, thus suggesting that the surface morphology is the dominant factor. In order to investigate this further a second model based on the same training set, which utilized the height 2 atomic Signatures, hereby including more data per atomic Signature, was developled. As illustrated in Figure 5.1 and Figure 5.3, the correlative abilities of both models, independent of the number of atomic Signatures, never increased further than 0.72. However if the predictive capacity of both models still should be maintained, thus avoiding overfitting, the best correlating model obtained was the model with height 2 atomic Signature. This model obtained a R^2 value of 0.53 and a q^2 value of 0.42 and comparing this model with 5 QSAR models developed by Weis and Visco (2010) [15], which achieved R^2 values of 0.69-0.80 and q^2 values of 0.23-0.71, the height 2 atomic Signature model could be accepted as being sufficiently correlative and predictive. However as Weis and Visco also reports, such models should be treated with care. This is also in agreement with Roy and Leonard (2006) [22] who describes QSAR models as being predictive when $q^2 > 0.5$ hereby making the height 2 atomic Signature model unable to predict the contact angle of polymers outside of the training set. This could, as previously described, be caused by too few Signatures included in the model, the Signature itself being insufficient to describe the contact angle of polymer films or that the relationship is not linear.

Before investigating a non-linear relationship a new training set was acquired. This training set originated from one source hereby eliminating the variance that was included in the training set used in the above, due to its origine from multiple sources. The new training set did not describe the water contact angles due to the limited information available, but rather contained information of polymers critical surface tension. This is a method used to described the energy of a surface and is further described in section 2.1.2. The first QSAR model developed using this training set was based on height 1 atomic Signatures. This model obtained a R^2 value of 0.95, which ensured the correlation between the predicted- and experimental CST values, as depicted in Figure 5.6. In addition the correlation had an approximately 45^o angle, which is a requirement for a good model as described by Weis and Visco (2010) [15]. The predictability of the model was ensured with a q^2 value of 0.80, which is greater than the suggested 0.5.
As described in section 5.1.2, a second QSAR model was developed on the basis of height 2 atomic Signatures. This model obtained a R^2 value of 0.92 and a q^2 values of 0.79. Both of these models exhibit great correlative and predictive abilities however only the best performing QSAR model should be selected for the i-QSAR problem. This was done by evaluating the R^2 and q^2 values of the two models, which clearly showed that the height 1 atomic Signature model performed best in both aspects. In addition, this model contained 2 additional atomic Signatures making the CST predictions based on more structural information. Comparing this model with the best performing model developed by Brown et al. (2006) [18], which contained 12 signature and R^2 and q^2 values of 0.96 and 0.95, respectively. The CST model showed similar correlative abilities and less predictability, however since the q^2 value of the CST model was greater than

0.5, it is still considered being predictable. Comparing the CST model with models developed by Weis and Vicso (2010) [15], which contained 7-13 signatures, R^2 values of 0.71-0.80 and q^2 values of 0.23-0.71. The CST model both had higher correlative and predictive abilities and contained an increasing number of atomic Signatures hereby making it more than sufficient for the i-QSAR analysis.

6.1.2 The constraint equation

The constraint equations were solved using a CST interval of -1.001 to -1.000, which corresponds to 16.884-16.900 mJ/m^2. This interval was chosen on the basis of computational time and initially the interval was set to -1.5 to -1.0, however such calculations could have taken days, weeks or months and the used interval was selected based on trial and error.

6.1.3 Subjective evaluation

Solving the constraint equations and generating connected graphs, i.e. connected 2D molecular structures, resulted in 456 polymer-repeating units. The success of the i-QSAR with respect to methodology was therefore a success. In mind of purschasing a polymer the next step was to evaluate the solved structures on the basis of internal strain, solubility, adhesion with water, availability and cost. The solved polymer repeating units of Figure 5.9 and Figure 5.10 could in general be classified as solutions containing elevated internal strain. Solutions like these could have been avoided by implementing a force field, which calculates the internal energy of the solved 2D molecular structures and discards molecules with an internal energy too great [15]. This could however lead to false internal energies due to the dummy atoms used in this analysis hereby removing polymers which in reality contained a lower internal energy. The force field was therefore not implemented.

The repeating units of the first polymer in Figure 5.9 is depicted as being inside the carbon ring, however due to the rotational freedom of the oxygen bonds connecting the carbon chain to the benzene ring, the repeating units would properly be present on the outside. This polymer could possibly exist, even though the internal strain would be elevated, however from a synthetic point of view difficult to synthesize. The second polymer of Figure 5.9 contains two closely bonded cycloalkanes. The relative short bond lenght between the cycloalkanes combined with the closely bonded repeating atoms of the polymer would properly introduce a too great strain for this polymer to exist. The last polymer of Figure 5.9 can, as to the best of my knowledge, exist but has yet to be synthesized.

The first polymer of Figure 5.10 contains a substituted cyclopentadecane. The polymer would properly not contain high amounts strain or steric hindrance due to the way the repeating atoms are positioned, enabling space for the cyclopentadecane. However from a synthetic standpoint it would also be difficult to synthesize. The second polymer of Figure 5.10 is a derivative of the third polymer from Figure 5.9, but contains an additional carbon in the cyclic chain and a carbon less in the linkage to the benzene ring. The internal strain of this polymer is properly less than the third polymer of Figure 5.9, due to the steric hindrance occuring from the polymer backbone. It is therefore also considered as being able to exist.

Both polymers of Figure 5.11 are also considered as being able to exist since none of the two exhibits any form of elevated internal strain except for the cyclopropane at the end of the aliphatic segment. In addition the substituted aliphatic chains would improve the solubility of the produced polymers hereby making them easier to electrospin.

None of the above polymers have, as to my knowledge, been synthesized and due to the scope of this thesis an available polymer at relative low cost was needed. Structural units of the mentioned polymers were therefore reconstructed in the best possible way to obtain a polymer that was commercially available.
In each of the solved polymers a benzene ring was present with either a substituted aliphatic- or cyclic chain bonded by an oxygen bridge. The introduction of oxygen is however not favorable in the aspect of producing superhydrophobic materials due to its ability to form hydrogen bonds through its lone pairs. This would increase the adhesive forces and hereby the wettability of the polymer. Furthermore a methyl group was often substituted to the benzene ring and fluoride was most often bonded to at least one of the repeating carbon atoms. Beside the polymers used in the model (HFP, FEP, PTFE, PCTFE, PVDF, PVF) the number of fluoronated polymers is limited and the search of a polymer with such properties was therefore abandoned. The search of a commercially available polymer with an improved hydrophobicity was therefore restricted to a polymer containing a benzene ring substituted with an aliphatic- or cyclic- chain and resulted in the purchase of poly(styrene-co-α-methylstyrene), which is depicted in Figure 6.1.

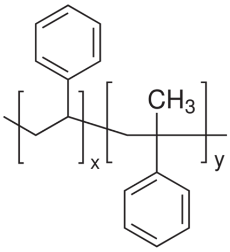

Figure 6.1: Poly(styrene-co-α-methylstyrene).

6.2 Vertification of inverse-quantitative structure-activity relationship

As seen in section 5.2, the CST determined by the QSAR equation resulted in 40.60 mJ/m^2 while the experimentally determined CST of PSMS resulted in 22.78 mJ/m^2. By comparing these values with the CST of Teflon, 19.4 mJ/m^2, and that of PMMA, 37.5 mJ/m^2, it is oblivious that the CST determined by QSAR predicts PSMS as being hydrophilic while the experimentally determined CST predicts it as being hydrophobic. This could either be due to an incorrect CST predicted by the model, experimentally or both.
The CST predicted by the QSAR model was done by first translating the structure of PSMS into atomic Signatures. This resulted in 2 additional atomic Signatures that were not included in the training set of the QSAR model. As such, one could argue that the QSAR model would be incapable of predicting the CST of this polymer however since 8 other atomic Signatures were included in the model and since half of the 10 atomic Signatures of PSMS were included in the QSAR equation, this does not seem likely.

The experimentally determined CST was measured using different ratios of formamide and 2-ethoxyethanol. These solvents were chosen since the experimental data used in the QSAR model were measured using these liquids [41]. However as described by Dann (1969) [14] the choice of solvent when determining the CST by extrapolation is of great importance since the CST should be a product of the total surface energy. This means that polar-, hydrogen- and Van der Waals interactions should be included in the measurements at the surface. However by having used formamide and 2-ethoxyethanol to determine the CST of PSMS dispersion forces were neglected. This would however have been the dominating interactions of PSMS due to the fact that PSMS does not contain any lone pairs in order to form hydrogen bonds or any significant amount of polarity. The experimentally determined CST of PSMS did therefore not describe the total surface energy of PSMS. This was also indicated by the spreading of the 0.03/0.97 V/V % formamide/2-ethoxyethanol liquid. This liquid had a γ_{lv} of 28.8 mJ/m^2 and as described in section 2.1.2, the CST is obtained when a liquid just wets the surface of a solid. This therefore indicated the true CST of PSMS was more likely to be near 28.8 mJ/m^2 than the values determined by either extrapolation or the QSAR model.

To investigate the CST of PSMS further, the surface was characterized by measuring the contact angle of water. This yielded in a contact angle of 94.10 ± 3.73^o, as depicted in Table 5.8, making PSMS hydrophobic. Comparing this value with the contact angle of poly(butadiene) of 96.0^o [41], the two materials seem alike and since the contact angle of poly(butadiene) is close to that of PSMS, one would expect the same for the CST. As illustrated in Table 4.3, poly(butadiene) has a CST of 29.3 mJ/m^2 hereby confirming the suspicion that the true CST of PSMS is near 28.8 mJ/m^2.

6.3 Electrospinning of poly(styrene-co-α-methylstyrene)

To increase the hydrophobicity of PSMS and achieve a superhydrophobic material, the control of the surface energy is alone insufficient and surface roughness must be induced in order to increase the hydrophobicity. Electrospinning is a method which previously has been used to do so and is a simple versatile method [45].

6.3.1 The investigation of the electrospinning ability of poly(styrene-co-α-methylstyrene)

The electrospinning of PSMS has, to the best of my knowledge, never been done before. The electrospinning ability of PSMS was therefore initially investigated by varying the polymer concentration, choice of solvent, flow rate, gap distance and voltage, as depicted in Table 5.9. Here it is evident that electrospraying occurred in all samples using cyclohexane and 90/10 w/w % cyclohexane/THF hereby forming beads. This could be an indication that the choice of solvent, in these samples, restricted the formation of fibers since either varying the flow rate, gap distance, voltage or polymer concentration resulted in formation of fibers. As described in section 2.3, solution properties such as the conductivity, viscosity and surface tension plays a key role in the fiber formation. The properties of the prepared solutions were however not investigated and were left for future work. Supaphol et al. (2005) [46] investigated the fiber formation of poly(styrene), which structural is closely related to PSMS, they reported the same tendencies

as for the non-spinability of poly(styrene) using cyclohexane as solvent and believed that this was due to the low conductivity of the solution, which could be related to low dipole moment of cyclohexane of 0.61 Debye.
The use of 90/10 w/w % cyclohexane/THF also resulted in electrospraying and is also believed to be caused by the low conductivity of the solution here confirming that the addition of 10 w/w % THF, with a dipole moment of 1.62 Debye was insufficient. Supaphol et al. (2005) [46] also reported that poly(styrene) was very easily electrospun by the use of THF, however the polymer solution often clogged the nozzle due to the fast evaporation, caused by the low boiling point of 66^{o}C. They also reported the ease of electrospinning poly(styrene) using DMF, which was attributed to the high dipole moment of 3.82 Debye leading to solutions of high conductivity. In addition DMF has a higher boiling point, 153^{o}C, minimizing the clogging of the nozzle.
The last set of samples were therefore electrospun using DMF as solvent, which for the 25 and 35 w/w % PSMS resulted in electrospraying and in an intermediate region for 50 w/w % PSMS, except when using a flow rate of 5 and 10 mL/hr, where a stable liquid jet sometimes was observed. This suggested that the concentration of PSMS was too low to form fibers since the intermediate region was observed independently of varying the gap distance or voltage.

In order to investigate this further, 9 different PSMS concentrations were investigated using 3 new groups electrospinning conditions and the morphology of each sample was investigated by SEM. The 3 groups of electrospinning conditions were chosen on the basis of the before mentioned investigations, thus the flow rate did not exceed 1 mL/hr and was investigated further by decreasing it to half, 0.5 mL/hr, in group 2 and 3. The gap distance was also investigated further by decreasing it to 10 cm in group 3, while the voltage was kept constant.
Samples electrospun using group 2 conditions are depicted in Figure 5.13, which illustrates the formation of beads until a concentration of 52 w/w % PSMS/DMF that resulted in an intermediate morphology between beads and fibers. At 54 w/w % PSMS/DMF fibers were produced and the transition from beads to fibers can be explained by the relationship between the cohesive forces of the solution and the applied field. When the cohesive forces of the solution are low, i.e. a low polymer concentration, the applied field overcomes the cohesive forces of the liquid and as a consequence tears the liquid jet apart resulting in the formation of beads. When a critical concentration is obtained the cohesive forces of the liquid will hold the liquid together hereby only allowing the applied field to pull in the liquid jet thus forming fibers. This critical concentration was obtained for the group 2 conditions at 54 w/w % PSMS/DMF while it for the group 1 and 3 conditions already was obtained at 52 w/w %. The lower critical concentration of the group 1 conditions can be attributed to the higher flow rate, hereby reducing the energy of the applied field per volume solution allowing the cohesive forces of the solution to be maintained. Fibers were also formed for the 52 w/w % PSMS using the group 3 conditions. This sample was electrospun at a smaller gap distance than that of group 2, hereby decreasing the electrical resistance in the system. This should have allowed the applied field to overcome the cohesive forces of the solutions and form droplets [47]. However this was not the case and could possibly be explained by the small gap distance not allowing DMF, with a high boiling point, to evaporate before reaching the collector, thus not allowing the applied field to overcome the cohesive forces of the solution. Further investigations are however needed to confirm this hypothesis.

Next, the mean fiber size was investigated as function of the concentration for the 3 different

electrospinning conditions, which is depicted in Figure 5.17. This was done since the size of the fibers is one of the parameters controlling the surface morphology and hereby the hydrophobicity. The mean fiber size of samples from group 1 and 3 generally increased as a function of the increasing PSMS concentration. This is a well-known phenomenon that is due to an increase in the cohesive forces by the added polymers and has for certain polymers been demonstrated to show a power law relationship [24]. The fiber size distributions are as depicted in the figures overlapping indicating that splitting of the polymer jet, as described in section 2.3, might have been present in the electrospinning process. This is evident in the SEM pictures, Figure 5.13, which illustrates that fibers with different diameters are present hereby confirming this suspicion, which can mainly be attributed to the low M_w of PSMS.
As seen on Figure 5.13, the mean fiber size of group 2 electrospun fibers decreases with increasing PSMS concentration. This is however unusual and has, as the best to my knowledge, only occurred in the electrospinning of poly(caprolactone) and gelatin blends [48] and to truly explain this relationship, further investigations are needed.

When comparing the concentrations needed to electrospin PSMS, 50-60 w/w %, with concentrations used in the electrospinning of polymers such as nylon-6,6, poly(urethanes), poly- (benzimidazole) and poly(carbonate), which are electrospun using 10-15 w/w % solutions [24], the concentrations are much greater. This was caused by the molecular weight of PSMS, M_w = 2.800 g/mol, which is considerably lower than the previously mentioned polymers of M_w = 10.000-1.000.000 g/mol [24]. Initially we therefore had concerns that electrospinning of PSMS would be difficult or impossible due to the resulting solutions low viscosities and low surface tensions hereby making PSMS unable to electrospin.

6.3.2 The hydrophobicity of electrospun poly(styrene-co-α-methylstyrene)

The hydrophobicity of the produced fibers was investigated as a function of the fiber diameter, since the the surface roughness is a key factor in the hydrophobicity of surfaces. As described is chapter 1, the separation of secondary dispersions of water-in-diesel is greatly influenced by the hydrophobicity of the membrane surface. Notice that the 52 w/w % PSMS/DMF was not investigated due to its inability of being electrospun using the group 3 electrospinning conditions.

As seen on Figure 5.18, Figure 5.19 and Figure 5.20 there is a general trend for the hydrophobicity as being greater for the lowest mean fiber diameters. This is due to an increase in the surface area hereby increasing the repulsive forces at the interface and allowing more air to be trapped between the individual fibers, as described by Ma et al. (2005) [45]. The hydrophobicity then generally decreased as a function of the mean fiber diameter and is a result of a decrease in surface roughness, thus some of the pores and hollows have increased in size allowing water drops to penetrate and hereby lowering the contact angle. However for samples such as the 2.78 and 3.30 μm mean fiber diameter of Figure 5.19, the hydrophobicity increased as a function of the mean fiber diameter after the pre-described decrease in hydrophobicity. These samples were electrospun at 56 and 54 w/w % PSMS/DMF respectively, which resulted in the formation of beaded fibers as depicted in Figure 5.13. Ma et al. (2005) [45] also described that the formation of beaded fibers increased the roughness of the fiber mats surface hereby inducing greater amounts of pores and hollows, thus increasing the hydrophobicity of the surface. This has also been experimentally confirmed by Lim et al. (2007) [49] and Menini and Farzaneh (2008) [50]. The same tendency was evident in Figure 5.20 where the contact angle was greatest for the 54 and 56 w/w % PSMS, both samples contained beaded fibers and as a result the bead-free fibers, 58 and 60 w/w %, had the lowest contact angles. The group 1 electrospun fiber mats deviated from this trend by increasing in contact angles for the 60 w/w % PSMS, which however did not contain beaded fibers. Further analysis are therefore needed to investigate this irregular tendency, but must somehow be related to the surface morphology.

The contact angle was also investigated as a function of deposited fiber, which according to Ding et al. (2005) [51] has a influence on the surface roughness and hereby on the hydrophobicity. The relationship is depicted in Figure 5.18, Figure 5.19 and Figure 5.20 illustrates that the contact angle decreases as a function of deposited fibers for all the analyzed samples thus indicating that the increase in fiber mat thickness decreased the roughness of the surface, hereby decreasing the contact angle and the hydrophobicity.

The purpose of electrospinning PSMS was to increase the hydrophobicity by creating a rough surface. The contact angle for the flat PSMS surface was 94.10 ± 10^o. The lowest contact angle measured for an electrospun sample was 131.33 ± 0.87^o while the most hydrophobic surface produced had a contact angle of 165.85 ± 0.51^o, which had a mean fiber diameter of 3.30μm and a weight of 10 g PSMS/m^2. The introduction of pores and hollows into the surface by electrospinning PSMS hereby maximum increased the contact angle with 74.75^o and yielded in the production of a superhydrophobic surface.

6.4 Membrane manufacturing and characterization

The 6 series of fabricated membranes presented in Table 5.10 was selected in order to investigate the influence of deposited fibers, hydrophobicity and mean fiber diameter on the later filtrations of the secondary dispersed water-in-diesel. Two series of membranes were therefore manufactured. The A series had a constant mean fiber diameter of 1.58 μm and varied in deposited fibers by 10-40 g PSMS/m^2. The B series had a greater mean fiber diameter of 6.57 μm and varied in deposited fibers by 30 and 40 g PSMS/m^2. The separation of secondary dispersions of water-in-oil emulsions is thought, due to the low diameter water droplets, to be related to air filtration. The measured air permeability's of the fabricated membranes should therefore also be related to the performance of the liquid/liquid coalescence filtrations. However due to difficulties in accurately measuring the thickness of the produced membranes, the apparent Darcy flow resistance, R_D was instead determined. The mean R_D of the fabricated membranes was all in the range of $2.38\cdot10^6$-$5.10\cdot10^6$ m^{-1}, as depicted in Figure 5.22. Gibson et al. (2001) [44] achieved comparable greater Darcy flow resistances for polyester fabrics, 10^7-10^8 m^{-1}, tightly-woven cotton fabric, 10^8 m^{-1}, electrospun poly(acrylonitrile), 10^8-10^9 m^{-1} and Teflon microporous membranes with a Darcy flow resistance in the order of 10^9-10^{10} m^{-1}. They therefore concluded that the flow resistance of electrospun membranes were quite large compared with the pre-mentioned materials, which was a result of the small fiber diameters minimizing the mean free path through the membrane. However such high Darcy flow resistances were not observed for the electrospun PSMS membranes conducted in this project and can be contributed to both

the mass of deposited fiber, mean fiber size and the mean free path of the membranes, i.e. the porosity.
The air permeability is highly dependent on the mass of deposited fiber, as described by Darcy´s Law, and was confirmed by an increase in R_D as a function of deposited fiber, as depicted in Figure 5.22. In addition all of the fabricated membranes had a higher R_D than the template glass fiber mat and that a sort of "critical" R_D value of 3-4·10^6 m^{-1} was achieved for the A series membranes. This could indicate that the membrane thickness no longer was the most significant independent variable and that other parameters such as the mean free path started controlling the system. The mean free path is, besides the thickness, also dependent on the mean fiber diameter and can be quantified by the porosity. The resulting porosities of the fabricated membranes were all close to 1, which clearly indicated that the membrane porosities were less than the detection limit of the Pycnometer used, thus these results were neglected.
The "critical" R_D value of the A series membranes could instead be explained by the mean fiber size of 1.58μm in all the fabricated membranes, which therefore did not change the pressure drop or volumetric flow rate and hereby keeping R_D constant at 3-4·10^6 m^{-1}.

The R_D values of the B serie membranes was greater than the A series, however due to the large standard deviations caused by an irregular deposition of some of the B series membranes, which is illustrated on Figure 5.21 as the right membrane, nothing could be concluded based on these results.

6.5 Liquid/liquid coalescence

The filtration setup, as illustrated on Figure 4.2, was constructed in mind of mimicking the fuel system of a car. The pump connecting to the oil tank and filter holder was therefore a fuel pump used in, inter alia, GMC cars and the flux was kept constant at a rate of 0.92 $\frac{m^3}{m^2 \cdot hr}$. This setup would correspond to a car keeping the same rounds per minus thus keeping the flux of diesel constant. The performance of the experiments was, as described in section 5.5, evaluated based on removal efficiencies, which was done due to small fluctuations in the upstream size drop distribution between each filtration.

The removal efficiencies of the 6 different types of membranes ranged from 60-98 %, as depicted in Figure 5.23. The coalescence performance depends on the flow rate, membrane thickness, temperature, surfactants, wettability, size drop distribution and porosity [6] [5] [4]. In the filtrations conducted in this thesis only the membrane thickness, wettability and porosity was varied. The hydrophobicity of the 6 different types of fabricated membranes is depicted in Table 5.10 and illustrates that the hydrophobicity decreased as a function of deposited fibers. The efficiency on the other hand increased as a function of deposited fibers, as illustrated on Figure 5.23, indicating that other parameters were dominating. Sahu et al. (2012) [52] described that there exist a critical membrane thickness before water droplets, depending on the hydrophobicity, either are repelled or penetrates the membrane. The critical membrane thickness of the fabricated membranes is in the order of 30 g PSMS/m^2 since, as seen on Figure 5.23, the separation efficiency of the A series membranes is highly dependent on the membrane thickness until the A_{30}

membranes. The A_{30} membranes however has greater separation efficiencies than the A_{40} membranes clearly indicating that the membrane thickness no longer is the dominating independent variable. The better removal efficiency of the A_{30} membranes can instead be contributed to the larger mean contact angle of 14.28^o, relative to the A_{40} membranes, making these membranes more hydrophobic and thereby able to repel more water than the A_{40} membranes.

The increase in pressure drop that was observed within the first 10 min. of all runs, see Figure 5.24, can be related to the total resistance of the system, which can be described by Darcy's Law, as equation 6.1 illustrates.

$$J = \frac{\Delta P}{\mu \cdot (R_m + R_c)} \tag{6.1}$$

Here J is the flux $\left[\frac{m^3}{m^2 \cdot s}\right]$, R_m is the membrane resistance [m^{-1}] and R_c is the cake resistance [m^{-1}]. The initial pressure drop can be explained as a consequence of an increase in the total resistance, i.e. R_m and R_c, since the flux and viscosity was constant during all of the conducted filtrations. The cake resistance in the liquid/liquid coalescence of water-in-oil emulsions is caused by pore blocking of the membrane by the water droplets. Over time more water is transported to the membrane, which will coalesce with the droplets retained at the surface of the membrane forming larger droplets. When reaching a critical size, the droplets will due to gravity and the difference in density of diesel and water precipitate to the bottom of the filter holder hereby reducing the cake resistance. Further more, small enough water droplets will be transported through the membrane and into the storage tank.

The transport of water to the membrane, the precipitation of larger water droplets and the transport of water through the membrane are factors that influence the cake resistance and hereby the pressure drop. The second parameter that influence the total resistance of this system is the membrane resistance, which as described by Hu and Scott (2007) [53], is a function of the pore size distribution, porosity, thickness, shape and permeability. As a filtration is started the flow of the diesel-water emulsion can change some of these parameters by compressing the membrane hereby reducing the pore size distribution, porosity, thickness and permeability thus increasing R_m and hereby the pressure drop. The initial increase in pressure drop can therefore be related to both the cake- and membrane resistance. Figure 5.24 also illustrates that the pressure drop generally increases as a function of deposited fiber as the A_{10} and A_{30} had lower pressure drops than the A_{40}, B_{40} and B_{30} membranes. This can be related to the membrane resistance, which as described in the above among other things is a function of the membrane thickness. This also correlates with the apparent Darcy flow resistance, as shown in Figure 5.22, thus the pressure drop increases as a function of the mean R_D. The A_{20} membranes however exhibited a much greater pressure drop than all other membranes. This could indicate that these membranes contained a greater R_m but as shown in Figure 5.22, they exhibited lower apparent Darcy resistances than the membranes with greater amounts of deposited fiber. Also, the mean fiber diameter of the A series membranes should be equal, since they were electrospun using the same electrospinning conditions thus to fully explain this sudden increase in pressure drop, further analysis are needed.

An example of the size drop distribution is depicted in Figure 5.25. This illustrates that the larger water droplets are removed during the filtrations. This is a consequence of the lower surface tension of the larger water droplets compared to the higher surface tension of the smaller water droplets. The surface tension of the larger water droplets is therefore more easily overcome by the kinetic energy of the collisions, than it is between smaller water droplets, between the water droplets at the membrane surface. In addition, the size drop distribution of the permeate has shifted toward higher amounts of smaller droplets with a mean diameter of approximately 20 μm. This phenomenon can be caused by the transport of droplets through the membrane, which will come into contact with the membrane and depending on the membrane porosity and flow, the droplets can be broken into smaller droplets.

The best performing membranes, which was conducted in triplets, was the B_{30} membranes which reached steady state at 50 min. with a separation efficiency of 93.85±2.64 % and a pressure drop of 0.64±0.17 kPa. Note that the last data point of the B_{30} series only contains the information from one separation and was therefore not used for this comparison.
The separation performance of secondary dispersions of water in diesel of the B_{30} membranes is hereby greater than the hydrophilic membranes made from electrospun poly(amide), which maximum obtained a separation efficiency of 84.0±2.5 % with a pressure drop of 15 kPa [6]. The B_{30} membranes also performed better compared to hydrophilic membranes fabricated from electrospun poly(styrene), which had the greatest separation efficiency of 88.1 % and a pressure drop of 25 kPa [5]. The electrospun PSMS membranes hereby both performed better than previous fabricated membranes with respect to both separation efficiencies and pressure drop.

7. Conclusion

The objective of this project was to identify a novel polymer with improved hydrophobicity for the separation of secondary dispersions of water-in-diesel.

The identification of superhydrophobic materials is a twofold process since the hydrophobicity of materials is both dependent on the surface energy and the surface morphology. The identification of a polymer with a low surface energy was done by developing an inverse-quantitative structure-activity relationship on the basis of critical surface tensions, CST. This resulted in 456 potential polymers with predicted CST of 16.884-16.900 mJ/m^2. These solutions were then subjective evaluated on internal strain, solubility, adhesion with water, availability and cost. The evaluation resulted in the purchase of poly(styrene-co-α-methylstyrene), PSMS. The critical surface tension of a flat PSMS surface could however not be determined accurately, either by the model or experimentally, but was in the order of 28 mJ/m^2. The contact angle of the flat PSMS surface was experimentally determined to 94.10$\pm$3.73^o and PSMS could therefore be characterized as being hydrophobic.

To further increase the hydrophobicity of PSMS, electrospinning was adapted to induce pores and hollows into the surface and hereby change the surface morphology. PSMS has however, as to the best of my knowledge, never been electrospun and the electrospinning ability of PSMS was therefore investigated. PSMS was successfully electrospun by electrospinning concentrations of 54-60 w/w % PSMS/DMF at a flow rate of 0.5 and 1 mL/hr, a gap distance of 10 and 20 cm and a voltage of 30 kV. This yielded in the production of fiber mats with different fiber diameters and amount of deposited fibers. These samples were analyzed by contact angle measurements to determine the hydrophobicity. In general the contact angle decreased as a function of the mean fiber diameter, as less pores were present in the PSMS surface. Samples containing beaded fibers had higher contact angles than bead-free fibers and the contact angle decreased as the function of deposited fibers, which indicated that the added amount of fibers reduced the amount of pores and hollows in the surface. The electrospinning of PSMS resulted in surfaces with contact angles of 131.33-165.85^o hereby maximum improving the contact angle by 74.75^o and producing superhydrophobic surfaces.

Membranes for the separation of water-in-diesel were fabricated by electrospinning PSMS onto template glass fiber mats. The fabricated membranes separated the secondary dispersions of water with efficiencies ranging from 65.76-93.85 % and pressure drops of 0.48-1.48 kPa. The best performing membranes were fabricated by electrospinning a 60 w/w % PSMS/DMF solution onto glass fiber mats with an average deposited weight of 30.29 g PSMS/m^2. These membranes had a water contact angle of 155.65$\pm$3.11^o and could be therefore be classified as being superhydrophobic. Steady state was reached after 50 min. with separations efficiencies of 93.85$\pm$2.65 % and pressure drops of 0.64$\pm$0.17 kPa.

Bibliography

[1] Feng L., Zhang Z., Mai C., Ma Y., Liu B., Jiang L., and Zhu D. (2004). "A super-hydrophobic and super-oleophilic coating mesh film for the separation of oil and water", *Angew. Chem. Int. Ed.*, 43, 2012-2014, .

[2] Grignard B., Vaillant A., Coninck J.D., Pines M., Jonas A.M., Detrembleur C., and Jerome C. (2011). "Electrospinning of a functional Perfluorinated block copolymer as a powerful route for imparrting superhydrohobicity and corrosin resistance to aluminum substrates" *Langmuir*, 27, 335-342, .

[3] Stanfel A. (2009). "Fuel filtration: Protecting the diesel engine", *Filtration + Separation*, May/June, 22-25, .

[4] Shin C. and Chase G.G. (2004). "Water-in-Oil Coalescence in Micro-nanofiber Composite Filters", *AIChE Journal*, Vol. 50, No. 2, 343-350.

[5] Shin C., Chase G.G., and Reneker D.H. (2005). "Recycled expanded polystyrene nanofibers applied in filter media", *Colloids and Surfaces A: Physicochem. Eng. Aspects*, 262, 211-215, .

[6] Shin C. and Chase G.C. (2005). "Separation of Water-in-Oil Emulsions Using Glass Fiber Media Augmented With Polymer Nanofibers", *Journal of Dispersion Science and Technology*, 27, 512-522.

[7] Pan Q., Wang M., and Wang H. (2008). "Separating small amount of water and hydrophobic solvents by novel superhydrophobic copper meshes", *Applied Surface Science*, 254, 6002-6006.

[8] Buckton G. (1990). "Contact Angle, Adsorption and Wettability - a Review with Respect to Powders", *Powder Technology*, 61, 237-249.

[9] Jiang L. and Feng X. (2006). "Design and Creation of Superwetting/Antiwetting Surfaces", *Adv. Mater.*, 18, 3063-3078.

[10] Heimbuch J. (2009). "NASA Uses Lotus Leaf As Inspiration for Space Gear Dust-Repellent", *Threehugger*, Accessed: 12-05-2012, <www.threehugger.com/clean-technology/nasa-uses-lotus-leaf-as-inspiration-for-space-gear-dust-repellent.html>, .

[11] Harvard University (2011). "Hydrophobic de-icing without chemicals", *Ask Nature*, Accessed: 12-05-2012, <www.asknature.org/product/4feddb09a84cb65ac0ed01d2109fa731>.

[12] Burris A. (1999). "Discovery of factors affecting bubble size in water", *QuickPure*, Accessed: 12-05-2012, <www.quickpure.com/Diffusers.htm>.

[13] Neumann A.W. and Spelt J.K. (1996). *Applied Surface Thermodynamics*, Dekker New York, ISBN: 0-8247-9096-0.

[14] Dann J.R. (1969). "Forces Involved in the Adhesive Process - I. Critical Surface Tensions of Polymeric Solids as Determined with Polar liquids", *Journal of Colloid and Interface Science*, Vol. 32, No. 2, 302-320.

[15] Weis D.C. and Visco D.P. (2010). "Computer-aided molecular design using the Signature molecular descriptor: Application to solvent selection", *Computers and Chemical Engineering*, 34, 1018-1029.

[16] Churchwell C., Rintoul M.D., Martin S., Visco D.P., Kotu A., Larson R.S. Sillerud L.O., Brown D.C., and Faulon J.L. (2004). "The signature molecular descriptor 3. Inverse-quantitative structure-activity relationship of ICAM-1 inhibitory peptides", *Journal of Molecular Graphics and Modelling*, 22, 263-273, .

[17] Todeschini R. and Consonni V. (2002). "What is a molecular descriptor", *Milano Chemometrics and QSAR Research Group*, Accessed: 11-11-2011, <www.moleculardescriptors.eu/tutorials/what-is.htm>.

[18] Brown W.M., Martin S., and Rintoul M.D. Faulon J.L. (2006). "Designing Novel Polymers with Targeted Properties Using the Signature Molecular Descriptor", *J. Chem. Inf. Model.*, 46, 826-835.

[19] Faulon J.L., Visco D.P. Pophale R.S., and Rintoul M.D. (2002). "Developing a methodology for an inverse-quantitative structure-activity relationship using the signature molecular descriptor", *Journal of Molecular Graphics and Modelling*, 20, 429-438, .

[20] Faulon J.L., Visco D.P., and Pophale R.S. (2003). "The signature molecular descriptor. 1. Using extended valence sequence in QSAR and QSPR studies", *J. Chem. Inf. Comput. Sci.*, 43, 707-720, .

[21] Navidi W. (2006). *Statistics for Engineers and Scientists*, McGraw-Hill, ISBN: 0-07-255160-7.

[22] Roy K. and Leonard T.J. (2006). "On selection of Training and Test Sets for the Development of Predictive QSAR models", *QSAR combinatorial Science*, 25, no. 3, 235-251.

[23] Frenot A. and Chronakis I.S. (2003). "Polymer nanofibers assembled by electrospinning", *Current Opinion in Colloid and Interface Science*, 8, 65-75.

[24] Huang Z.M., Zhang Y.Z., Kotaki M., and Ramakrishna S. (2003). "A review on polymer nanofibers by electrospinning and their applications in nanocomposites", *Composites Science and Technology*, 63, 2223-2253.

[25] Li D. and Xia Y. (2004). "Electrospinning of Nanofibers: Reinventing the Wheel?", *Adv. Mater.*, 16, No. 14, 1151-1170.

[26] Trafton A. (2009). "Spinning at nanoscale - Electrospun fibers could be used for protective clothing, wearable power and more", *MITnews*, Accessed: 16-05-2012, <http://web.mit.edu/newsoffice/2009/electrospun-fibers-0505.html>, .

[27] Mark J.E. (2009). *Polymer Data Handbook*, Oxford University Press, ISBN: 0-19-518101-8, .

[28] Diversified Enterprises. "Critical Surface Tension and Contact Angle with Water for Various Polymers", *ACCU DYNE TEST*, Accessed: 01-11-2011, <www.accudynetest.com/polytable_03>, .

[29] Youngblood J.P. and McCarthy T.J. (1999). "Ultrahydrophobic Polymer Surfaces Prepared by Simulataneous Ablation of Polypropylene and Sputtering of Poly(tetrafluoroethylene) Using Radio Frequency Plasma", *Macromolecules*, 32, 6800-6806.

[30] Baier R.E. and Zisman W.A. (1969). "Wettability and Multiple Attenuated Internal Reflection Infrared Spectroscopy of Solvent-Cast Thin Films of Polyamids", *Macromolecules*, vol. 3, No. 4, 462-468.

[31] Kim K., Sung W., Park H., Lee Y., Han S., and Kim K. (2003). "Hydrophobic Properties of Ethylene-Vinyl Alcohol Copolymer Treated with Plasma Source Ion Implantation", *Journal of Applied Science*, 92, 2069-2075.

[32] Marletta G., Ciapetti G., Satriano C., Pagani S., and Baldini N. (2005). "The effect of irradiation modification and RGD sequence adsorption on the responce of human osteoblasts to polycaprolactone", *Biomaterials*, 26, 4793-4804.

[33] Khorasani M.T., Mirzadeh H., and Irani S. (2008). "Plasma surface modification of poly(L-lactic acid) and poly(lacto-co-glycolic acid) films for improvement of nerve cells adhesion", *Radiation Physics and Chemistry*, 77, 280-287.

[34] Kaba M., Raklaoui N., Guimon M.F., and Mas A. (2005). "Improvement of water selectivity of ULTEM polyetherimide pervaporation film by an allylamine plasma-polymerized layer", *Journal of Applied Polymer Science*, 97, 2088-2096, .

[35] Sauer B.B. and Dipaolo N.V. (1991). "Surface tension and Dynamic Wetting of Polymers Using the Wihelmy Method: Applications to High Molecular Weights and Elevated Temperatures", *Journal of Colloid and Interface Science*, Vol. 144, No. 2, 527-537.

[36] Sanchis M.R., Calvo O., Fenollar O., Garcia D., and Balart R. (2008). "Characterization of the surface changes and the aging effects of low-pressure nitrogen plasma treatment in a polyurethane film", *Polymer Testing*, 27, 75-83.

[37] Lee L.H. (1967). "Adhesion of High Polymer. II. Wettability of Elastomers", *Journal of Polymer Sciecne*, Part A-2, Vol. 5, 1103-1118.

[38] Sugama T. (2004). "Hydrothermal degradation of polybenzimidazole coating", *Materials Letters*, 58, 1307-1312.

[39] Feng L., Li S., Li H., Zhai J., Song Y., Jiang L., and Zhu D. (2002). "Super-Hydrophobic Surface of Aligned Polyacrylonitrile nanofibers", *Angew. Chem.*, 114, Nr. 7, 1269-1271, .

[40] Barabanov W.P., Osipov O.P., Sannikov S.G., and Torsuyev D.M. (2001). "Study of Fluorocarbon polymer wettability", *Chemistry and Computational Simulation*, Vol. 2, No. 6, 47-50.

[41] Diversified Enterprises. "Critical Surface Tension Components", *ACCU DYNE TEST*, Accessed: 10-01-2012, <www.accudynetest.com/polytable_01>, .

[42] Varabhas J.S., Chase G.G., and Reneker D.H. (2008). "Electrospun nanofibers from a porous hollow tube", *Polymer*, 49, 4226-4229.

[43] Dosunmu O.O., Chase G.G., Kataphinan W., and Reneker D.H. (2006). "Electrospinning of polymer nanofibers from multiple jets on a porous tubular surface", *Nanotechnology*, 17, 1123-1127.

[44] Gibson P., Schreuder-Gibson H., and Rivin D. (2001). "Transport properties of porous membranes based on electrospun nanofibers", *Colloids and Surfaces A: Physicochemical an Engineering Aspects*, 187-188, 469-481.

[45] Ma M., Mao Y., Gupta M., Gleason K.K., and Rutledge G.C. (2005). "Superhydrophobic Fabrics Produced by Electrospinning and Chemical Vapor Deposition", *Macromolecules*, 38, 9742-9748, .

[46] Jarusuwannapoom T., Hongrojjanawiwat W., Jitjaicham S., Wannatong L., Nithitanakul M., Pattamarom C., Koombhongse P., Rangkupan R., and Supaphol P. (2005). "Effect of solvents on electro-spinnability of polystyrene solutions and mophological apperance of resulting electrospun polystyrene fibers", *European Polymer Journal*, 41, 409-421.

[47] Greiner A. and Wendorff J.H. (2007). "Electrospinning: A Facinating Method for the Preparation of Untrathin Fibers", *Angew. Chem. Int. Ed.*, 46, 5670-5703.

[48] Ghasemi-Mobarakeh L., Prabhakaran M. P, Morshed M., Nasr-Esfahani M.H., and Ramakrishna S. (2008). "Electrospun poly(caprolactone)/gelatin nanofibrous scaffolds for nerve tissue engineering", *Biomaterials*, 29, 4532-4539, .

[49] Lim J.-M., Yi. G.-R., Moon J.H., Heo C.-J., and Yang S.-M. (2007). "Superhydrophobic Films of Electrospun Fibers with Multiple-Scale Surface Morphology", *Langmuir*, 23, 7981-7989.

[50] Menini R. and Farzaneh M. (2008). "Production of superhydrophobic polymer fibers with embedded particles using the electrospinning technique", *Polym. Int.*, 57, 77-84.

[51] Ding B., Fujimoto K., and Shiratori S. (2005). "Preparation and characterization of self-assembled polyelectrolyte multilayered films on electrospum nanofibers", *Thin Solid Films*, 491, 25-28, .

[52] Sahu R.P., Sinha-Ray S., Yarin A.L., and Pourdeyhumi B. (2012). "Drop impacts on electrospun nanofiber membranes", *Soft Matter*, 8, 3957-3970.

[53] Hu B. and Scott K. (2007). "Influence of membrane material and corrugation and process conditions on emulsion microfiltration", *Journal of Membrane Science*, 294, 30-39.

A. Standard curves

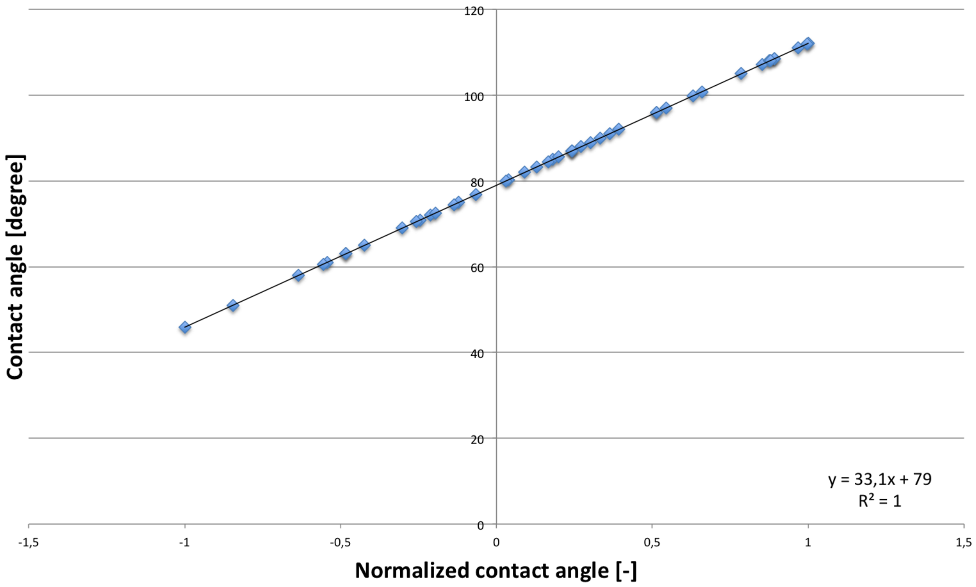

Figure A.1: Depicts the contact angles as function of the normalized contact angles.

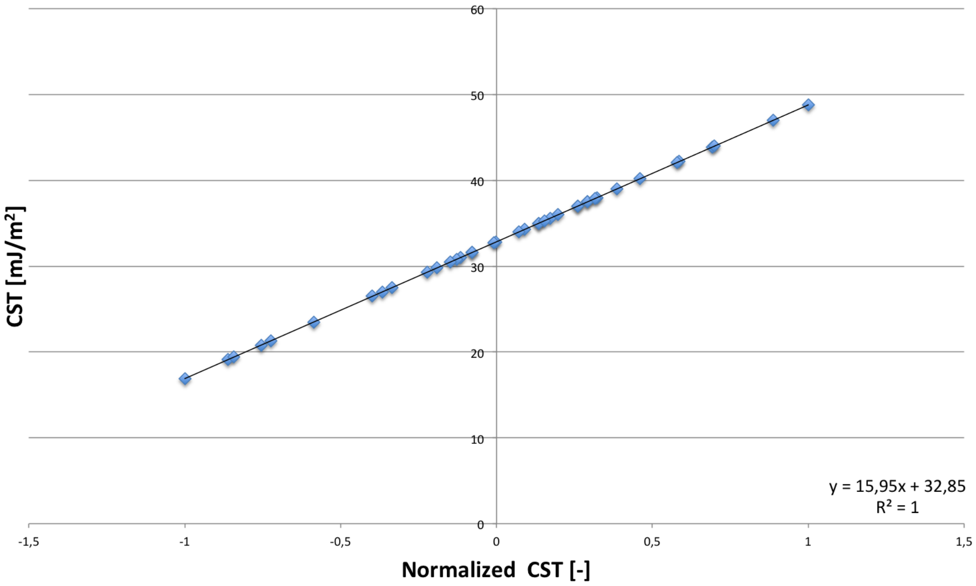

Figure A.2: Depicts the CST as function of the normalized CST.